Mesoscale Modelling of Waterspouts: An Offshore Wind Energy Perspective

Qidi Yu

MSc thesis in Geoscience and Remote Sensing of Civil Engineering
2020

Mesoscale Modelling of Waterspouts: An Offshore Wind Energy Perspective

by

Qidi Yu

to obtain the degree of Master of Science
at the Delft University of Technology,
to be defended publicly on 26 August, 2020 at 02:00 PM.

Student number:	4532910	
Thesis committee:	Dr. Sukanta Basu,	TU Delft, supervisor
	Prof. dr. S. J. Watson,	TU Delft
	Dr. Stephan de Roode ,	TU Delft

ABSTRACT

Wind energy is becoming an important renewable energy source. An increased number of offshore wind farms are constructed due to the relatively higher wind speeds. Besides, compared with the land, the ocean areas offer more empty space for the installation of wind turbines. In recent years, several governments in Europe have the plan to expand their countries' wind farms over the North Sea area. With this surge in the development of offshore wind farms, extreme weather events over the sea pose threats to the installations. A waterspout is one of such phenomenon of concern.

In this study, we simulated and characterized the atmospheric conditions associated with two waterspout events observed recently over the North Sea. These cases were selected from the European Severe Weather Database. Various types of observational data, including radiosondes, radar reflectivities, satellite imageries, lighting maps, and floating liar-based wind profiles, were utilized for detailed characterization. Atmospheric circulation patterns associated with waterspouts were deduced from surface-level and upper-air synoptic charts. A mesoscale model, called the Weather Research and Forecasting model, was used for simulations with a high spatial resolution of 1 km. We used five different parameterizations of varying complexities to quantify the sensitivity of the simulated results with respect to cloud microphysics. A number of meteorological variables and indices (e.g., thermodynamic indices, wind shear, vertical velocity, reflectivity) are extracted from the simulations and compared with the observational data. In general, our results are in agreement with the findings from previous studies. For instance, we have found that a double moment microphysics parameterization produces more realistic results in comparison with a single moment one. However, we have noticed that our simulated results fall outside the range specified by the so-called Szilagyi waterspout nomogram. This nomogram was initially proposed based on observational data from the Great Lakes region and is widely used by the operational meteorologists. Based on the results, updating this nomogram is needed with additional observational and simulated data from the North Sea region.

Contents

List of Figures

List of Tables

List of Abbreviations

AAIB Air Accidents Investigation Branch
AMU Applied Meteorology Unit

BRN Bulk Richardson Number
BS01 0-1 km Bulk Shear
BS06 0-6 km Bulk Shear
BWFZ Borssele Wind Farm Zone

CAPE Convective Available Potential Energy
CCN Cloud Condensation Nuclei
CIN Convective Inhibition
CLOSED Closed low pressure

DLCs Design Load Cases

ECMWF European Centre for Medium-Range Weather Forecasts
EL Equilibrium Level
EPL EuroPlatform
ESSL European Severe Storms Laboratory
ESWD European Severe Weather Database

F Fujita scale

HKZ Hollandse Kust Zuid

IEC International Electrotechnical Commission
IRENA International Renewable Energy Agency

KI K Index
KNMI Royal Netherlands Meteorological Institute

LCL Lifting Condensation Level
LFC Level of Free Convection
LW long-wave trough

MCAPE Maximum Convective Available Potential Energy
MSL Mean Sea Level

NASA National Aeronautics and Space Administration
NG non-gradient pressurefield
NOAA National Oceanic and Atmospheric Administration
NWP Numerical Weather Prediction

PSD Particle Size Distribution

RFD Rear-Flank Downdrafts

SPC Storm Prediction Center
SRH Storm-Relative Helicity
SST Sea Surface Temperature
SW south-westerly flow
SWEAT Severe Weather Threat Index
SWI Szilagyi Waterspout Index
SWN Szilagyi Waterspout Nomogram
SWT short-wave trough

TT Total Totals index

WDM6 WRF Double-Moment 6-class scheme
WRF Weather Research and Forecasting
WSM6 WRF Single-Moment 6-class scheme
WSMMPs WRF-Single-Moment-Microphysics schemes

1

Introduction

One form of renewable energy, wind energy is widely used all over the world, including onshore wind farms and offshore wind farms. Offshore wind speeds are in general higher compared to on land. Therefore, offshore wind power generation leads to a higher amount of energy. According to the report from International Renewable Energy Agency (IRENA) in 2019, the cumulative installed offshore wind power capacity was approximately 23.4 GW in total worldwide, and near 80% capacity was installed in Europe by the end of 2018. European governments are committed to making Europe become the first climate-neutral continent. To be specific, greenhouse gas emissions are planned to be reduced by 80-95% by 2050 in Europe. In order to achieve this goal, wind power will become one of the main contributors to an increasingly stable form of power supply. Northern Europe is the place with most of the largest offshore wind farms over Europe. About 60% of the world's offshore wind installations are installed in this area. The North Sea accounts for 77% of all offshore wind capacity in Europe (WindEurope, 2020). Several countries, including the United Kingdom, the Netherlands, and Belgium, have constructed wind farms over the North Sea. Figure 1.1 shows the location of offshore wind farms over the North Sea.

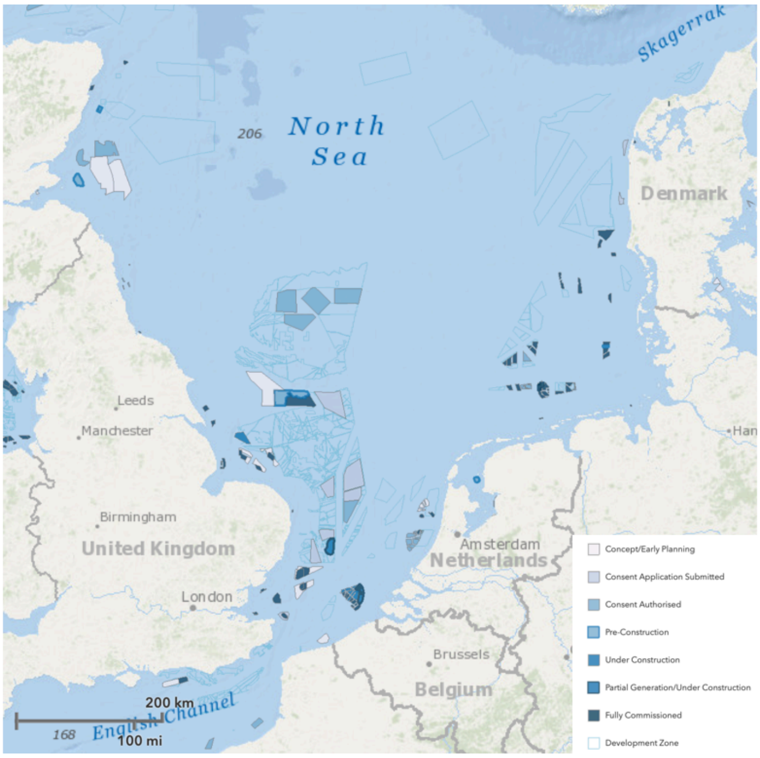

Figure 1.1: A map of offshore wind farm installations over the North Sea (Source: 4C Offshore, 2019)

As the leader of offshore wind power, Europe installed 3,623 MW offshore wind power capacity in 2019. At the end of 2019, the cumulative offshore wind capacity was 22,072 MW (WindEurope, 2020). The Dutch government aims to have 14% of all energy used in domestic from renewable sources in 2020, and a minimum of 27% by 2030. Because of the successful offshore wind energy policy in the Coalition Agreement and the Climate Agreement (2019), offshore wind farms will generate about 11 GW by 2030, which equals 40% of current electricity consumption.

With the increasing density of wind farms over the North Sea, concerns regarding extreme wind phenomena are also growing. Waterspouts are one of the potential threats for offshore wind farms. A waterspout is defined as an intense column vortex that occurs over water surface like an ocean or a lake and is suspended from a cumuliform cloud (Figure 1.2). In general, it is a non-mesocyclonic tornado, which means that it does not usually require a supercell to form. Although waterspouts in the North Sea have been studied since the early 1900s (Owen, 1946), only some basic records exist. Besides, several research studies discussed the tornadogenesis, thermodynamic environment, and atmospheric conditions of waterspout formation in Florida, the Great Lakes, the Central-Eastern Mediterranean, the Adriatic Sea, and the Baltic Sea. However, the literature on waterspouts in the North Sea is virtually nonexistent. Therefore, the North Sea was selected as the research area of this study.

Figure 1.2: A waterspout at Walney Windfarm in 2015 (Photo by Chris Hall)

For waterspouts, there is a solid shell rotation outside, and a weakly forced downward movement in the center. A much stronger rain-cooled downdraft is usually presented near the waterspout (Golden, 1974). Based on the findings from Davies (2006), Doswell (2001), Markowski and Richardson (2009) and Renko et al. (2016), waterspouts usually develop in an unstable environment with low cloud height with a low wet layer in the boundary layer, pre-existing vertical vorticity over a boundary and strong vertical wind shear. Therefore, thermodynamic parameters and wind conditions will be used in this study to analyze the favorable environment for waterspout formation. These parameters are simulated by a Numerical Weather Prediction (NWP) model, the Weather Research and Forecasting (WRF) model, with five different microphysics schemes. Radar data, radiosonde data, lidar measurements, and satellite images are used for comparison. Besides, synoptic charts are also needed to identify the circulation patterns.

Szilagyi (1994) developed a practical tool, based on observational data from the Great Lakes region, called the Szilagyi Waterspout Nomogram (SWN). The original nomogram has been continuously updated over the years. At present, it is operationally utilized by the meteorologists in North America.

According to the general environment of waterspout occurrence, it would be ideal for measuring relevant data for a whole process of waterspout development. Nevertheless, in order to find a better location of observation, the first step is to detect these features on a relatively small scale. Therefore, this study uses data from simulation results. The research questions are thus specified as follows: to what extent is the WRF model capable of detecting a favorable environment of waterspout development? To answer this, the following sub-questions are to be covered:

- To what extent can high-resolution (1 km grid size) simulations capture the mesoscale characteristics of the waterspout occurrence area?
- What are the strengths/weaknesses of various microphysics schemes to simulate the waterspout environment?
- How well can the Szilagyi waterspout nomogram technique perform for the North Sea region?

The organization of this thesis is as follows. Chapter 2 starts with a review of waterspouts in detail according to previous research, and then introduces all the parameters used in the following analysis. Besides, the details of the five selected microphysics schemes are presented in this chapter. Chapter 3 will briefly introduce the study area and describe all the observation data. Chapter 4 will show the WRF model setting applied in this study. Chapter 5 and Chapter 6 will give the final results and analysis of two waterspout cases over the North Sea. Chapter 7 will conclude the study's performance, the limitation of this study, and some suggestions for future work.

2

Literature Review

In this chapter, the aim is to provide the relevant knowledge of waterspouts and the risks associated with this phenomenon. The entire chapter is organized as follows: Section 2.1 presents an introduction of waterspouts, including properties, the potential threats, and previous research. Section 2.2 covers an overview of the most frequently used thermodynamic parameters for waterspouts' analysis. Finally, relevant wind shear parameters are discussed in Section 2.3.

2.1. Waterspout

A tornado is one of the most mysterious and elusive meteorological phenomena, especially during the warm season. It can be defined into two types based on the surface of occurrence. The one that occurred over lands is called a tornado or a landspout, and the other one occurring over the water surface is called waterspout, which is the topic of interest of this thesis.

Tornado reports in Europe are recorded in the European Severe Weather Database (ESWD). Groenemeijer and Kühne (2014) published their major survey of a climatology of tornadoes in Europe. According to their research, Figure 2.1 shows that the coast of the North Sea presents a high frequency of events. Due to the scarcity of observational data over the offshore region, this spatial distribution of waterspouts may not be comprehensive.

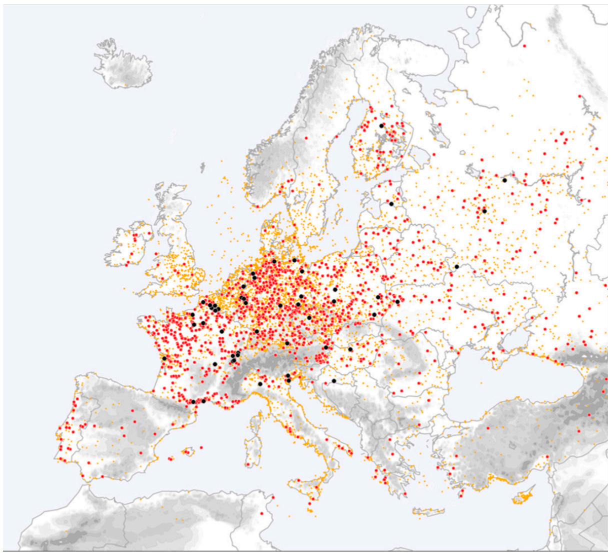

Figure 2.1: Tornado reports in the the ESWD for Europe. Orange shows weak (F0, F1) and unrated tornadoes; red represents strong (F2, F3) tornadoes; and black points are violent (F4, F5) tornadoes (Groenemeijer and Kühne, 2014)

2.1.1. Definition and formation

Waterspouts are natural phenomena that are both fascinating and horrifying events. It is a tornado over a water surface, but weaker than land tornadoes due to the differences in atmospheric dynamics. Often, waterspouts are always observed without any visible cloud (Golden, 1977). Due to the lack of observers in the open ocean, most of the witness reports of waterspouts are from the coastal and inland areas. It is very likely that these events occur much more frequently and are presented in various offshore regions around the world. Figure 2.2 is a photo of the waterspout that occurred in West-Terschelling Netherlands near a local wind farm called the Nordsee One wind farm on 13^{th} of August 2019.

Figure 2.2: A waterspout near wind farm on August 13 2019 (European Severe Weather Database, 2018)

A waterspout does not last more than 30 minutes in general. They typically form over warm water, and these warm temperatures are essential to the development of waterspouts. As the warm air evaporates, it becomes rising humid air, then clouds form. This causes a slower cooling rate than dry air and leads to instability. Simultaneously, moderately strong updrafts in the clouds and the inflow to the rising air of these clouds encounter shifting winds near the water's surface. The converging inflow can form a vortex, and with increasing entertainment, then waterspout is formed.

To better understand the mechanisms of waterspouts formation, Golden (1974) analyzed the characteristic life cycle of waterspouts. In his research, five discrete but overlapping stages are regularly shown in the life cycle of waterspouts, (1) the dark spot stage; (2) the spiral pattern stage; (3) the spray ring stage; (4) the mature stage and (5) the decay stage. To begin one process, the sea-surface shows a noticeable light area surrounded by a dark appearance where the vortex or column of rotating wind reaches it. The second step in this process is to show a light and dark band spiral ring around the dark spot. Then, a concentrated spiral ring forms around the dark spot. An eye will appear in the center, analogous to the eye of a typhoon but much smaller. In the follow-up stage, the waterspout comes to its most intense stage. During the formation of a matured vortex, a rotating column is formed from the sea surface to the clouds overhead, characterized by a hollow funnel, and sometimes surrounded by water vapor. At the final stage, the waterspout dissipates when the strength of warm air vortex flow becomes weaken. Figure 2.3 is a sketch of the life cycle.

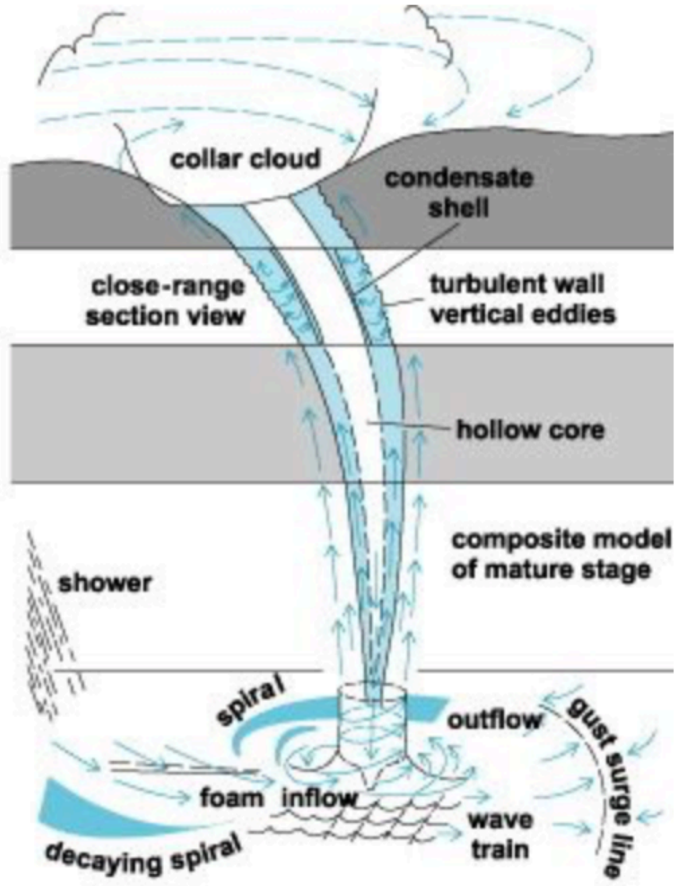

Figure 2.3: Illustration of a waterspout life cycle and structures (Higgins Storm Chasing, 2019)

2.1.2. Categories

Waterspouts are generally a form of non-mesocyclonic tornados that are thought to develop by the stretching of pre-existing vertical vorticity along surface convergence boundaries, such as fronts and outflow boundaries, or wind-shift lines (Figure 2.4). In contrast, the tilting of vorticity and subsequent stretching is the primary mechanism for supercell tornadoes (Wakimoto and Wilson, 1989). Waterspouts can be usually separated into two categories: thunderstorm related waterspout and fair weather waterspouts.

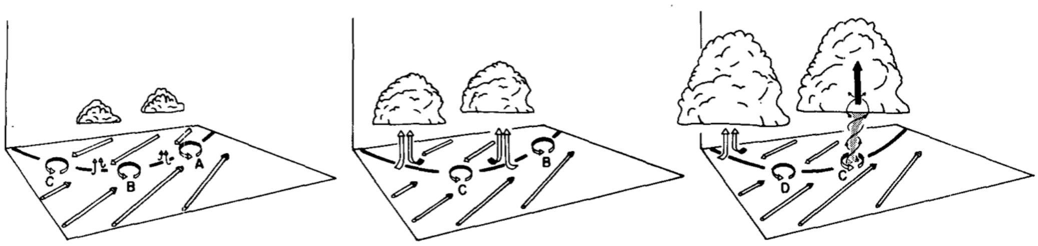

Figure 2.4: The formation of a non-mesocyclonic tornado along a convergence line (Wakimoto and Wilson, 1989).

Thunderstorm related waterspouts are also called tornadic waterspouts. As is shown in the name, this type of waterspouts has the same characteristics to a land tornado except occurred over the water surface. Sometimes cumulonimbus clouds or thunderstorms form over open water, and funnel cloud can be seen over the waterspouts. These columns of spinning air extend downwards from the cloud and touch the water surface, then forming waterspouts. They are usually influenced by high wind speeds associated with severe weather, such as thunderstorms, rising air, vertical axis rotations, and dangerous lightning. The presence of lightning is the most straightforward approach to identify tornadic waterspouts from fair-weather waterspouts. Thus, thunderstorm related waterspouts are the stronger and more devastating type of waterspouts. Figure 2.5 (Left panel) is an ideal schematic of a tornadic waterspout.

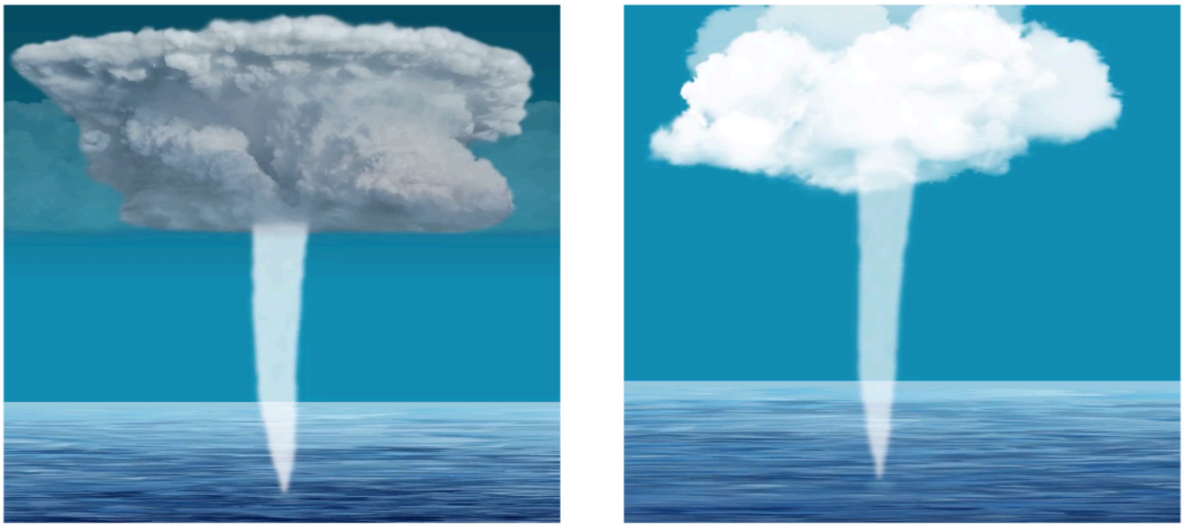

Figure 2.5: (Left panel) Schematic diagram of thunderstorm related waterspouts, (Right panel) Schematic diagram of fair-weather waterspouts (Met Office: Learn About Weather, 2018).

Fair-weather waterspouts are much more common in nature (Renko et al., 2016). Fair-weather waterspouts usually form along with cumulus congestus or developing cumulonimbus clouds (Figure 2.5 (Right panel)). According to Golden's (1974) research for 72 waterspouts over Florida keys in 1969, at least 90% of the waterspouts are formed by rapidly developing cumulus cloudlines. And the spiral patterns are shown on the flanking edge of one cloudline as well as a rain shower. Fair-weather waterspouts belong to the non-mesocyclonic tornado over warm water, which is related to developing storm systems, but not storms themselves. The extra ingredients for fair-weather waterspouts are cooler air and wind shear. The former allows warm and moist air to rise and then to condense. The latter allows the rising air column to spin because of the changing of wind direction with height. This vortex of cloud droplets forms and extends from sea surface to the base of cumulus clouds, which is opposite to thunderstorm related waterspouts. As for this type of waterspout, the term fair weather comes from fair and relatively calm weather when it occurred. It always occurs during morning hours except for noon, as well as in the late afternoon.

Formation of both thunderstorm related and fair-weather waterspouts requires high levels of humidity and a relatively warm sea surface water compared to the overlying air. The occurrence of lightning during waterspouts can be used to distinguish the waterspout category (Manzato, 2007). This criterion is used because we want to emphasize that a large number of the waterspouts occur beneath cumulus congestus cloud or cumulus mediocris clouds. These kinds of clouds are usually associated with convergence lines (Renko et al., 2016).

2.1.3. Hazard

Waterspouts look like fabulous funnels, but in fact, these are dangerous meteorological phenomena. Although the occurrence of waterspouts is surprising to witness, it has some potential possibilities to cause significant damages and injuries to people as well as to properties. Specifically, the waterspouts pose significant hazards to aircraft, mariners, and offshore engineering structures, including turbines.

In the aviation industry, whenever an aircraft encounters a waterspout, there will be enough severe turbulence to cause structural damage, injure crew and passengers, and even lead to loss of control. Waterspouts can cause some fatal consequences at the surface of the sea. According to the Air Accidents Investigation Branch (AAIB) incident report, there was an accident on 28th February of 2002 (SKYbrary, 2019). The tail pylon and the tail rotor blades of a super puma helicopter were damaged when it encountered severe weather generated vortices associated with a waterspout over the North Sea near Scatsa in the Shetland Islands.

Another effect of waterspouts is posing threats to mariners (Figure 2.6). Although intense waterspouts are not common, several incidents were mentioned in the historical records. On 4 September 1970, a tornadic waterspout occurred in Venice, Italy. This waterspout killed 36 people because it lifted a motorboat from water and threw it to the bottom of a lagoon in a short time (Wikipedia, 2020). Another one occurred on 12 July of 1995, a tornadic waterspout started from south St Petersburg, Florida, and caused a loss of 200,000 dollars (Collins et al., 2000).

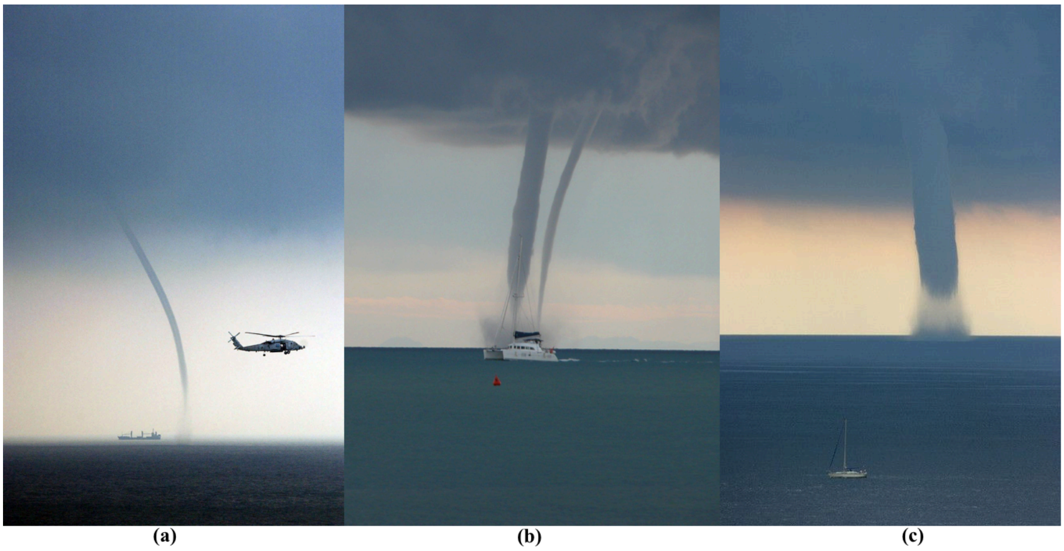
(a) (b) (c)

Figure 2.6: Waterspouts passed close to ships photographed by Richard R. Waite, September 5, 2004 (a), Sailing Journal, March 3, 2019 (b), NWS NEXRAD, April 2009 (c)

Except for the aforementioned concerns, waterspouts also pose an unknown threat for wind turbines in offshore wind farms. The primary standard for wind turbine structural design requirements is International Electrotechnical Commission (IEC) 61400-1 third edition (IEC, 2005). This standard contains many aspects, including design classes, environmental conditions for each class, Design Load Cases (DLCs), fault condition, electrical requirements, and to assess the site-specific suitability of a turbine. This standard also highlights the importance of detailed characterisation of turbulent wind environment. Understanding wind characteristics is important to assess unsteady aerodynamic load distributions along with the rotating blades. The IEC and a working group (TC88) started to develop a guideline for offshore wind turbines in 2000. TC88 declared their objective that to develop international, engineering and technical design requirements for offshore wind turbines, IEC 61400-3 (IEC, 2009). The design of an offshore wind turbine must be based on wind conditions. In 2018, IEC accepted a new global wind farm Technical Specification, IEC/TS 61400-28, by considering the maintenance of wind farms and their life extension. TC88 believes that the new Technical Specification will promote standardization. As a consequence, the uncertainty of wind farms damaging and the cost of electricity generated will decrease. This technical standard will be published in 2020.

IEC uses a 50-year return period for the definition of extreme design condition. The 50-year extreme 10-min average wind speed should be the reference. The extreme wind speed is often associated with the “survival wind speed” of the wind turbine. The exhibiting extreme wind speeds, shear factors, and turbulence should be taken into account, when designing the turbines. However, some less known severe weather phenomena, such as waterspouts, are very difficult to be predicted. We can not compute the possibility that the vortex center accurately hits a single wind turbine because of the computational burden. These conditions are able to prove catastrophic. With the horizontal wind shear across the whirlpool center, even a near-pass by a waterspout might be dangerous and risky for a wind turbine (Dotzek et al., 2010). It is unclear that if the small scale wind field in a wind farm altered by the wind turbine wakes themselves may increase the likelihood of a hit once a waterspout enters an array of wind turbines (Christiansen and Hasager, 2005). Thus, wind farms should be considered as a whole rather than any specific wind turbine. Although there is no severely damaged case caused by waterspouts so far over the North Sea, a waterspout is still a potential threat for wind turbines, causing damage to the blades or other components with the increasing density of offshore wind farms. Hence, more research is necessary for the understanding and characterization of waterspouts.

2.1.4. Findings from previous studies

The frequency, spatial and temporal distribution, thermodynamic properties, and meteorological environment favorable for developing waterspouts have been provided in many areas of the world. Until recently, minimal research focusing on the occurrence of waterspouts over the North Sea has been conducted.

Golden (2003) reported that the Florida keys might be one of the locations with the highest frequency of waterspouts in the world. Because of this fact, the Florida Keys also is called the capital of waterspouts. A note of caution is due here since only a small percentage of the waterspouts can be observed and recorded. At this location, waterspouts occurred and were reported every month of a year, especially in the wet season between June to October. The formation of waterspouts possibly is influenced by the mesoscale. According to National Oceanic and Atmospheric Administration (NOAA)'s observations between 1969 and 1972, 90% of waterspouts that occurred over the Florida Keys are spawned by a quickly built cumulus cloud line. Usually, the vortex is formed on the cloud line's flanking edge, and a rain shower is nearby. Besides, the synoptic conditions are associated with waterspout-active convective cloud line development. For lower-level intense anticyclonic conditions, the cumulus cloud line development is inhibited by subsidence. As for a robust cyclonic condition, the surface heating mechanism is disrupted by strong winds and vertical wind shear at lower levels. All in all, irrespective of the type of waterspouts, there is always a weak but well-defined trough line through the location of the occurrence of the waterspout events.

Dotzek (2003) surveyed the number of tornadoes and waterspouts that occurred in Europe in 25 countries. He found that the frequency of occurrence for each country is not only related to its size; other factors also have contributions, such as climatology and historical record. Wegener's statistics can prove this result. For example, the Netherlands' coastline is relatively short; its territorial area is relatively small compared with others in Table 2.1. However, the number of waterspouts in the Netherlands is not small at all (Wegener, 1917). Another condition is that some countries have just started recording their statistics. Not surprisingly, their average numbers are relatively small. Table 2.1 shows the observational records of waterspouts in Europe's top five countries and estimation by observations per-year. The highest number of waterspouts occurred in the Netherlands, Spain, Italy, and the United Kingdom. Spain and Italy are influenced by the Mediterranean Sea, which has a high sea surface temperature. The number of observations or estimation of waterspouts per year was given (Table 2.1). Based on the data from 25 countries in total, there are 160±3 waterspouts each year with witnesses. Note that the observed numbers are generally lower than the number of estimations. The amount of under-reporting of waterspouts is quite large, due to the lack of observers at present. For Germany, waterspouts over the North and Baltic Seas are common from July to September, and no systematic recording occurs. Hence, a significant amount of under-reporting of events around coastal waters may be the reason. For the estimation, an average of 393±11 waterspout events in each year is estimated for 25 countries in Europe. According to the estimated values, the under-reporting rate is more than 58%.

In reviewing the literature about the atmospheric environment of waterspouts, Rossow (1970) pointed out that it is difficult to distinguish between a waterspout day and a non-waterspout day simply based on daily sounding or specific stability indices. Then Golden and Bluestein (1994) found that the thermodynamic sounding shows relatively low wind speed at a low level, light shear, high moisture in the

Table 2.1: Number of waterspouts in Europe (Dotzek, 2003)

Country Name	Observations	Estimations
Netherlands	60	100
Spain	25	150
Italy	25	27
United Kingdom	15	30
Germany	5	20
Total (25 countries)	160	393
Average (25 countries)	160±3	393±11

boundary layer. Furthermore, Spratt and Choy (1994) analyzed sounding data from Tampa, West Palm Beach, and Cape Canaveral between 1979 and 1992, and reported that the favorable conditions for waterspout development include low wind speed at discrete levels as well as total precipitated water vapor levels of more than 4.1 cm. Golden's studies in 2003 stated his worry that a mean sounding climatology could not sufficiently catch the super adiabatic lapse rates observed in the sub-cloud layer of waterspouts.

A study of waterspouts in the Adriatic, Ionian, and Aegean Sea region, from Sioutas and Keul research in 2007, 28 waterspout events' synoptic circulation patterns were examined in the area. These waterspouts were reported from July to November 2002, during which the whirlwind activity is in a high frequency in general. The highest frequent month of Adriatic was in July, August, and September, and the Ionian and Aegean were in September, October and November. Among 28 waterspout events, fair weather cases and thunderstorm related cases are 13 and 15, respectively. Five selected particular synoptic features of waterspouts that contributed to the development of waterspout, activity were examined in the different locations, and a closed low-pressure system at 500 hPa is the most popular type (Sioutas and Flocas, 2003). As for the mesoscale environment, studies used thermodynamic indices, and wind parameters as derived by radiosonde from the closest sites and approximated the time around the waterspout occurrences. The results present in both thunderstorm related and fair-weather waterspout cases, K Index (KI) and Total Totals index (TT) were good predictors of the unstable environment, for both event types and areas.

As was mentioned before, the Netherlands is a place with a high frequency of waterspouts that a significant number of waterspouts occur in the summer season from June to October. There were more than 80 funnel clouds with witnesses in August 2006. With persisting increasing temperature in summer, the temperature of shallow waters in the Netherlands rises quickly, e.g., the IJsselmeer and Waddenzee. The atmospheric environment becomes the favorable “cyclonic” circulations. In order to know more about in which conditions the spout-type funnel clouds will occur, a study started in 2007. As a consequence, Renko et al. (2011) developed an index developed, the so-called KHS index which contains an instability index combining four weighted parameters which are wind shear, lapse rate, average humidity, and 10 m wind speed. Using the four parameters can indicate the risk of waterspouts, which develop over the shallow waters of the North Sea along the coast of the Netherlands.

Szilagyi (2009) developed an empirical technique, known today as the SWN which nomogram is presented in Figure 2.7. The method is based on a massive database covering the period from 1988 to 2005. During this period, 263 confirmed waterspouts events occurred in total over the Great Lakes. This SWN technique uses a nomogram to present the difference between sea surface temperature and the 850mb temperature against the convective cloud depth, which were selected from fourteen parameters as possible correlators to waterspout formation.

Moreover, on this nomogram, a waterspout classification scheme was developed and indicated different types. In order to quantify the likelihood of waterspout occurrence, the Szilagyi Waterspout Index (SWI) was available in Figure 2.8. Values of the SWI range are from -10 to 10, for which the value of larger than 0 indicates a favorable waterspout environment. In the same year, the SWI was tested around Central-Eastern Mediterranean waterspouts by 110 sample waterspout events during the period between 2002 and 2006 (Figure 2.9). The results show 94% of all cases passed the nomogram test. Besides, the majority of waterspout cases were quite related to large values of ΔZ (more than 8500 m) and relatively small values of ΔT (less than 16 °C). This indicates that the dominant mechanism for waterspout formation is dynamic processes. The SWI testing result shows that the highest mean SWI values are 7.0, near 6.5, and 4.0 in the Ionian Sea, the Adriatic Sea, and the Aegean Sea areas, respectively. The SWI value indicates that the majority of waterspout events were non-marginal, marginal waterspout events occur near SWI = 0.

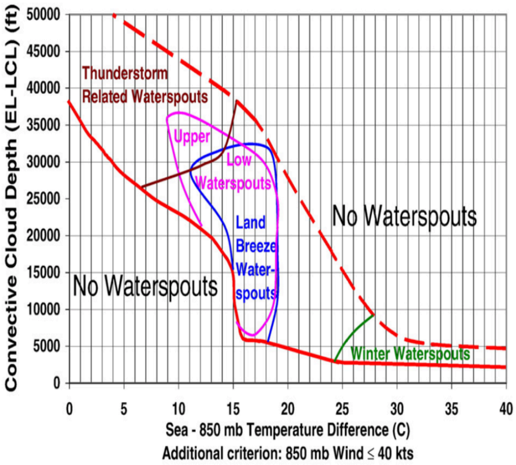

Figure 2.7: The Szilagyi Waterspout Nomogram (Szilagyi, 2009)

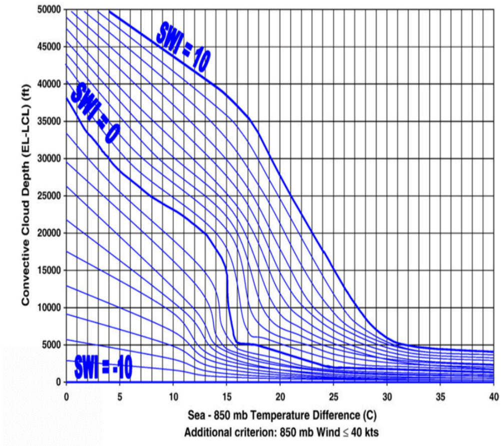

Figure 2.8: The Szilagyi Waterspout Index (Szilagyi, 2009)

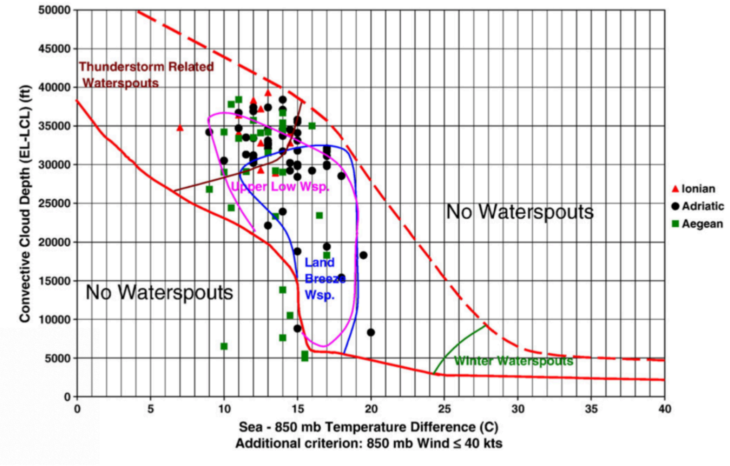

Figure 2.9: Szilagyi Waterspout Nomogram with plotted Mediterranean events of the period 2002–2006 (Dotzek et al., 2010)

.

Wheeler (2009) at National Aeronautics and Space Administration (NASA) Applied Meteorology Unit (AMU) provided a threat level to identify the waterspout's potential of a day. The potential values combined four factors, including monthly climatology, vertical wind profile, precipitation, and persistence, to determine waterspout potential for the day. Three-levels are developed, according to the difference in score, for which the low level is the score from 0 to 8; and the moderate level is a score from 8 to 24; the high level is the score from 24 to 32. This score's goal is to develop a user-friendly interface and clearly show the potential of one day. Watson (2011), did a follow - up research on severe weather in east-central over Florida in the summer of 2010. He reported that it is challenging to distinguish severe and non-severe weather only by several sounding parameters.

Renko et al. (2013) presented the preliminary climatology by synoptic and mesoscale aspects to analyze waterspouts developing in the Adriatic Sea during 2001-2011 and 220 waterspouts occurred in about 100 days from the records. The seasonal distribution shows that the highest occurrence frequency is in summer due to the high convective activity and high Sea Surface Temperature (SST) during that season. For the prevailing synoptic circulations of the 220 waterspout events, the the south-westerly flow (SW) was the highest frequency circulation type (Sioutas and Flocas, 2003). The second highest frequency was the Closed low pressure (CLOSED), with the number of cases quite close to the SW type. As for thermodynamic conditions, radiosounding data, and four instability indices (K Index (KI), Total Totals Index (TT), Severe Weather Threat Index (SWEAT), Convective Available Potential Energy (CAPE)) were monitored, and the results show that the majority of waterspouts (69%) by observation are associated with thunderstorms in this region. The values of KI and TT agree with the values already obtained in the previous studies of waterspouts in the Adriatic Sea (Sioutas and Keul, 2007) while CAPE and SWEAT values show significant deviations from the theories. Besides, the favorable atmospheric environment for the development of waterspouts also show similarities in weak winds and weak shear at lower tropospheric in many previous research (Spratt and Choy, 1994; Brown and Rothfuss, 1998; Golden, 2003; Renko et al.,2011; Sioutas and Keul, 2007; Wheeler, 2009).

Further testing of the SWN method, synoptic, and mesoscale analysis of waterspout were carried out from 2013 through 2016 by Renko et al. (2019) in the Adriatic. The data of their studies were collected in an online survey at the official website of local weather stations in Croatia, and reports with witnesses from newspapers. In total, there are ten waterspout cases occurred in the selected period, and they did detailed research for three of them. The results confirmed that waterspouts could develop in a considerable different value of CAPE, which generally indicates atmospheric environments that can develop convection weather. They concluded that most of the analyzed waterspouts were non-mesocyclonic. As for SWI, this research presents better results for the summer season cases, but relatively large deviations were reported for the winter season cases. A possible explanation for this phenomenon might be that this index was originally developed for the Great Lakes areas. Therefore, when using it at different locations of the world, some adjustments would have appeared. For example, the Adriatic has a higher sea surface temperature in winter than the Great Lakes areas. In order to avoid false alarms, more parameters can be added to SWI fields, such as wind convergence and moisture convergence. However, caution must be applied in a small sample size. The findings could lead to uncertainty for the conclusion, and more observations and measurements should be performed in the study region.

Golden (1974) stated that sea surface temperature gradients might be a key factor in the formation of waterspouts. The sea surface temperatures were measured by the NOAA airplanes. According to Simpson (1983), the sea surface temperature (SST) gradient was 0.5 - 1 °C, which were measured by radiometers on aircraft. The SST gradient was found in a band range no more than 20 km wide. The real gradient may be greater due to remote detection by aircraft. Based on the real measurement, strong SST gradients show a connection with the sea-breeze like convergence that is associated with waterspouts.

2.2. Thermodynamic parameters

Waterspouts are associated with convective instability. The initial perturbation of the flow increases by its positive feedback, and CAPE is converted into kinetic energy. CAPE is defined as the total amount of energy available from buoyancy for an air parcel lifting upward while it expands adiabatically. Due to positive buoyancy compared to the environment, the air parcel will go upward (Pennsylvania State University, 2018). The level of buoyancy starting positive is the LFC, and the ending level of the rising parcel is the Equilibrium Level (EL). Equation 2.1 is used to compute CAPE, which integrates the buoyancy force (B) from LFC to EL. This potential energy for an air parcel to rise can be read from the Skew-T log-P diagram. CAPE is shown the overlap area of the environmental lapse rate and hypothetical trajectory of the parcel from LFC to EL.

$$CAPE = \int_{LFC}^{EL} B dz \tag{2.1}$$

In contrast, Convective Inhibition (CIN) is a measure of the amount of energy required for air parcel to move to LFC. Equation 2.2 is used to compute CIN.

$$CIN = -\int_{z_o}^{LFC} B dz \tag{2.2}$$

The LCL is the pressure level when a lifted air parcel becomes saturated, when lifted dry adiabatically. The height of the LCL roughly equals the cloud base height. Low LCL heights are usually related to the development of tornadoes (including waterspouts). Statistically, the most destructive tornadoes form when LCL heights are in the four- to the six-hundred-meter range. Rasmussen and Blanchard (1998) and Thompson et al. (2003) have recognized low LCL heights play an important role in mesocyclone tornado environment. Recently, Markowski et al. (2002) found high LCL heights are associated with a strong negative buoyant rear-flank downdraft, which interferes with tornadogenesis. However, Davies (2006) has suggested that in the environments with high LCL height and small SRH (explained below) tornadoes can also occur. A tornado is a non-mesocyclone case which can be developed if storm grows rapidly even updrafts are relatively young (Brady and Szoke, 1989).

The rate of temperature changing with height is called the lapse rate. The steeper lapse rate denotes a faster temperature decrease with altitude. The steep lapse rate represents that the atmosphere is unstable. If the value is less than the moist adiabatic lapse rate (5.5-6 °C/km), it is a stable condition; if the value larger than 9.5 °C/km, it is an absolutely unstable condition. The lapse rate between these two values that is conditionally unstable condition. In this study, temperature difference (ΔT) between the sea surface and the 850 hPa level will be used.

The total totals index (TT) is another severe weather index. It is computed using the temperature and dewpoint at 850 hPa and the temperature at 500 hPa as Equations 2.3 (Miller, 1975). VT denotes for the Vertical Totals, and CT is the abbreviation for the Cross Totals. These two components consist of the Total Totals Index. The VT represents the lapse rate from 850 to 500 hPa (T_{850}, T_{500}), the CT uses the 850 hPa dewpoint (D_{850}). As a result, TT accounts for both static stability and 850 hPa level moisture. Additionally, a significant capping inversion might inhibit convection despite a high TT value.

$$\begin{aligned} VT &= T_{850} - T_{500} \\ CT &= D_{850} - T_{500} \\ TT &= VT + CT \end{aligned} \tag{2.3}$$

The K index (KI) is a measure of the thunderstorm potential based on the vertical temperature lapse rate, and the amount and vertical extent of low-level moisture in the atmosphere. It is simply computed from temperatures at 850, 700, and 500 hPa, and dewpoints at 850 and 700 hPa as Equation 2.4 (George, 1960). Generally speaking, the higher the moisture and the greater temperature difference between 850-500 hPa, the larger the KI and potential for convection. However, the dewpoint depression at 700 hPa will cause a low K index. Even the condition below 700 hPa is moisture, unstable air, and a lifting mechanism. In this situation, small KI can still lead to a thunderstorm.

$$KI = (T_{850} - T500) + D_{850} - (T_{700} - D_{700}) \tag{2.4}$$

2.3. Wind shear parameters

Wind shear plays a crucial role in convection because it causes dynamic pressure perturbations. The perturbations have a strong effect on storm development. Vertical wind shear is the derivative of the wind vector with height. Usually, vertical wind shear can be expressed by the difference between the horizontal winds at two specified altitudes or bulk shear. The bulk wind difference over a layer is calculated by vector subtraction (Equation 2.5). For a small value of vertical wind shear, according to Byers (1949), the development of single or ordinary cells can be expected, but lifetimes are relatively short. In contrast, when the shear is large, it is more likely for the occurrence of multicell storms. Doswell III and Evans (2003) gives the median value of bulk shear$_{0-6km}$, slight greater than 20 m/s. This kind of storm usually has more capacity to generate severe weather and a consistently long duration time.

$$\begin{aligned} bulk\,shear_{0-1km} &= \left|\vec{v}_{1km} - \vec{v}_{sfc}\right| \\ bulk\,shear_{0-6km} &= \left|\vec{v}_{6km} - \vec{v}_{sfc}\right| \end{aligned} \tag{2.5}$$

Bulk Richardson Number (BRN) is not good as an indicator of low-level mesocyclone and tornado potential. It is more useful to assess the potential for supercell and middle-level mesocyclone organization. By contrast, BRN shear as the denominator of Bulk Richardson Number, it has a better performance in distinguishing between those supercells that will or will not produce tornadoes. BRN shear can be computed by Eqution 2.6 (Stensrud et al., 1997).

$$BRN\,shear = 0.5(\bar{u}^2 + \bar{v}^2) \tag{2.6}$$

Where $\bar{u}$ and $\bar{v}$ are the wind speed difference between the density weighted 0-6 km mean wind and the lowest 500 m mean wind.

SRH is a measure of the potential for cyclonic updraft rotation in right-moving supercells. It can be calculated for the lowest 1 and 3 km layers above ground level. SRH is a representative of a quantity proportional to streamwise vorticity and storm-relative winds. It is defined by Equation 2.7.

$$SRH = \int_0^h (V - C) \cdot \omega dz \tag{2.7}$$

Where SRH is the storm-relative helicity [m^2/s^2], V is the ground-relative wind vector [m/s], C is the storm motion vector [m/s], ω is the horizontal vorticity vector [s^{-1}], (0, h) is the depth of integration [m], and dz in the vertical dimension [m] (Jones et al., 1990).

SRH has no clear threshold values because of the development of supercells with more relative to the deeper layer of vertical shear. However, if 0-1 km SRH value is greater than 100 m^2/s^2, there is an increased threat of tornadoes with supercells. Research conducted by the Storm Prediction Center (SPC) shows that SRH_{0-1km} values are statistically correlated with the development of significant tornadoes. Research done by Rasmussen and Blanchard (1998), Thompson et al. (2003), and Thompson et al. (2008) have confirmed the SRH can discriminate diagnostically between tornadic and non-tornadic supercells. The 0-1 km SRH seems to have better utility at differentiating thunderstorm types than the 0-3 km. For a recent study, the effective inflow layer technique has been developed by Thompson et al. (2008) as a more realistic estimate of the storm inflow. Effective-SRH calculated based on threshold values of lifted parcel CAPE larger than 100 J/kg and CIN larger than -250 J/kg.

3

Description of Study Area and Datasets

In this chapter, the content is organized as follows: the climatology of North Sea is described in Section 3.1 based on the research investigation. Section 3.2 introduces all observation datasets used in this study.

3.1. Study Area

The area that our research focuses on is the southern North Sea. During the period from June to October, a significant number of waterspouts are typically reported frequently in this region. For example, more than 80 waterspouts were observed in August 2006 in the Netherlands. Especially in the summer months of some years, the sea surface temperature can rise quickly. In spatial weather patterns, which is the favorable environment of waterspouts, many events migt be reported on the same day. According to Reynolds (1999), from 1960 to 1989, approximately 11 waterspouts were recorded pre-year; most of these events occurred near Kent, East Sussex and the Isle of Wight. The followed research in the period 1981 to 2010 by Kirk (2014) found that waterspouts occurred 12.7±2.8 per year and on 8.1±1.5 days yearly. It should be noted that all these reported waterspouts are most likely to be seen during daylight hours. In this thesis, two waterspout events are selected. The time for the first selected case was on September 1, 2017, which is a day of waterspouts outbreak; five events occurred on the southeast side along the coast of Belgium and Netherlands. The second case located near Herne Bay of the UK, and only one waterspout was reported on August 31, 2018.

3.2. Observational Datasets

3.2.1. Weather reports

The European Severe Weather Database (ESWD) is a collection of severe weather reports established by the European Severe Storms Laboratory (ESSL) to provide detailed and high-quality information useful for scientific analysis (Dotzek et al., 2009) and it also provides the data of the selected waterspouts in this research. The severe weather phenomena collected by ESWD include large hail, tornadoes (including waterspouts), heavy rain, and severe wind gusts. Tornadoes (both land and sea) have been reported from all regions of Europe. The areas with the highest density tornado are in western and central Europe. Based on the documented tornadoes, the highest frequency time of a day of waterspouts occurrence is 15-16 and 09-10 local time. The average annual number of fatalities tornado is approximate between 10 and 15 in Europe.

ESSL reviews all reported events after the general public submission. They delete the non-accurate reports and classify the rest of the events into four different quality levels as Table 3.1. Additionally, ESSL has an annual review to check the review work at the beginning of a year. Simultaneously, the data for the specific year can still be modified, updated, or delayed if there is some new information. In this study, the quality level of the two selected cases is defined as QC1.

Table 3.1: ESWD event quality level

Quality level	Description of the level
QC0	as received.
QC0+	plausibility checked.
QC1	confirmed by reliable source.
QC2	verified through detailed analysis.

3.2.2. Radiosonde data

A publicly available repository of the University of Wyoming was used in this study (The University of Wyoming, 2020). The sounding data sets containing the data of temperature, dewpoint temperature, potential temperature, equivalent potential temperature, virtual potential temperature, wind speed, wind direction, and relative humidity from the surface to about 100 hPa. The upper air data can be downloaded to represent vertical profiles of the atmosphere, which contains global sounding stations and can be traced back to the 1960s. Besides, the summary of thermodynamic atmospheric indices can be checked, and those indices are also a useful source for the researchers. For this study, we have used radiosonde data from three stations around the Netherlands and the UK. Table 3.2 lists the radiosonde data that were used, and Figure 3.1 shows the locations of the launch stations.

Table 3.2: The sounding used in this study

station number and name	Observation time	Station coordinates
10113 Norderney	2017-09-01-12UTC	$53.71^{o}N, 7.15^{o}E$
10410 EDZE Essen	2017-09-01-12UTC	$51.40^{o}N, 6.97^{o}E$
03882 Herstmonceux	2018-08-31-12UTC	$50.90^{o}N, 0.32^{o}E$

Figure 3.1: Locations of the radiosonde launch stations. The selected stations are marked with red circles.)

3.2.3. Radar and satellite imageries

Wetterzentrale (Georg Müller and Rogier Floors, 2020) contains links to various weather maps for Germany and the Netherlands. Daily observations of weather stations in Germany and the Netherlands are available including archived radar and satellite images. Archive of satellite images from EUMETSAT has been available since 2016. For the Netherlands, there are multiple sources of radar images, and one of them is the Royal Netherlands Meteorological Institute (KNMI). Every five minutes, an image is compiled from the observations of the KNMI precipitation radars in Herwijnen and Den Helder.

Buienradar's radar images are also used in the case II study (RTL Nederland, 2020). Buienradar is a Dutch website that uses radar and satellite to display the current precipitation above the Netherlands. The rain radar started to work from 2006.

Different sources of the radar image are used for two case studies. Because the locations of radars are different, and they operate on a different wavelength. Even though the observed time and area are the same, slightly different echos images can be provided.

3.2.4. Lightning data

MyBlitzortung is a web application for a wide range of displays and visualization of lightning (Blitzortung.org Contributors, 2003-2020). The data is imported automatically and can be displayed on demand. In this study, the archive of strike maps and animations for a particular day is used. From Chapter 2.1.2, waterspouts are divided into two types, and lightning is the criterion to judge their category.

3.2.5. Lidar data

Several lidar-based wind datasets are publicly available via TNO (formerly ECN, the Energy Research Center of the Netherlands). In this study, two floating lidars, called HKZA and HKZB, were deployed by Fugro and used at Hollandse Kust Zuid (HKZ) zone. The lidars provided wind profile data between 30 m and 200 m above Mean Sea Level (MSL). The temporal resolution of all the wind time-series is 10 minutes. Moreover, the EuroPlatform (EPL) stations also captured the data on that day. In fact, the floating lidar at Borssele Wind Farm Zone (BWFZ) is a good location that might come with a higher possibility to observe useful information regarding of waterspouts of case study 1. Unfortunately, the floating lidar did not collect data on the expected day in the location shown in Figure 3.2 (Li et al., 2020).

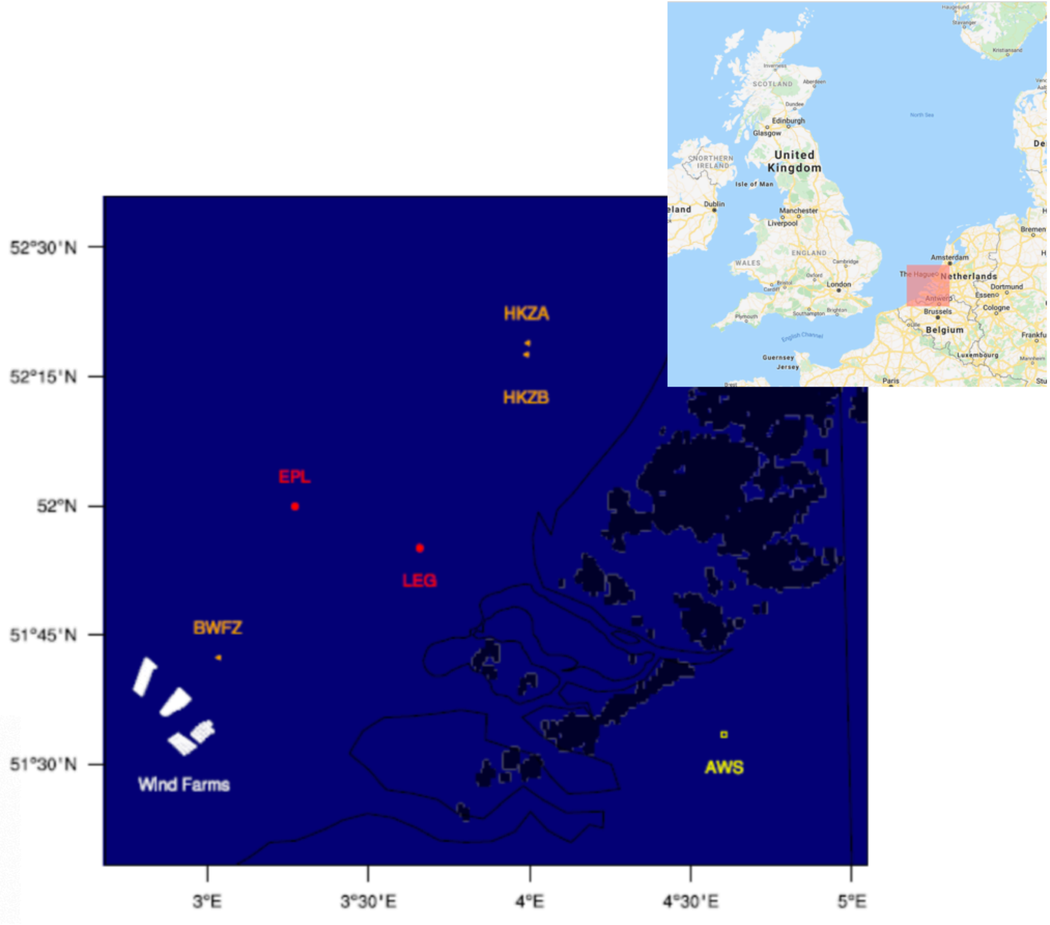

Figure 3.2: Locations of lidars (Li et al., 2020)

4

Model Setup

Based on the research objectives defined in Chapter 1, the literature review presented in Chapter 2, and the area of study introduced in Chapter 3, the settings of the simulation are proposed in this chapter. In order to produce domains that include the entire area of waterspout occurrence on the selected day, the finest domain grid size is 1 km. Besides, five microphysics schemes in WRF are utilized to quantify their impacts. More details of these five microphysics schemes are provided in Appendix A.

The WRF model is a non-hydrostatic model and a state-of-the-art atmospheric simulation system that is convenient and powerful on available parallel computing platforms. One of the essential benefits of the WRF model is that it is open-source, community-contributed code. Because of this benefit, there are a large number of options for physics parameterizations. In this study, the WRF-Advanced Research version 3.9.1.1 was used for simulating the atmospheric conditions associated with the occurrence of waterspouts.

Two waterspouts days were simulated. The first one occurred on September 1st, 2017, from 00 UTC to 12 UTC. Another case happened on August 31st, 2018, from 00 UTC to 12 UTC. The model output was saved every ten minutes. Three nested numerical modelling domains with one way coupling were employed in both simulations. In one way nesting strategy, the parent domain passes information onto the nested domain, but the nested solutions are not communicated back to the parent domain. For the first case, the outermost domain (d01 size: 666 km×576 km) utilizes a 9 km horizontal grid spacing, the intermediate domain (d02 size: 399 km×381 km) utilizes a 3 km horizontal grid spacing, and the innermost domain (d03 size: 145 km×124 km) utilizes a 1 km horizontal grid spacing. The domain configuration is shown in Figure 4.1. As for the second case, the outermost domain (d01 size: 666 km×576 km) utilizes a 9 km horizontal grid spacing, the intermediate domain (d02 size: 273 km×291 km) utilizes a 3 km horizontal grid spacing, and the innermost domain (d03 size: 115 km×97 km) utilizes a 1 km horizontal grid spacing. The domain configuration is depicted in Figure 4.2. All the simulations have 51 vertical levels with nonuniform grid spacing from the lowest model level. To be more specific, it is from approximately 8m to the top of the model, which is about 16km. The model time steps for d01, d02, and d03 were set at 45, 15, and 5s, respectively.

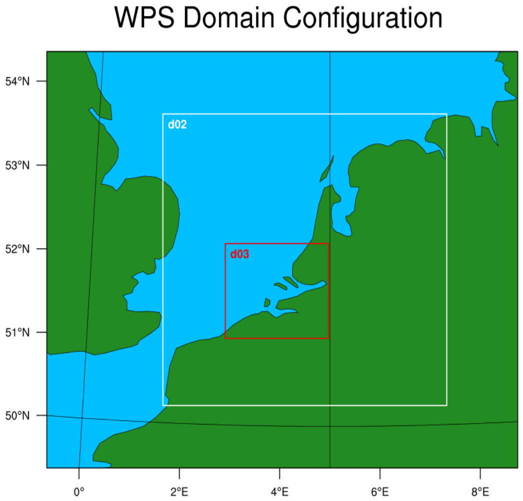

Figure 4.1: The domain configuration of case1

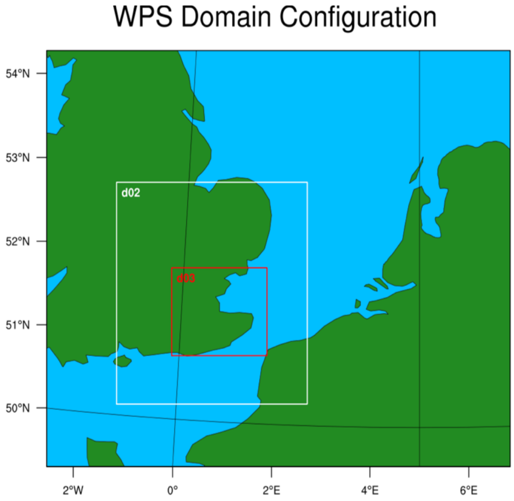

Figure 4.2: The domain configuration of case2

Initial and boundary conditions were provided by the ERA5 reanalysis dataset (ECMWF, 2020), which is from 1979 to within five days of real-time data are available for the public from the European Centre for Medium-Range Weather Forecasts (ECMWF). ERA5 provides hourly estimations of a large number of atmospheric, land, and oceanic climate variables. The data cover the Earth on a 30km grid and resolve the atmosphere using 137 levels from the surface to 80km height. The reanalysis dataset contains environmental data that is recorded from 1979 through the present at a 3-hour interval.

The schemes within the WRF model discussed here include parameterizations for five microphysical processes. The five microphysical schemes, including WRF Single–moment 6–class Scheme (WSM6), Thompson Scheme, Milbrandt–Yau Double Moment Scheme, Morrison2–moment Scheme, and WRF Double Moment 6–class Schemes (WDM6), were examined sensitivity. These parameterizations will be further discussed in Sections 4.1. The detailed setting used in this study is summarized in Table 4.1.

Table 4.1: Details of the modelling configurations

Details of the WRF Simulations				
WRF Run	IC	Grid Size(km)	Time Step(s)	MP Scheme
R1	ERA5	9/3/1	45/15/5	WSM6
R2	ERA5	9/3/1	45/15/5	New Thompson
R3	ERA5	9/3/1	45/15/5	Milbrandt-Yau
R4	ERA5	9/3/1	45/15/5	Morrison 2-moment
R5	ERA5	9/3/1	45/15/5	WDM6

5

Results of Case Study I

This chapter aims to provide the simulated results of the first case in this thesis. The modelled results are presented in this chapter by comparing simulations and observations and then analyzing the thermodynamic environment and wind conditions. To answer the research questions and show the characteristics for a favorable environment of waterspouts, Section 5.1 gives the synoptic conditions at the surface and 500 hPa geopotential height, which provide the current situation, including pressure pattern, fronts, and wind conditions. Subsequently, to demonstrate the difference between simulations and reality, radar reflectivity was used in Section 5.2. Besides, Section 5.3 provides the thermodynamic environment, including some comparisons between observations of atmospheric sounding data and simulated results, and some discussions considering thermodynamic parameters. The following three sections, Section 5.4, Section 5.5, and Section 5.6 elaborate on wind shear, vertical movement, and surface wind three aspects, respectively. In Section 5.6, measured lidar data are used to compare with simulations. Finally, Section 5.7 shows the Szilagyi Waterspout Nomogram test result for this case.

In the historic severe event records from the European Severe Weather Database (ESWD), six tornado events were observed on September 1, 2017. Five of them occurred overseas, which belong to waterspouts (Figure 5.1). This is a day of waterspouts outbreak day. Figure 5.2 shows all offshore wind farms located in the target area, in which the dark blue represents fully commissioned, the blue represents under construction, and the light blue show consent authorized. The first documented waterspout started at 8.15 UTC ±5 minutes near Duinbergen Belgium is shown in Figure 5.2. The following waterspout is reported in these two areas at 8.45 UTC ±5minutes. After one hour, another three events were reported. Two events were reported at Neeltje Jans, whereas the other one was reported at Domburg Netherlands at 9.40 UTC ±15minutes, 10.10 UTC ±5minutes, and 10.16 UTC ±30 minutes. Furthermore, all these reports belong to a reliable source (QC1), and some of them are shown in Figure 5.4, photographs of waterspouts were taken by Luc Van Den Eynden and Bart Michiels on the Belgium coast. Figure 5.4 implies that at least one waterspout goes through a wind farm or close to a wind farm. According to archive lightning records (Figure 5.3), there were lightning strikes in this area. Hence, these waterspouts were associated with thunderstorms. Note that results corresponding to 10:20 UTC are discussed as an example in this chapter, and plots regarding the other four times have been presented in Appendix B.

Figure 5.1: Waterspout events from ESWD (red del:tornado, blue circle:heavy rain), September 1, 2017

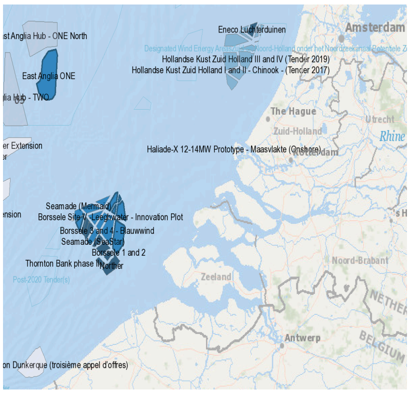

Figure 5.2: Wind farms near the locations of waterspout events (4C Offshore, 2019)

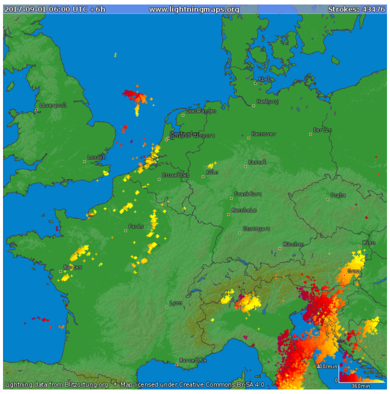

Figure 5.3: Lightning Maps, September 1, 2017 (Blitzortung.org Contributors, 2003-2020)

Figure 5.4: Waterspouts photographs from Belgium coast, September 1, 2017
(Photos by Luc Van Den Eynden and Bart Michiels)

5.1. Synoptic analysis

The 500 hPa analysis charts (Figure 5.5 (a), (b)) illustrate a long-wave pressure trough to the west of the interest area, and the trough implies that the upper-level wind was turning over the location of interest. This can be regarded as a typical SW type of synoptic system. From 00 UTC to 12 UTC, the axis of the trough across the North Sea becomes deeper and slightly moves to the east direction. In this type of synoptic conditions, a southwest flow is developed with embedded successive short-wave troughs and ridges. In general, the surface response is a low pressure filed in Figure 5.5 (c), (d). Based on the surface synoptic charts, two points need to be noticed. Firstly, the corresponding surface low pressure can be found from the surface synoptic charts. Secondly, in the region of interest, black lines with no semi-circles or triangles move easterly are conventionally called a trough. Troughs are used to mark areas where the air is particularly unstable. This phenomenon means that the air is quite turbulent or moves around a lot, especially when there is warm air beneath cold air that wants to rise. Additionally, another trough from the northwest direction was shown in the interest area between 00 UTC and 12 UTC.

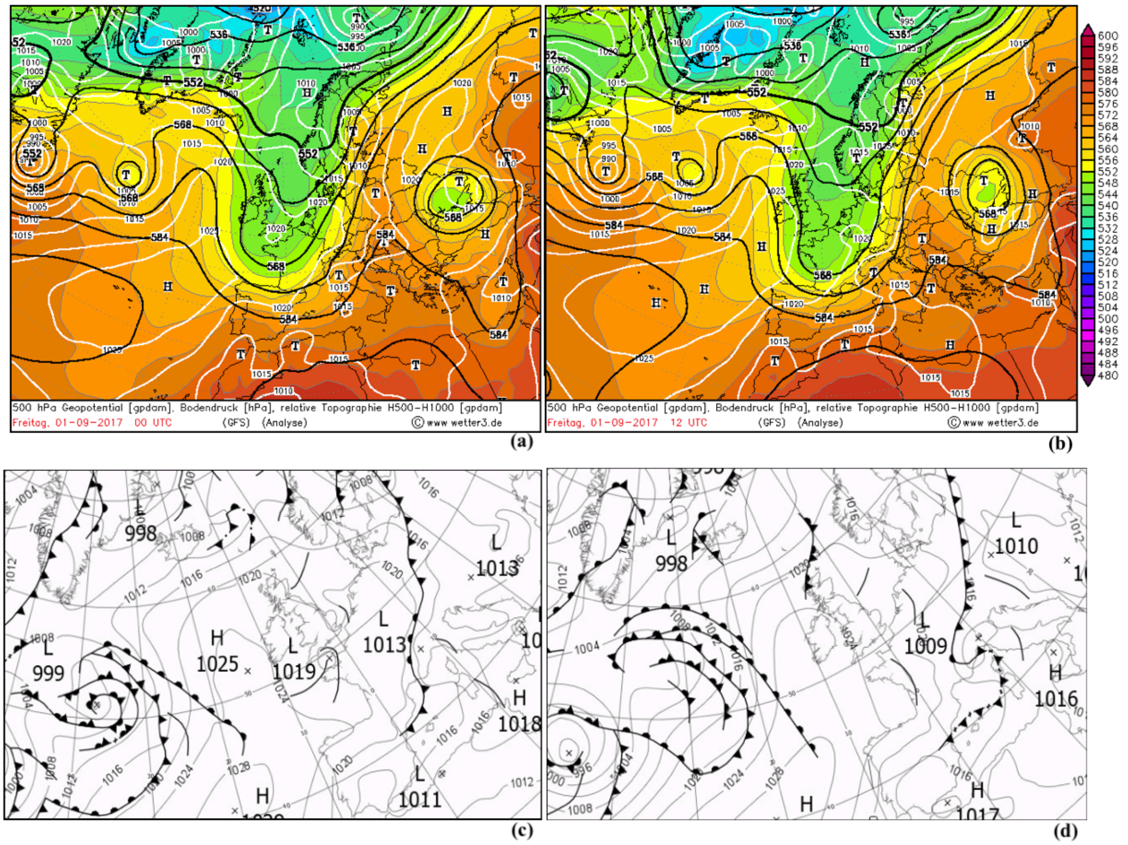

Figure 5.5: (a) Global Forecast System (GFS) analysis at 00 UTC showing geopotential height [gpdm] at 500 hPa (thick bold lines), surface pressure [hPa] (white bold lines) and relative topography H500 - H1000 [gpdm] (shading), (b) Same as (a) but at 12 UTC (R. Behrendt H.Mahlke, Since 2003) (c) Surface synoptic chart at 00 UTC, (d) Surface synoptic chart at 12 UTC (The Met Office, 2020)

5.2. Radar reflectivity with different microphysics schemes

Figure 5.7 presents the spatial distribution of maximum reflectivity from the selected five microphysics schemes of simulated on September 1, 2017, at 10.20 UTC. In contrast to observed radar images (Figure 5.6) from the website wetterzentrale (Georg Müller and Rogier Floors, 2020), the regions which is the same as selected domains are given by red rectangles. Although none of the modeled reflectivity shows a perfect match with observations, the shape and intensity of the simulation can provide some useful information.

Compared with the radar reflectivity figures at 10.20 UTC, both observation (Figure 5.6 (b)) and simulation are given in radar images along with squall line echo in the outer domain and a short squall line shape echo in the inner domain. However, none of the modelled results show this pattern. Instead, simulations for Morrison scheme are more similar to observed radar reflectivity at 11.00 UTC or 11.20 UTC. It was found that only the enhanced reflectivity is presented more east in reality. This can be explained by the fact that results from the simulation are almost one hour earlier than observation. Furthermore, this is in line with Rajeevan et al. (2010), Lean et al. (2008) indicated that in the convection cases based on Met office unified model, the initiation of convection takes place more rapidly as the grid length is reduced. When it comes to results from WSM6 and WDM6, the shapes of the simulated echoes are more close to the radar image at 10.20 UTC. Although the modeled reflectivity for the long squall line had a southeasterly deviation, the short squall line had a northeasterly deviation. Moreover, the WDM6 scheme simulated a stronger reflectivity of more than 50 dBz, and this is a little overestimation. For these two schemes' simulation (WSM6 and WDM6), they are quite similar to reality simultaneously. The rest two simulations show that the shape of the echo is more similar to the radar image at 10.40 UTC. However, the highlighted locations from simulations show more to the west than what is presented in the radar image.

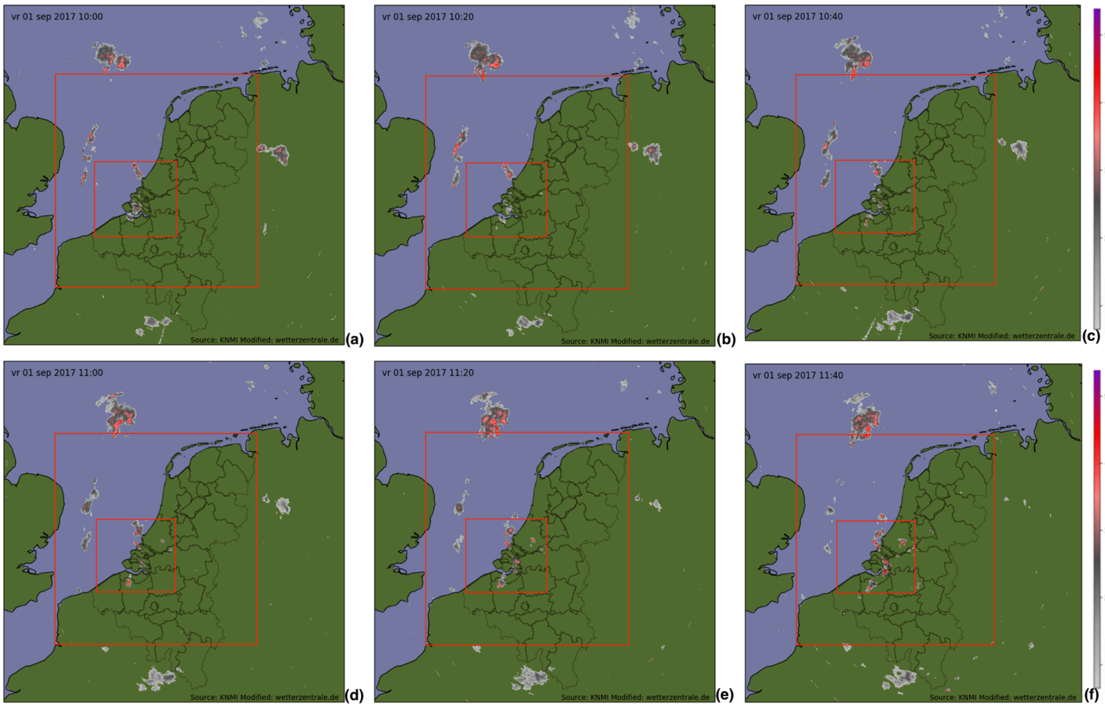

Figure 5.6: Reflectivity [unit: dBZ] from 10.00 UTC to 11.40 UTC (time interval 20 minutes) on September 1, 2017 (Georg Müller and Rogier Floors, 2020)

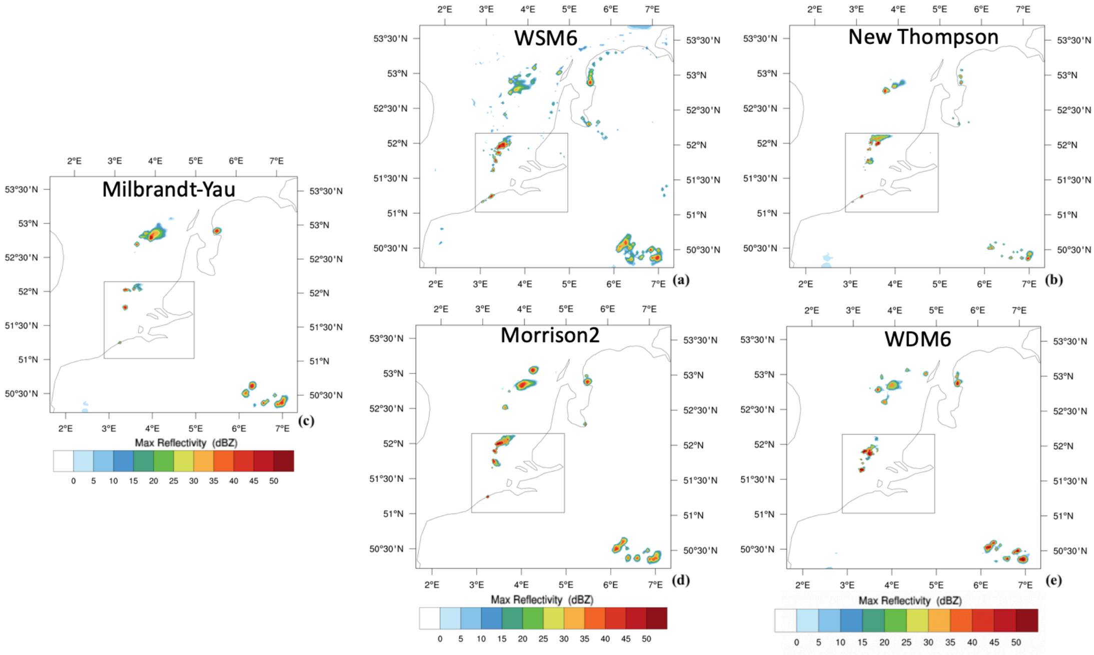

Figure 5.7: Max reflectivity [unit: dBZ] for domain 2 and domain 3 of five microphysics schemes at 10.10 UTC: WSM6 (a), Thompson (b), Milbrandt-Yau (c), Morrison (d), WDM6 (e)

All five microphysics schemes contain cloud water, rainwater, ice, snow, and graupel predictive equations. For these schemes, a general agreement is that the enhanced reflectivity is simulated in the innermost domain. All schemes capture some convection at the northwest part of the finest domain, which runs roughly southwest-northeast. The results of the WSM6 and WDM6 scheme show a squall line slightly curved outward, resembling an archer's bow. This pattern is usually associated with the line of thunderstorms, which is referred to as a bow echo. However, the WDM6 scheme produces higher and more concentrated reflectivity, exceeding 50 dbz. The convective system shape from Morrison double moment is hook echo that appears on the radar as a clockwise, hook-shaped extension as branches. The other two schemes generate several dispersed single cell thunderstorms with less intensity. Moreover, only the result of the WDM6 scheme shows nothing in the southwest of the finest domain. In contrast, the other four schemes produce small spots of simulated echoes near the Belgium coastline.

5.3. Thermodynamic environment

5.3.1. Sounding

In order to assess the results of the simulations, two atmospheric sounding stations, Norderney ($53.71^o N$, $7.15^o E$) and EDZE Essen ($51.40^o N$, $6.97^o E$), are selected for comparisons. The comparison with radiosounding and simulations at these two stations on September 1, 2017, at 12 UTC is presented in Figure 5.8 and 5.9. The skew-T diagrams are used to summarize atmospheric conditions. A skew-T plot is a logarithmic graph of pressure versus temperature in the atmosphere at a given location. In Figure 5.8 of the thermodynamic side, simulations generally show the same as the pattern of observation. For Norderney station, the measured result shows that temperature is almost equal to dewpoint temperature at 800 hPa. This implies that at this level, the environment is approximately near-saturated. Besides, all the five simulations show a near saturation, but their environment is not as moist as observations. And the nearly saturated heights (LCL) are lower than that in reality. Another obvious feature from sounding is that the dewpoint temperature decreases suddenly around 700 hPa level, and model results give a similar feature. However, in the observed Skew-T diagram (Figure 5.8 and Figure 5.9), all simulation shows that the dewpoint decrease to -30 °C around 700 hPa instead of about -25 °C . Moreover, all Skew-T diagrams (Figure 5.8) present that the CAPE areas are more or less of similar size.

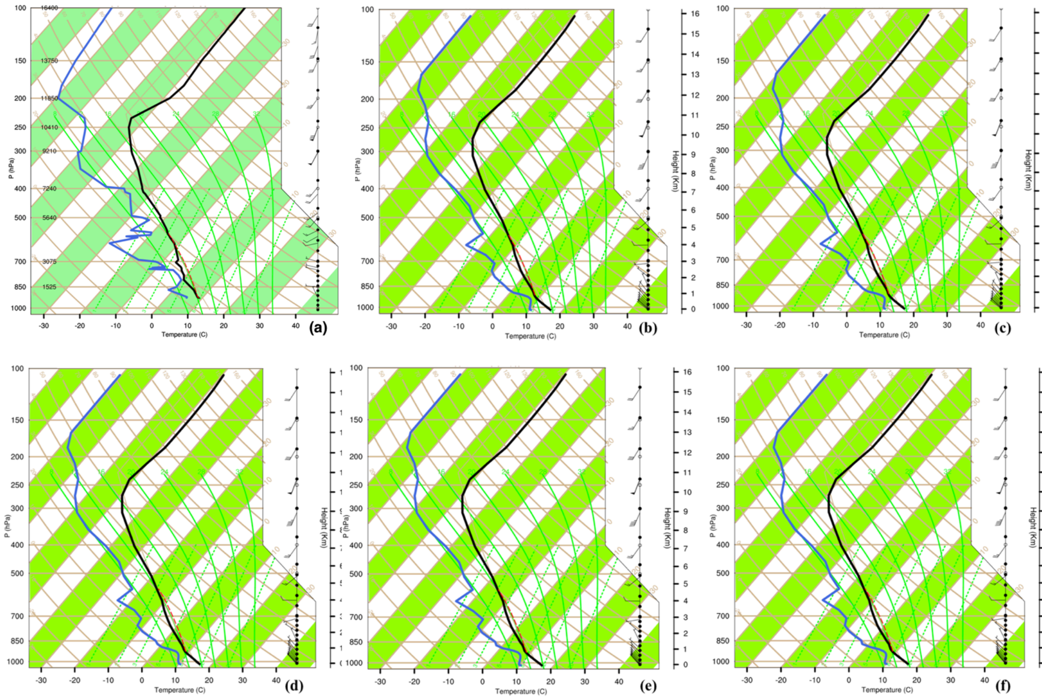

Figure 5.8: (a)Skew-T log-p diagram of radiosounding at Norderney station on September 1, 2017 at 12 UTC (The University of Wyoming, 2020), Skew-T log-p diagram of simulation result by WSM6 (b), Thompson (c), Milbrandt-Yau (d), Morrison (e), WDM6 (f) schemes

Table 5.1: Thermodynamic parameters of September 1, 2017 based on observed and simulated soundings at Norderney station

Parameter	Sounding	WSM6	Thompson	Milbrandt-Yau	Morrison-2	WDM6
EL (hPa)	499.01	542.17	579.63	570.66	587.63	594.16
EL_T (°C)	-20.99	-17.74	-14.08	-14.86	-13.39	-12.97
LCL (hPa)	932.44	932.03	930.97	933.35	926.59	925.05
LCL_T (°C)	9.66	8.81	8.99	9.14	8.74	8.62
ΔT (°C)	13.00	12.47	12.11	12.00	12.03	12.25
CAPE (J/kg)	145	118	118	175	147	147

According to the skew-T diagram from the EDZE Essen station, two clear saturated levels are given by observation. The first level is near 850hPa, and the second layer is just under 700 hPa. Above 700 hPa, the value of dewpoint temperature decline immediately, and it can be noticed that the dewpoint at near 500 hPa is more than -40 °C. However, all simulations did not provide this kind of low dewpoint; instead, those dewpoints are just a little higher than -30 °C. Besides, the simulated results show the same trend. At 850 hPa level, all schemes simulated a near-saturated level at 850 hPa. The observed result shows more moisture below 700 hPa with a drier upper level than the simulation. Furthermore, the CAPE areas of the model are smaller than the measured CAPE, which can be observed clearly in Figure 5.9. Besides, diagrams of Norderney station (Figure 5.8) present a quite similar pattern for observation and simulation in the wind speed and direction part. However, for EDZE Essen station, the real wind direction is more like the southwest rather than the west in the modelled results.

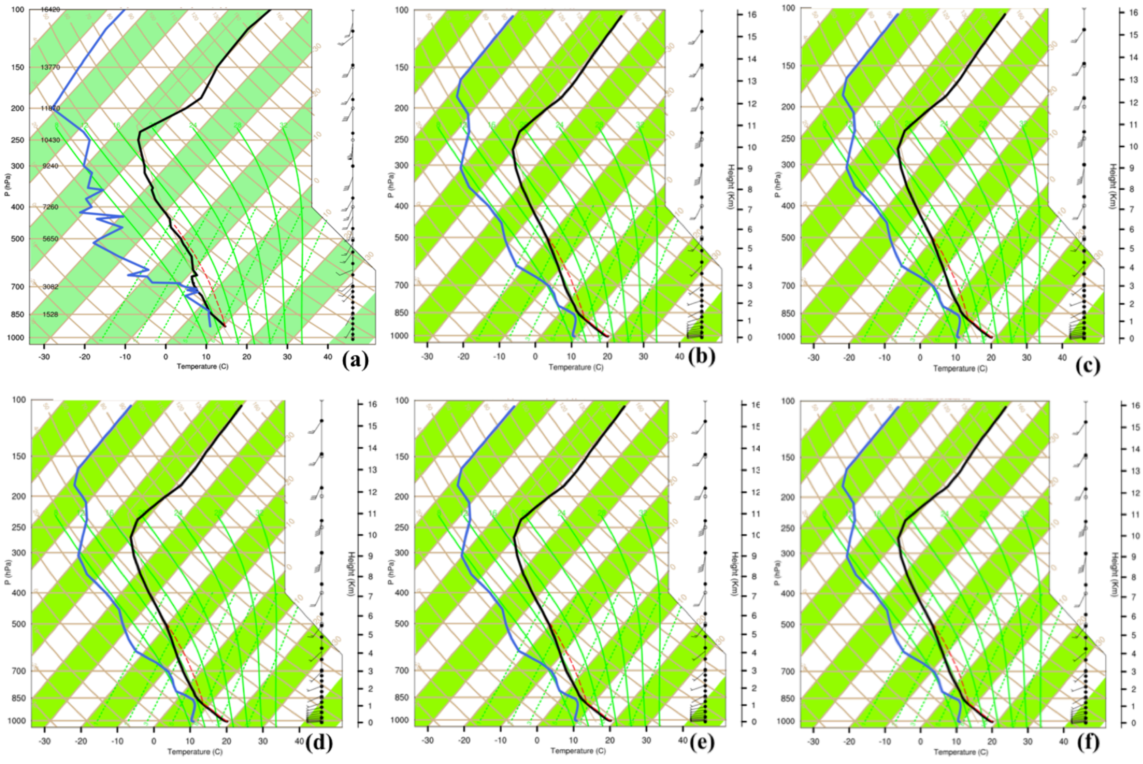

Figure 5.9: (a) Skew-T log-p diagram of radiosounding at EDZE Essen station on September 1, 2017 at 12 UTC (The University of Wyoming, 2020), Skew-T log-p diagram of simulation result by WSM6 (b), Thompson (c), Milbrandt-Yau (d), Morrison (e), WDM6 (f) schemes

Further thermodynamic parameters are provided in Table 5.1 and Table 5.2. The simulated results of Norderney illustrate slightly lower EL heights for all five simulations than the reality and the more or less higher temperature at that height. LCL heights from the model are quite close to true values. It can be noticed that the temperature between the surface and 850 hPa from sounding and the model is also quite similar. Similarly, from the Morrison scheme and the WDM6 scheme, a similar CAPE value can be observed. Table 5.2 show some parameters, including slightly lower modeled EL heights, temperature at the level, in EDZE Essen. Also, simulated LCL and temperature differences are acceptable because they are quite close to the measurement. However, CAPE value was not well simulated, and all schemes' results are underestimated more than 100 J/kg.

Table 5.2: Thermodynamic parameters of September 1, 2017 based on observed and simulated soundings at EDZE Essen station

Parameter	Sounding	WSM6	Thompson	Milbrandt-Yau	Morrison-2	WDM6
EL(hPa)	451.53	514.63	519.54	515.05	515.85	512.00
EL_T(°C)	-25.97	-19.12	-18.60	-19.05	-18.96	-19.38
LCL(hPa)	875.69	872.05	872.00	872.49	872.03	873
LCL_T(°C)	6.47	7.23	7.21	7.26	7.24	7.30
ΔT(°C)	13.40	12.47	13.63	13.69	13.53	13.54
CAPE(J/kg)	432	289	289	298	280	293

5.3.2. Simulation of thermodynamic indies

The MCAPE values in the finest domain are present in Figure 5.10 at 10.20 UTC. According to the scale of CAPE, its value less than 1000 J/kg is weak, or 1000-2500 J/kg is moderate, or 2500-4000 J/kg is strong, and more than 4000 J/kg is extreme range (from Met Office). All the simulated MCAPE distribution is less than 1000 J/kg, which belongs to a weak instability range. This marginally unstable environment is matched with the environment of waterspouts occurrence. One can see that except for simulation of the WDM6 scheme, the other four schemes show their highest values at the same approximate area with MCAPE about 700-800 J/kg. Results from the WDM6 scheme present a smaller activity area and a lower magnitude (about 600-700 J/kg).

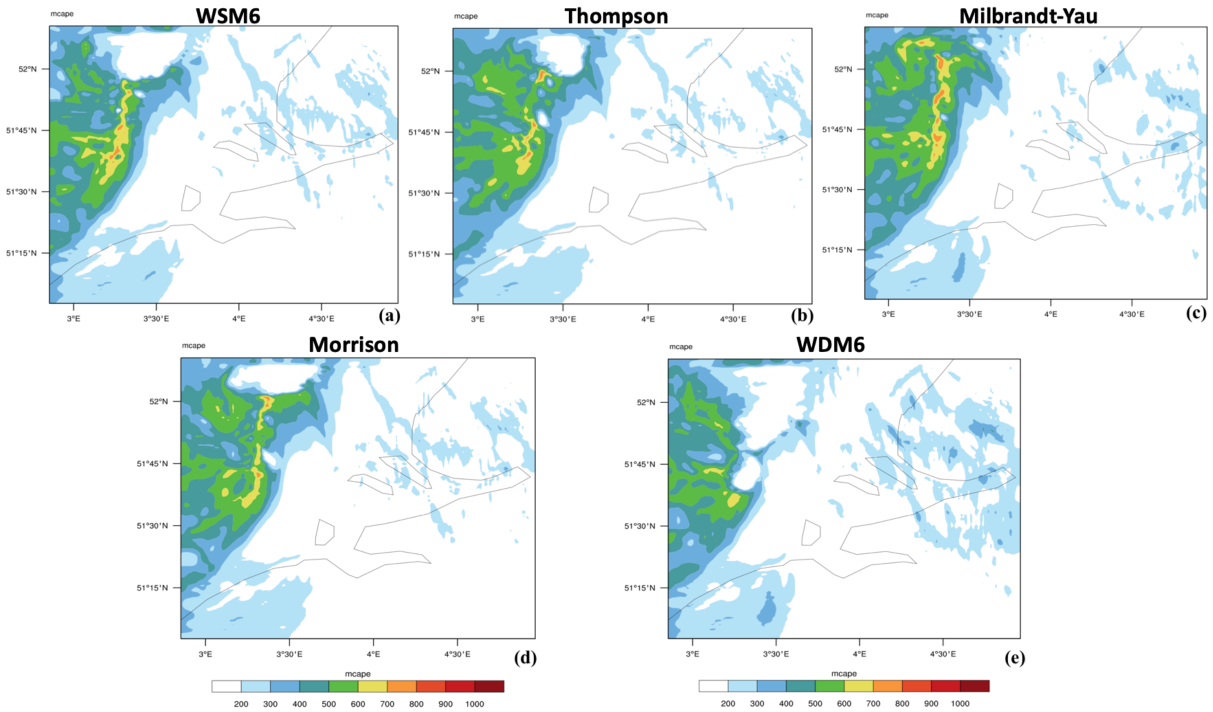

Figure 5.10: Simulated Maximum convective available potential energy (MCAPE) at 10.20 UTC (unit in [J/kg]) by WSM6 (a), Thompson (b), Milbrandt-Yau (c), Morrison (d), WDM6 (e) schemes

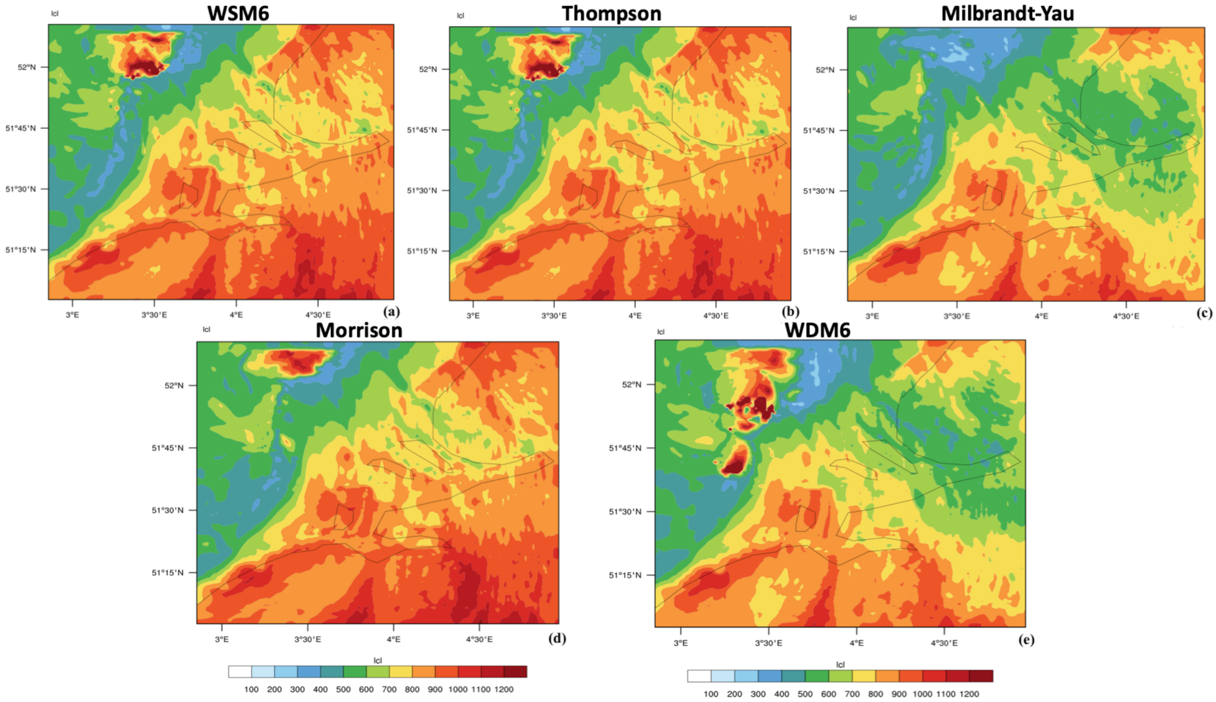

Figure 5.11: Simulated Lifting Condensation Level (LCL) at 10.20 UTC (unit in [m]) by WSM6 (a), Thompson (b), Milbrandt-Yau (c), Morrison (d), WDM6 (e) schemes

Although, Davies (2006) found that there are documented tornadoes from nonmesocyclone process showing a high LCL environment, other studies suggested that tornado environments generally have a relationship with large 0–1 km storm relative helicity (SRH) and relatively low LCL (Craven et al., 2004; Burgess and Foster, 1990) in the past two decades. Therefore, LCL height has been used as a significant feature for tornadogenesis and the height of this situation is less than 800 m (Rasmussen and Blanchard, 1998). In this study, LCL height and SRH between 0-1 km are shown in Figure 5.11 and Figure 5.16 respectively. As we can see, all simulations show lower LCL height (lower than 400 m) at the area that co-located with higher CAPE values (Figure 5.10). However, WSM6, Thompson and WDM6 scheme present several LCL highlighted spots (over 1200 m) near the low LCL area. According to Thompson et al. (2003) and Craven et al. (2004), significant tornadoes can be observed with notably large LCL heights (no more than 2000 m) occasionally. Besides, Davies (2006) found that high LCL situation show some characteristics to distinguish nontornadic and tornadic environment, such as large CAPE. Finally, Markowski et al. (2002) found that higher LCL heights are associated with Rear-Flank Downdrafts (RFD) that are regions of subsiding air on the rear side of the main updraft. The RFD plays an important role in being hypothesized in the tornadogenesis process.

The KI is a measure of the thunderstorm potential based on the vertical temperature lapse rate and the vertical extent of low-level moisture in the atmosphere. Generally, the higher the KI value is related to the more likelihood of thunderstorm development. Note that KI values are empirically divided into three threshold ranges, which are related to severe weather likelihood. The first range is the KI value smaller than 30; the second is the value between 30 and 40 that interpret better potential for thunderstorms with heavy rain. If the value is higher than 40, the potential for thunderstorms with very heavy rain is high. But, if there are very dry 700 hPa level and moist lower layer, thunderstorms with heavy rain or severe weather is possible, even with a relatively small KI value. As we can see in the simulations (Figure 5.12), all schemes provide simulated KI value of about 30 in the area of interest, and the highest value is almost equal to 34. Slight location differences are presented in each scheme's simulation, but the locations are matched with high CAPE and low LCL areas quite well.

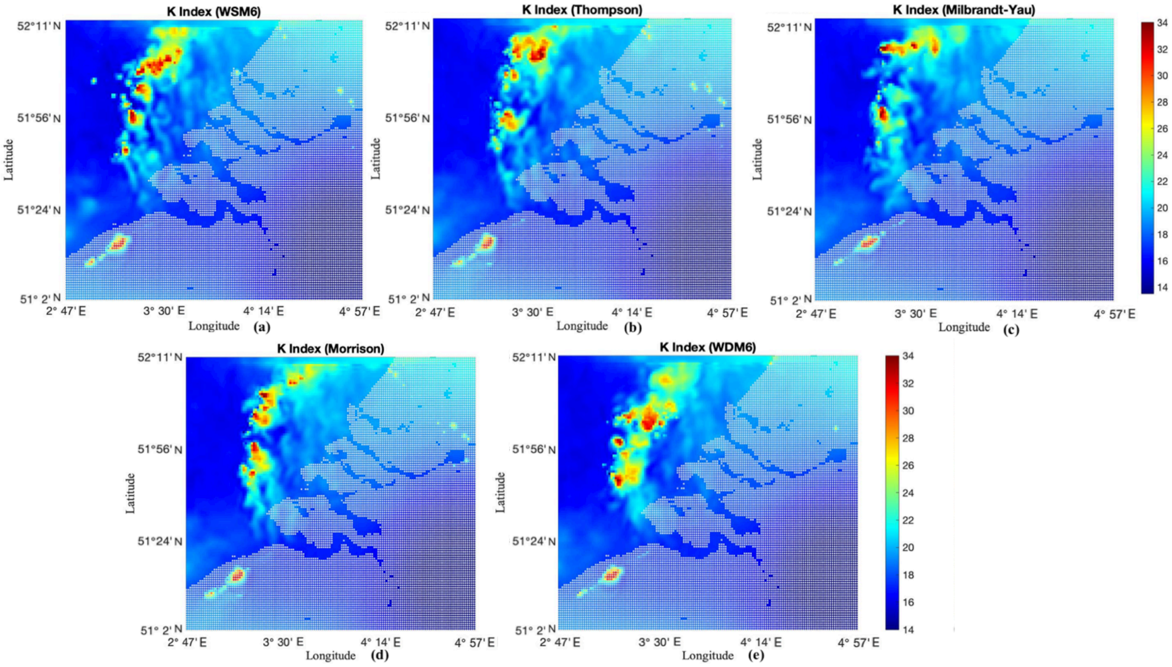

Figure 5.12: K Index at 10.20 UTC by WSM6 (a), Thompson (b), Milbrandt-Yau (c), Morrison (d), WDM6 (e) schemes

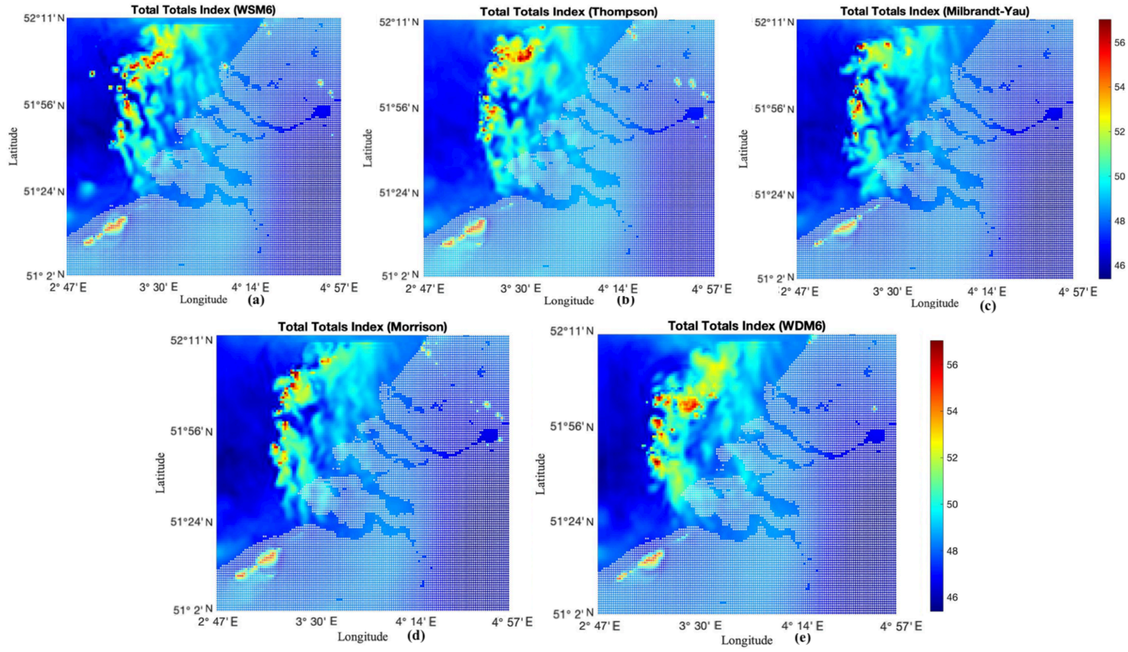

Figure 5.13: Total Totals Index at 10.20 UTC by WSM6 (a), Thompson (b), Milbrandt-Yau (c), Morrison (d), WDM6 (e) schemes

The TT values are empirically divided into three threshold ranges, which are related to severe weather likelihood: the first range is 45-50 that represent thunderstorms possible; the second range (50-55) denote that thunderstorms are more likely, possibly severe values; when TT index is larger than 55, severe thunderstorms are most likely. Figure 5.13 shows the TT index of simulation for five microphysics schemes in the finest domain at 10.20UTC. The high values of TT locations are quite similar to the K index highlight areas that co-located with high CAPE and low LCL areas. Note that the largest TT value near 56 is adopted in all simulations. Compared with other two schemes, WSM6 (Figure 5.13 (a)), Thompson (Figure 5.13 (b)), and WDM6 (Figure 5.13 (e)) scheme simulated larger area with high TT index value. However, the WSM6 scheme presents high-value areas closer to the north, and the WDM6 scheme gives high TT values much closer to the south region in close proximity waterspout events.

According to a statement that has been mentioned in chapter 2, the SST gradient might be an essential ingredient of waterspouts development. All simulations for five schemes at 10:20 UTC (Figure 5.14) show a clear persistent SST gradient in the preferred area at the time of all five reported waterspouts. Nevertheless, differences can be found among the schemes. To be more specific, the simulation of land surface temperatures from the Milbrandt-Yau and WDM6 is lower than the other three. Moreover, the WDM6 and New Thompson schemes present clear surface divergence with lower SST than its surroundings, and the temperature differences are about 2-3 °C. The Morrison and WSM6 schemes show a similar but weaker pattern whose differences are within 1 °C. Overall, what can be learned from here is that waterspouts, to some extent, are related to the SST gradient.

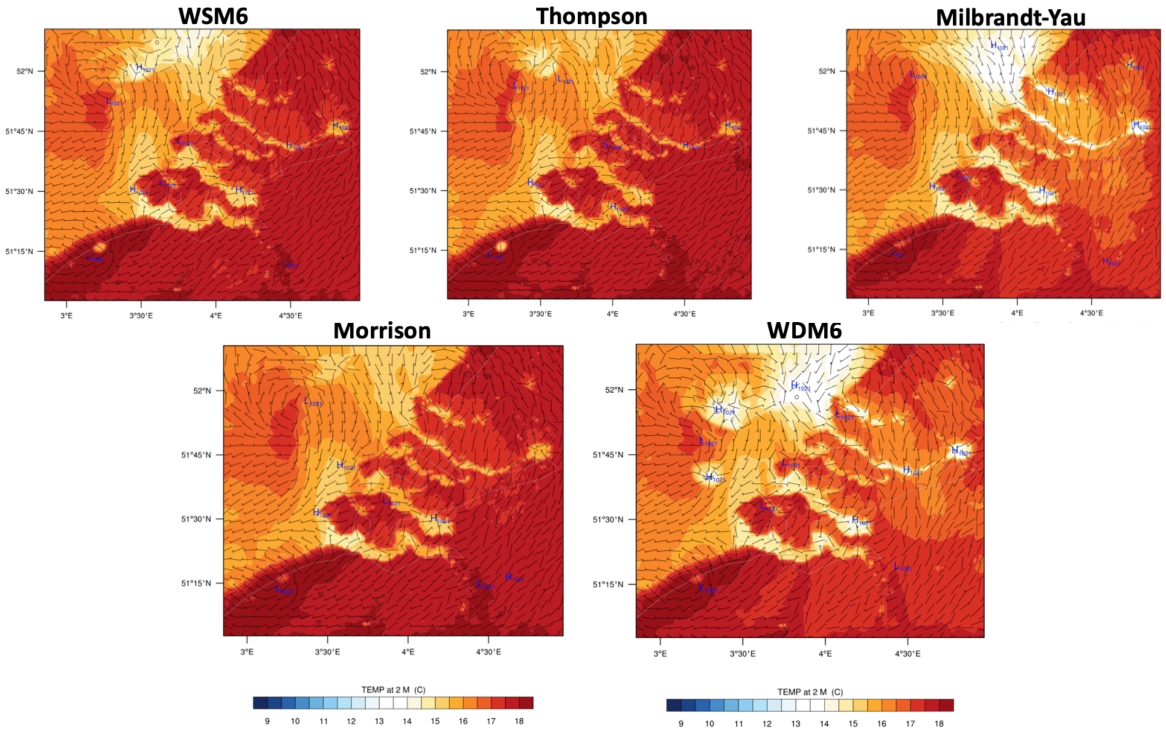

Figure 5.14: Surface temperature (shaded), wind barb and surface pressure centers from 5 schemes at 10:20 UTC

In addition, Figure 5.15 shows the cold pool aloft at the corresponding location of the SST gradient area. The cold pool aloft is a cooler-than-normal pocket of air in the higher levels of the atmosphere, usually about 3km to 6km. It helps the development of clouds and thunderstorms higher up in the atmosphere. When the air parcel passes through the cold pool aloft, the parcel was cooling as it rises, and it is still relatively warmer than the cold pool and can continue going up. Because the air parcel is allowed to rise, it induces more cloud development and thunderstorm potential.

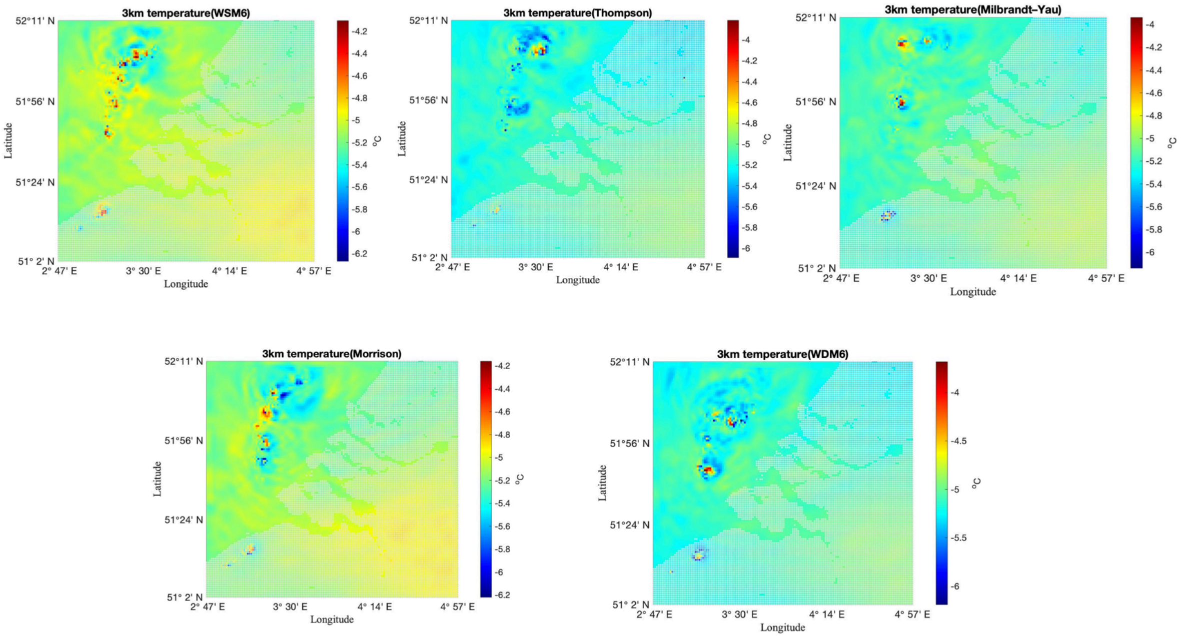

Figure 5.15: 3km temperature from five schemes scheme at 10:20 UTC

To summarise, the areas that are reported waterspouts occurrence show up in the simulations from five microphysics schemes (thermodynamic parameters):

- When the CAPE values are higher than the surrounding regions; however, the CAPE values should not be too large.
- When the LCL and LFC heights are lower than their surroundings.
- When the areas have higher values of two thermodynamic parameters K Index and TT values than the neighbor.
- When the areas show a strong SST gradient at the wind convergence boundary, and the corresponding higher temperature at 3 km show cold pool aloft.

Going along these expectations, the location of waterspouts occurrence shows higher CAPE values than other places. This case shows CAPE values in the interest area belong to a weak instability range (no more than 600 J/kg). The same effect is associated with the occurrence of waterspouts with low LFC height. Low LFC means air parcel gains positive buoyancy at a low level, upward acceleration can start from a low height, and vortex stretching occurs closer to the surface. The whole process is a positive effect, and the same result can be found for LCL height. Based on the research Rasmussen and Blanchard (1998), LCL can be used as an indicator of significant tornadoes related to lower than 800 m. From the results of this study, the LCL heights are satisfied for these two cases.

The KI is a combination of two parts: the vertical temperature lapse rate, and low-level moisture to provide thunderstorm potential. The temperature lapse rate also plays a role in the process of tornadogenesis if it is steep enough. Based on the KI range for waterspouts from previous researches, it is expected to be between 20 and 35. The first case gives its KI values 34 which is in the expected range. Compared with KI, TT shows a condition of lapse rate from higher levels. It can also be seen that a range for TT value, which is 40 to 60. In this case, the TT value is also within the anticipated range. Both KI and TT values for this case are close to the maximum amount of the range.

5.4. Wind shear

The environmental horizontal vorticity is provided by 0–1km Storm Relative Helicity (SRH_{0-1}). According to the research conducted by Thompson et al. (2003), SRH_{0-1}=75 m^2/s^2 can be used as a threshold to distinguish between significant tornadoes and more typical tornado. Furthermore, most cases show that the value larger than the threshold is associated with significantly tornadic supercells, whereas the opposite condition is true for the non-tornadic supercells. Besides, based on the strength of tornado (including waterspout) indicators from SkyStef's weather (Skystef, 2004-2020) that is used in Belgium, when the values of SRH_{0-1} is in the range of 7-46 m^2/s^2 (man value is 27 m^2/s^2), Fujita scale 0 events are possible. Detail of classification is given in Table 5.3. From SRH_{0-1} simulations at 10.20 UTC (Figure 5.16), the area larger than 75 m^2/s^2 area present in the results of WSM6, Thompson, and WDM6 schemes. The most obvious one is the WDM6 scheme (Figure 5.16 (e)) simulated by the largest area with highlighted SRH value. Overall, all simulations indicate the possibility of waterspouts occurrence in the regions of interest.

Table 5.3: Intensity indicators for SRH (Skystef, 2004-2020)

Index	Value	mean	Interpretation
Storm Relative Helicity 0-1 km [m^2/s^2]	7-46	27	Fujita scale 0 (F0) possible
	39-116	80	Fujita scale 1 (F1) possible
	102-241	198	Fujita scale 2 (F2) possible

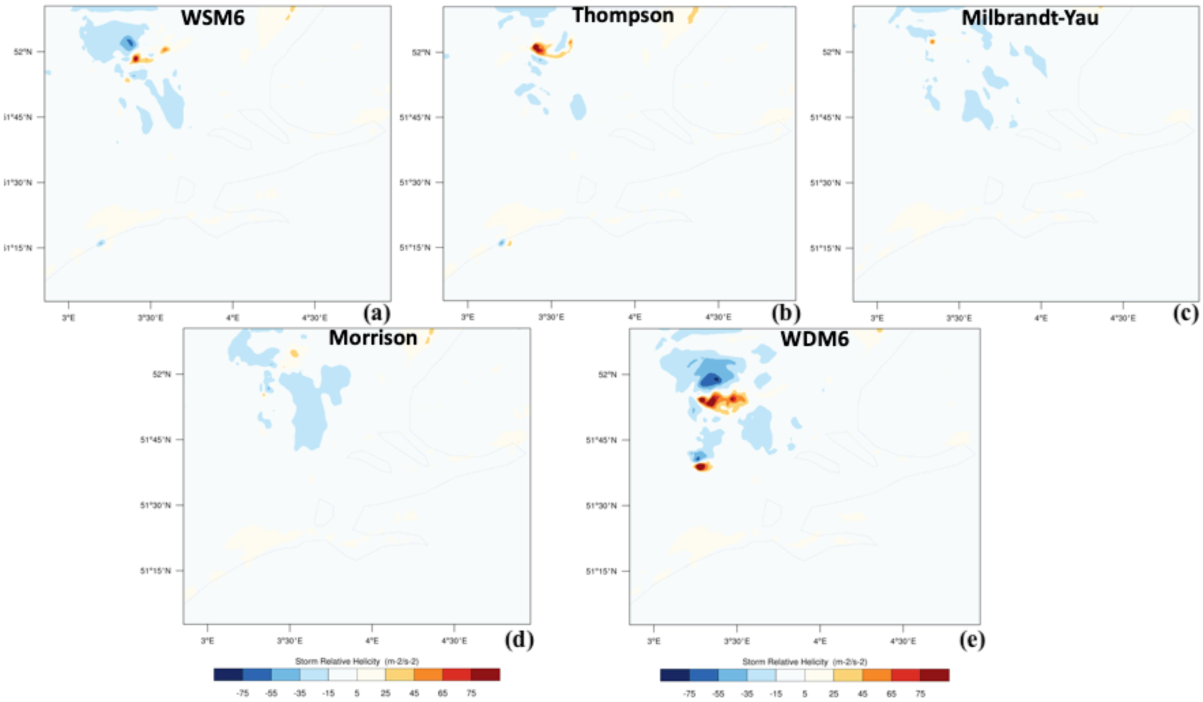

Figure 5.16: 0–1 km Storm Relative Helicity (SRH) at 10.20 UTC by WSM6 (a), Thompson (b), Milbrandt-Yau (c), Morrison (d), WDM6 (e) schemes

Table 5.4 shows the strength indicators for bulk shear from SkyStef's weather used in Belgium. Following Figure 5.17 and Figure 5.18, these two figures demonstrate the 0-1 km vertical wind shear and 0-6 km vertical wind shear, respectively. At this point, it is worth to note that the the simulation from the WDM6 scheme show the most attractive results. It shows a strong and clear vertical wind shear at the region of interest, and it also overlaps with the co-located area of high thermodynamic indices. The highest value of BS01 for the WDM6 scheme is about 18 m/s. This value is in the range of that occurrence of F1 intensity waterspouts is possible. The simulations from the other four schemes show that the magnitude of BS01 is about 10-12 m/s, which is in the range of possibility of F0 waterspouts. In other words, the WDM6 scheme simulated stronger vertical shear than that in the other four schemes. Regarding the BS06, the difference in F0 and F1 strength levels is much less than BS01.

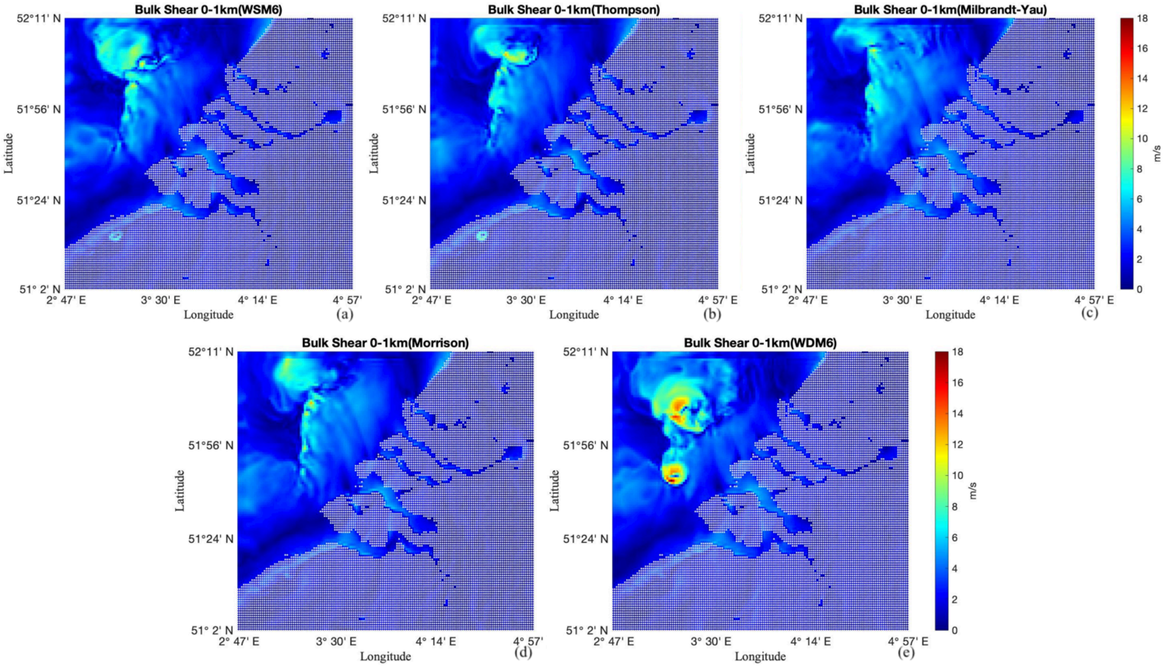

Figure 5.17: 0–1km Bulk Shear (BS01) at 10.20 UTC by WSM6 (a), Thompson (b), Milbrandt-Yau (c), Morrison (d), WDM6 (e) schemes

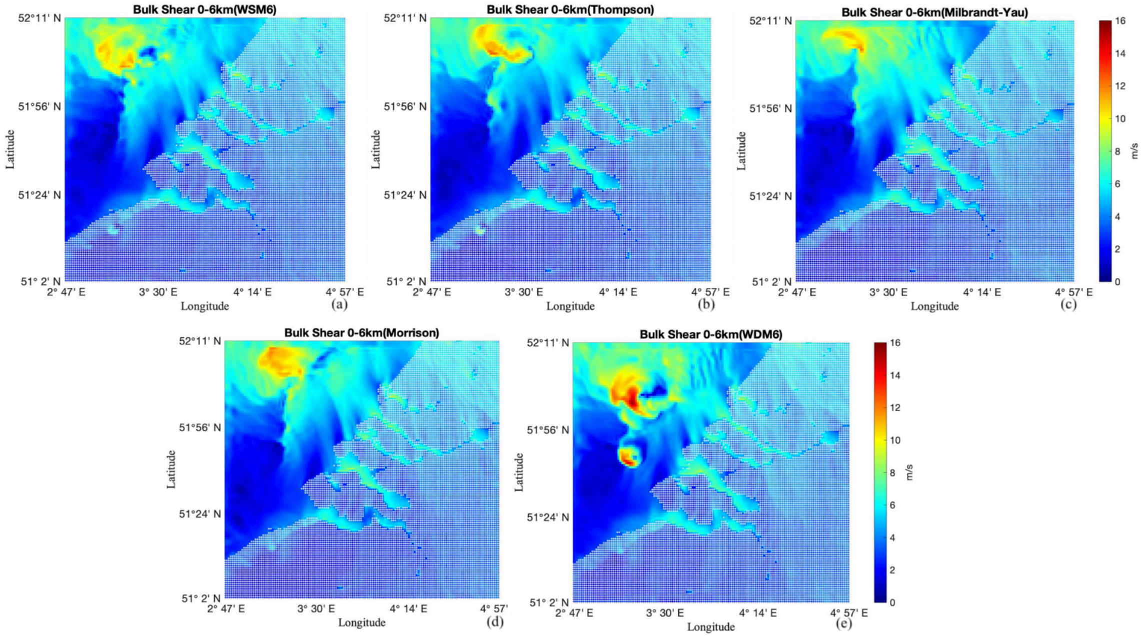

Figure 5.18: 0–6km Bulk Shear(BS06) at 10.20 UTC by WSM6 (a), Thompson (b), Milbrandt-Yau (c), Morrison (d), WDM6 (e) schemes

Table 5.4: Intensity indicators for BS01 and BS06 (Skystef, 2004-2020)

Index	Value	mean	Interpretation
Bulk Shear 0-1km $[m/s]$	5-13	9	Fujita scale 0 (F0) possible
	14-24	17	Fujita scale 1 (F1) possible
	25-43	40	Fujita scale 2 (F2) possible
Bulk Shear 0-6km $[m/s]$	23-38	34	Fujita scale 0 (F0) possible
	19-43	30	Fujita scale 1 (F1) possible
	33-98	52	Fujita scale 2 (F2) possible

The BRN shear term (Equation 2.6) is the denominator of the bulk Richardson number. From the empirical scale of BRN shear, values from 25 to 50 imply the likelihood of tornadic and non-tornadic storms. Values near and above 50 are more likely to be associated with tornadoes. BRN shear is sensitive to low-level winds, and the value of BRN shear is higher for tornadic storms than non-tornadic ones. Lower BRN shear values represent weaker environmental wind shear. In contrast, higher values are generally associated with an increased risk of tornadic supercells. Figure 5.19 depicts the BRN shear from five schemes. The result of the WDM6 scheme shows the largest BRN shear value about 60 m^2/s^2 and two highlight areas about 50 m^2/s^2, which is more likely to be associated with tornadoes at the overlapping location. Besides, the rest four schemes present BRN shear between 10-20 m^2/s^2, which are associated with quite a slight possibility of tornadic and non-tornadic storms.

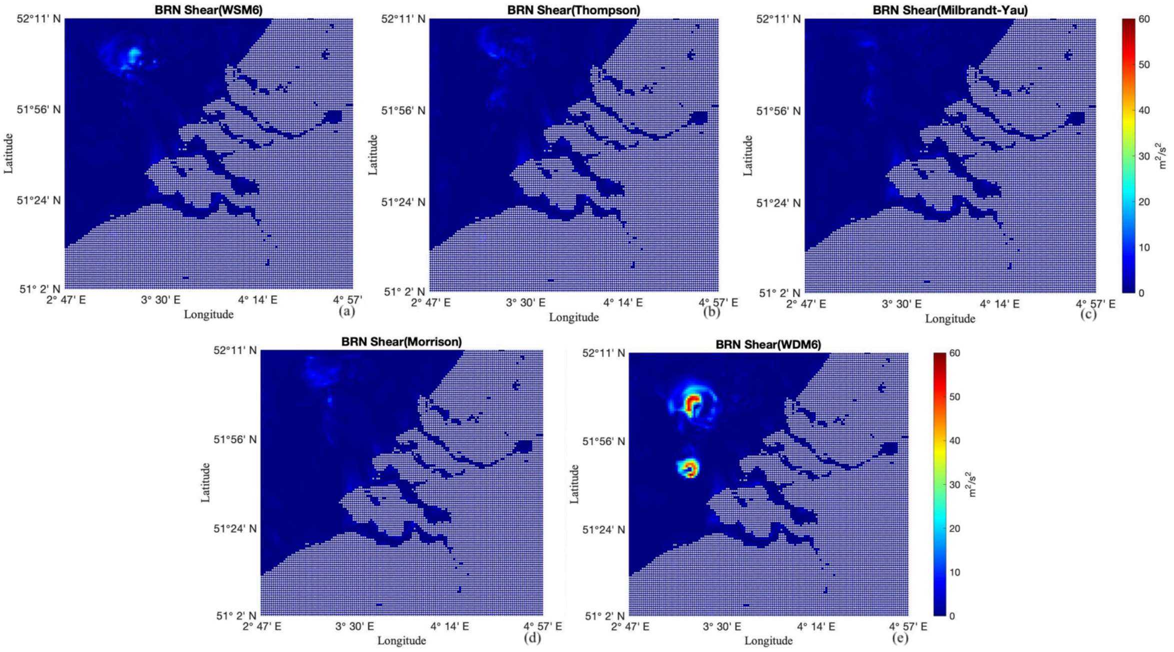

Figure 5.19: BRN shear scheme at 10.20 UTC by WSM6 (a), Thompson (b), Milbrandt-Yau (c), Morrison (d), WDM6 (e) schemes

To summarise, in terms of wind shear, the areas that are reported waterspouts occurrence show up in the simulations from five microphysics schemes:

- When the SRH values are higher than the surrounding regions, and the locations are overlapping with other specific regions as mentioned in Section 5.3.
- When the bulk shear value is higher than surrounding values.
- When the areas have higher values of BRN shear values in comparison with the surrounding areas.

Low-level shear increases strongly with the intensity of the tornadoes (including waterspouts). At the same time, F0 can be easily disguised from F1 and F2, because most of them are strong. That is to say, BS01 is a good indicator to distinguish them. Also, strong low-level wind shear implies that vorticity along a horizontal axis is present, which is an important ingredient of tornado development. However, most of the waterspout events show weak strength, and even a few events are associated with higher intensity. The mean BS01 value of waterspouts is 5.6 m/s and 7 m/s is the line to separate F0 and F1+ (Groenemeijer and Van Delden, 2007). In this study, only the WDM6 scheme simulated BS01 value of about 18 m/s, which is a relatively huge number in this study. On the other hand, the other four schemes show a smaller BS01 value around 7 m/s. Overall, in these five schemes, three of them give BS01 values more than 7 m/s. Besides, between the scale F0 and F1, the 0–6 km shear is much less than the 0–1 km bulk shear. Note that the mean value of BS06 for waterspouts is 12.3 m/s. Results from this case give higher values than the mean value. Despite the weakest result, the BS06 value is approximately 12 m/s.

0–1 km SRH is also used in this study. Rasmussen showed that SRH_{0-1km} is useful to separate tornadic and non-tornadic supercells. SRH shows the environmental horizontal vorticity, and the low-level shear is important, especially for non-mesocyclonic tornadoes. The mean value of SRH_{0-1km} is 7 m^2/s^2, which is easy to match. And the light yellow shaded area shows the. value of SRH_{0-1km} in the range of 0-25 m^2/s^2.

To summary, wind shear is another essential part of waterspouts. In this study, three parameters, bulk shear 0-1km (BS01), bulk shear 0-6 km (BS06) and storm-relative helicity (SRH), are mainly analyzed for the case. In the area of interest, it was found that all of them are higher than their surroundings.

5.5. Updraft and downdraft profiles

The simulated 10 m maximum updraft and downdraft velocities associated waterspouts at 10.20 UTC in the finest domain are shown in Figure 5.20 and Figure 5.21 for the five different microphysics schemes. It is noticeable that the WDM6 scheme clearly shows strong downward wind with speeds about 5 m/s. Three downward centers are shown in Figure 5.21. Next to these highlighted downwards shows strong upward motions, approximately 12 m/s, at the right side of the downward core. On the other hand, the other four schemes simulated similar patterns show a vertical movement line in the interest area. But the strength of these four schemes is quite small compared to the result of the WDM6 scheme. Note that out of the four schemes, and the WSM6 scheme simulated the strongest 10 m maximum upward wind speeds and downward wind speeds than others, with about 12 m/s updraft velocity and 4 m/s downdraft velocity.

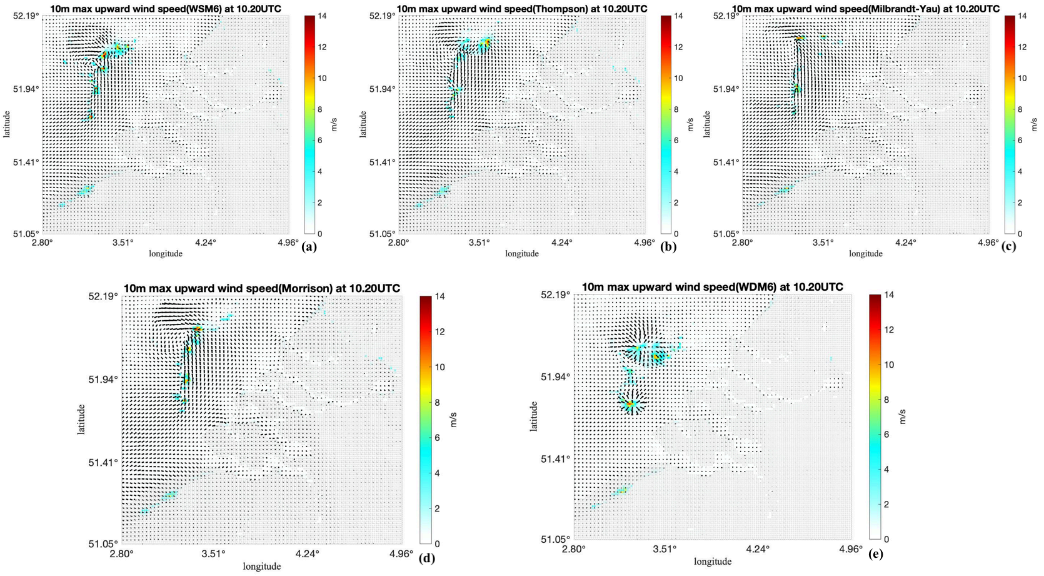

Figure 5.20: 10 m max updraft velocity at 10.20 UTC by WSM6 (a), Thompson (b), Milbrandt-Yau (c), Morrison (d), WDM6 (e) schemes

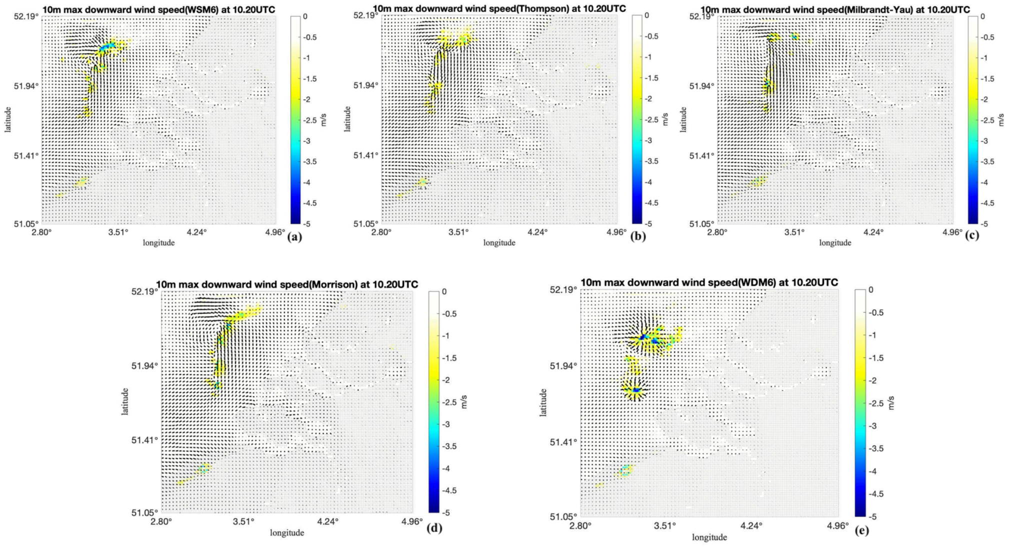

Figure 5.21: 10 m max downdraft velocity at 10.20 UTC by WSM6 (a), Thompson (b), Milbrandt-Yau (c), Morrison (d), WDM6 (e) schemes

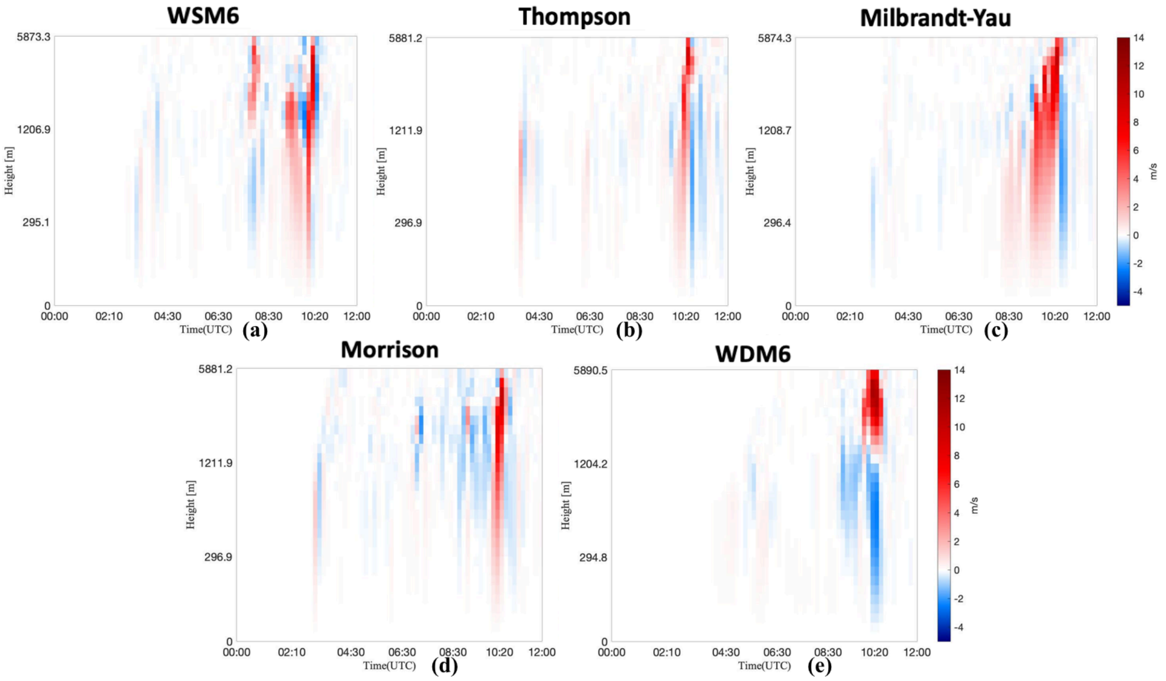

Figure 5.22: Model simulated vertical velocity (upward) at 10.20 UTC by WSM6 (a), Thompson (b), Milbrandt-Yau (c), Morrison (d), WDM6 (e) schemes

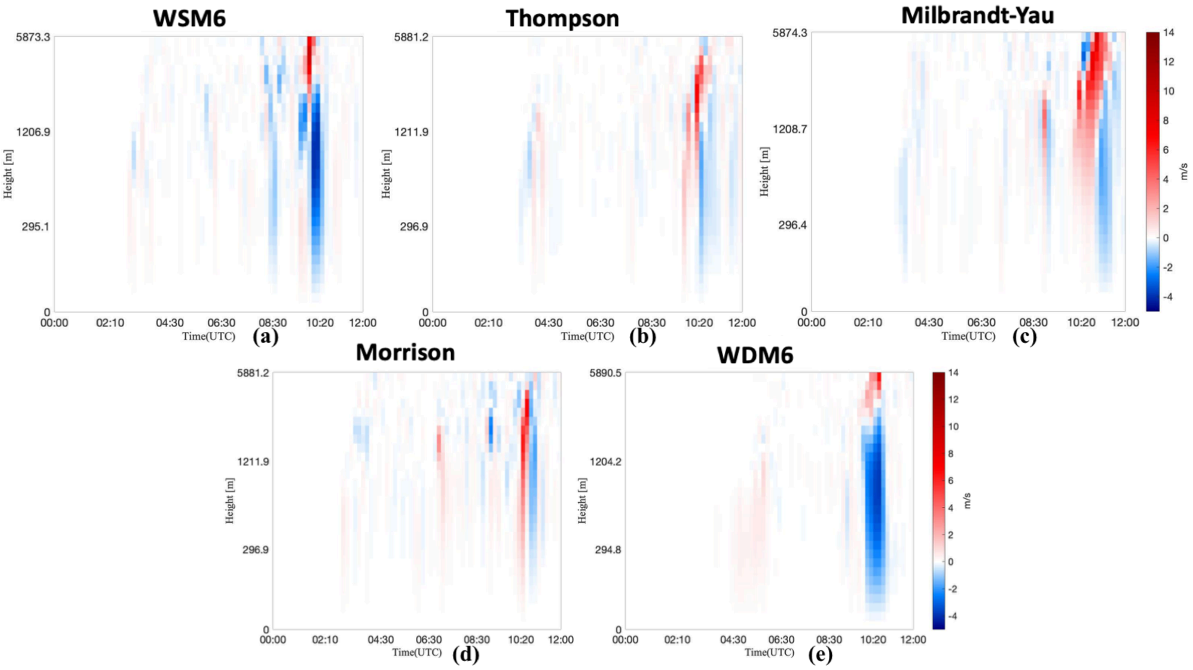

Figure 5.23: Model simulated vertical velocity (downward) at 10.20 UTC by WSM6 (a), Thompson (b), Milbrandt-Yau (c), Morrison (d), WDM6 (e) schemes

Figure 5.22 and Figure 5.23 show the time series of the strongest points of vertical movement from 10 m maximum upward to downward wind speeds. Besides, Figure 5.22 shows five points that present the strongest upward motion in Figure 5.20. Overall, all schemes simulate an updraft core with the associated downdrafts, but their strength and duration are different. First, the WDM6 scheme gives the most different structure in time series plots compared with others. In the WDM6 scheme, the updraft core (about 12-14 m/s) is approximately 4000 m above the downdraft core (about 3 m/s) approximate 1000 m around 10.20 UTC. Moreover, Thompson and Milbrandt-Yau schemes give similar updraft variation with time. A relatively strong upward came firstly followed by weak downward around the same time with WDM6's. Consequently, the Thompson scheme's simulation shows the shortest duration and weakest strength of updraft approximate 6 m/s. Besides, WSM6 and Morrison schemes simulated a short duration strong updraft (more than 10 m/s) around ten o'clock, and this strong updraft is surrounded by weak downdraft before and after this time. For the downward simulation (Figure 5.23), WSM6 and WDM6 scheme simulates a stronger downdraft, which is stronger than the other three schemes, whose speeds are in the range of 4-5 m/s.

Additionally, simulation of WSM6 and WDM6 schemes show a longer lifetime of the downdraft and give larger downdraft velocities. The remaining three schemes show a relatively weak downward vertical speed of about 2 m/s, after an upward-moving about 6 m/s. Morrison and Thompson schemes modeled similar movements. However, the simulation with Morrison scheme gives the vertical speeds both upward and downward movement. Both movements start from the near-surface up to approximately four kilometers, which is higher than the downdraft for the Thompson scheme.

5.6. Surface winds

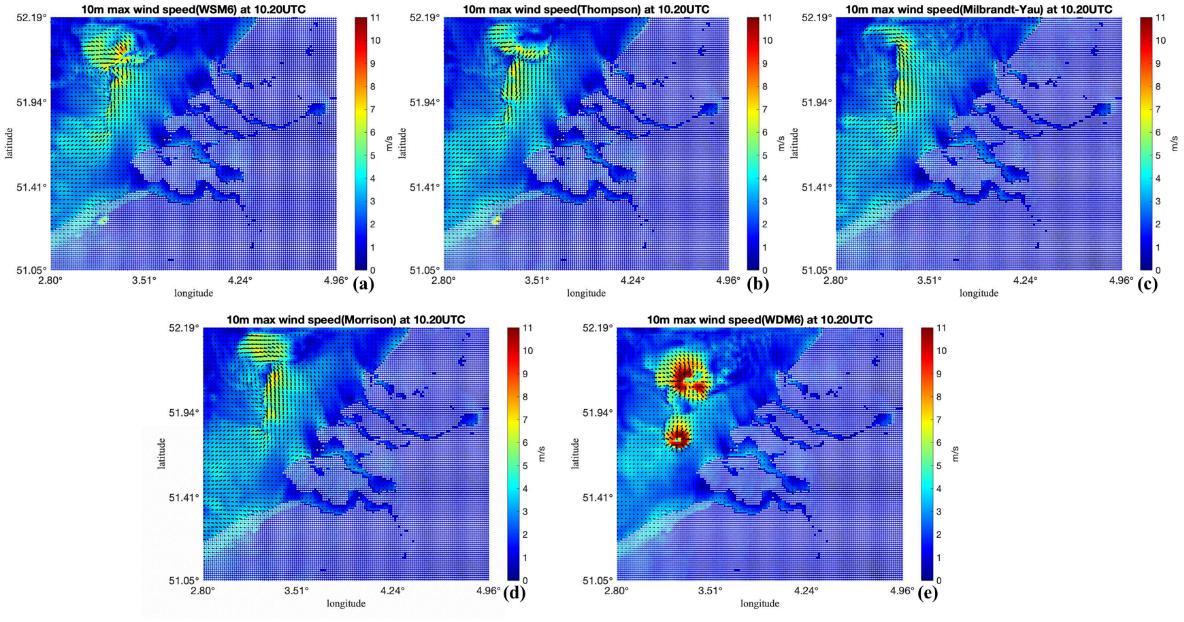

Figure 5.24: (a)10 m maximum wind speed at 10.20 UTC by WSM6 (a), Thompson (b), Milbrandt-Yau (c), Morrison (d), WDM6 (e) schemes

The model-derived 10m max wind field, in the innermost domain (d03) at 10.20 UTC of September 1, 2017, were analyzed for the WSM6, Thompson, Milbrandt-Yau, Morrison double moment and WDM6 schemes (Figure 5.24). It was noteworthy that Figure 5.24 (e) shows two clear divergences at 10m, and the highest wind speed reaches to 11 m/s. The areas are overlapped with the noted values of the aforementioned parameters. The rest of the schemes do not show this strength of wind speed and this kind of clear divergence. The WSM6 (Figure 5.24 (a)) and Thompson scheme (Figure 5.24 (b)) simulated results also provide weaker divergence pattern, and their highest speed reach approximately 7-8 m/s. In contrast to Milbrandt-Yau and Morrison double moment scheme's simulation (Figure 5.24 (c) (d)), a line shape wind speed is shown in the figures. In other words, at a specific location, a speed difference boundary appears, on the left-hand side of the line, wind speed under 4 m/s, whereas on the other side, wind speed is higher than 7 m/s. Moreover, a similar boundary pattern also shows in the WSM6 and Thompson scheme based simulation, which is located at the south of their weak divergence. Besides, on the land near the coast of Belgium, an obvious wind speed which is higher than that in its surrounding area can be noticed in simulations with WSM6 and Thompson schemes.

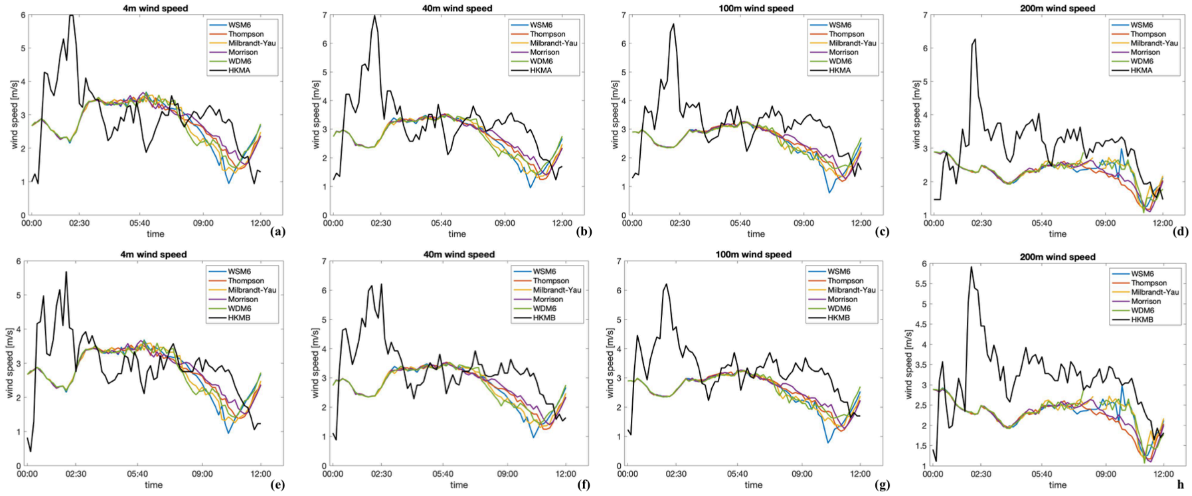

Figure 5.25: Top panel: Lidar observed and simulated wind speed time series from 4 m (a), 40 m (b), 100 m (c) and 200 m (d) height measured at location HKZA on September 1, 2017; bottom panel: Lidar observed and simulated wind speed time series from 4 m (e), 40 m (f), 100 m (g) and 200 m (h) height measured at location HKZB on September 1, 2017

Near the region of interest, the lidar measured wind speed data at two very close locations HKZA and HKZB are available for September 1, 2017. Figure 5.25 shows the observed wind speed compared with a simulation at the same point from 00 UTC to 12 UTC. During this period, a wind speed peak occurred at around 02.30 UTC; however, all modeled wind time series show a valley-like shape, causing the speed difference quite big 4-5 m/s. After this time, modeled wind speeds are slightly overestimated most of the time during nighttime below 100 m. In contrast, wind speeds during the daytime are underestimated by the simulations. At 200 m, irrespective of the time, all simulations underestimate the wind speeds. As for the simulated wind speed time series, outputs from all schemes show a similar tendency. For daytime and regions with lower height like (a),(b),(c),(e),(f),(g), Morrison scheme based simulated is slightly closer to the observation than the other simulations. It was found that with the increase, the rest of the schemes simulated better wind speed results.

Next, a single grid point from each simulation is selected for further analysis. Time series of 10m max wind, surface pressure, surface temperature, and total accumulated precipitation from this point are plotted in Figure 5.26. Thompson, Morrison, and WDM6 schemes simulated a clear wind speed peak between 10 UTC and 12 UTC; especially, the peak from the WDM6-based run is very prominent. Moreover, at the corresponding time, the surface pressure decreases. Besides, two of the three simulations show that their temperature decrease when it starts to rain at this particular time. The only temperature from the Thompson scheme increases when there is no rain at this moment. As for simulations from WSM6 and Milbrandt-Yau schemes illustrate sudden fluctuation between 10 UTC and 12 UTC, the corresponding time series of surface pressure also decreases more or less. Also, the temperature drops for the WSM6 scheme during rain. At the same time, the Milbrandt-Yau scheme predicts no rain and increasing temperature.

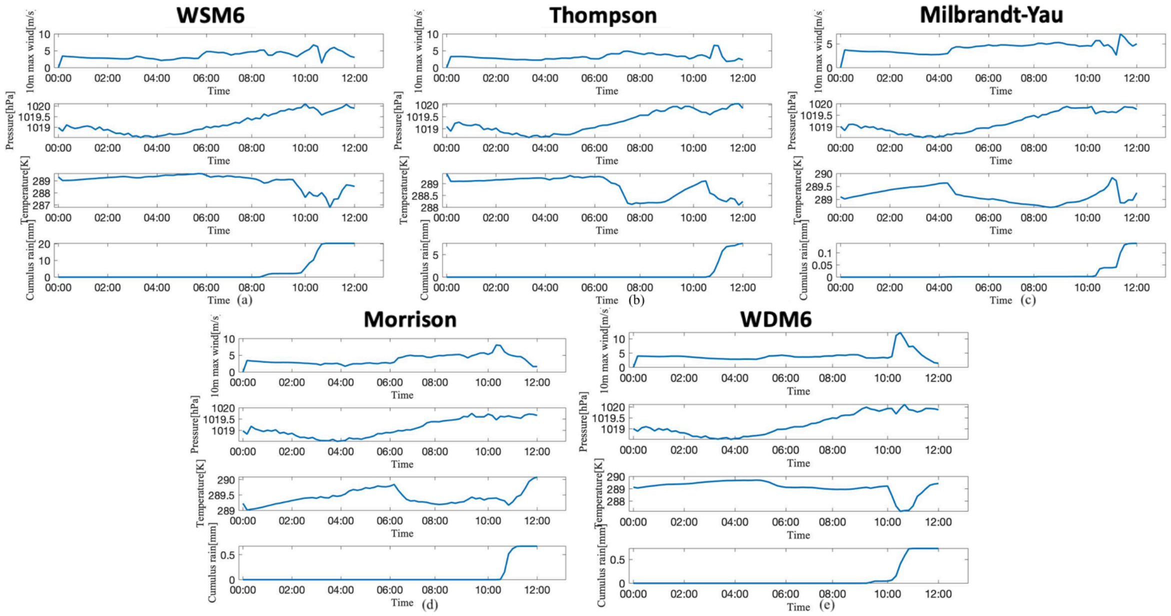

Figure 5.26: Time series of 10m max wind, surface pressure, surface temperature and total accumulated precipitation by WSM6 (a), by New Thompson scheme (b), by Milbrandt-Yau scheme at (c), by Morrison scheme (d), by WDM6 scheme (e)

5.7. The Szilagyi Waterspout Nomogram

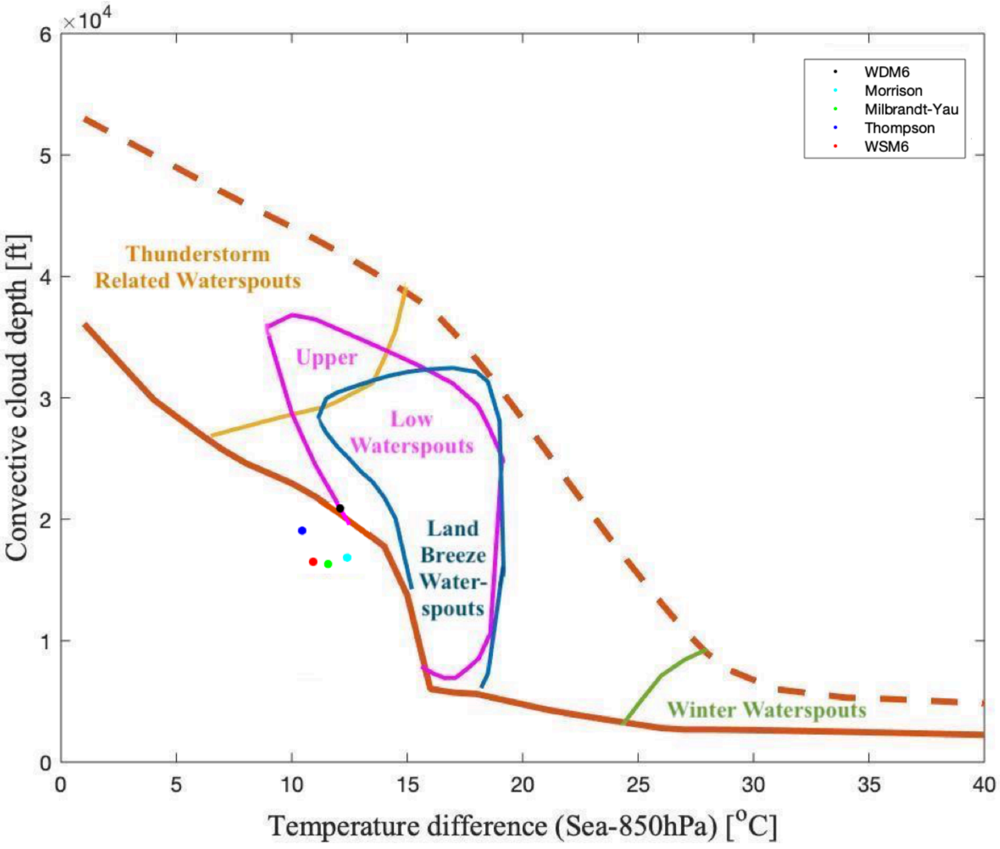

Figure 5.27: The Szilagyi Waterspout Nomogram

The Szilagyi Waterspout Nomogram is an empirical technique based on waterspout events over the Great Lakes. Three most relevant correlators are selected from fourteen parameters. These parameters are temperature difference (ΔT) between the water surface and 850 hPa level, convective cloud depth (ΔZ), and an additional criterion for wind speed at 850 hPa (no more than 40 kts or 20.58 m/s). Besides, by using different color threshold lines representing different types of waterspouts, the nomogram is also divided into some waterspout classification. In this case study, the convective cloud depth of case1 is approximately from 16000 ft to 21000 ft, and the height is matched with the vertical movement profile. Subsequently, Figure 5.22 and Figure 5.23 show the heights of vertical motion about from 5000 to 6000 m, which is equal to the convective cloud depth. The temperature difference of this case is between 11-12 °C. Hence, Figure 5.27 depicts the values of this case in the Szilagyi nomogram. Each point represents one microphysics scheme. Interestingly, only one point from the WDM6 scheme is in the range. This scheme always simulated the strongest condition for all parameters mentioned above.

6

Results of Case Study II

This chapter is quite similar to the previous chapter, aiming to provide the simulated results for the second case study. Basically, the chapter shows simulations by comparing these results with observations, by analyzing the thermodynamic environment, and by characterizing the wind conditions to answer the research questions. Section 6.1 gives the synoptic conditions. Next, to demonstrate the difference between simulations and reality, radar reflectivity was used as a reference in Section 6.2. Section 6.3 elaborates on the thermodynamic environment of case II, including some comparisons between radiosounding observations and corresponding simulations. Besides, some thermodynamic parameters are discussed. The following three sections (Section 6.4, Section 6.5, and Section 6.6) characterize wind conditions by wind shear, vertical movement, and surface wind patterns, respectively. Finally, Section 6.7 shows the Szilagyi Waterspout Nomogram test result for this case.

The second case is recorded by ESWD as well. Compared to the first case, it occurred in a different background environment. Only one waterspout was observed at 05.40 UTC±15 minutes on August 31, 2018 (Figure 6.1). Daily weather summary from Met office also has documentation of that day: there were a few showers in southeast England, with reports of a funnel cloud of the Kent coast. Figure 6.2 is the photo of case II from two witnesses. We can see from this photo that a waterspout crossed through a wind farm. Moreover, the relatively heavy rain, which is located on the left-hand side of the waterspout, is shown in Figure 6.2. According to the distribution of wind farms (Figure 6.4) and the report area from ESWD in Figure 6.1, it is most likely that the waterspout passed through either Kentish Flats Extension or Thanet Extension wind farms. Based on the historical records from LightMaps.org (Figure 6.3), there were no lightning strokes at the interest area at all between 00 UTC to 12 UTC on August 31, 2018. Thus, this case was associated with a fair-weather type waterspout.

Figure 6.1: Waterspout events from ESWD, August 31, 2018. Red inverted triangle indicates the location of a tornado event

Figure 6.2: Waterspouts photographs from Herne Bay by Chris Attenborough and Jayne Smith, August 31, 2018

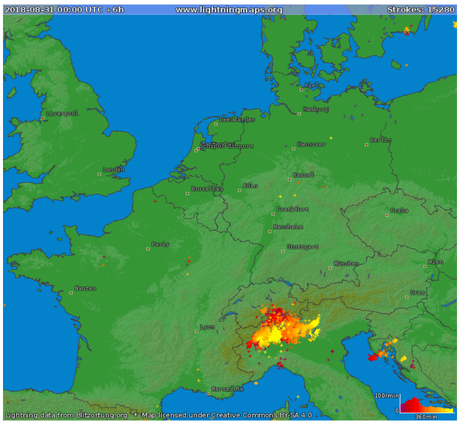

Figure 6.3: Archive Lightning Maps, August 31, 2018 (Blitzortung.org Contributors, 2003-2020)

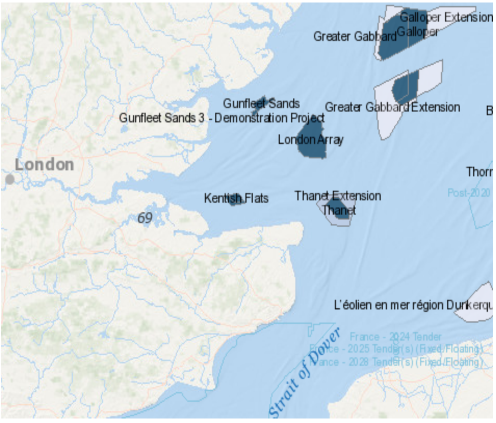

Figure 6.4: Wind farm location near waterspout location (4C Offshore, 2019)

6.1. Synoptic analysis

The 500 hPa analysis charts (Figure 6.5 (a),(b),(c)) indicates that a long-wave pressure trough is just above the area of interest at 06 UTC. Therefore, the synoptic chart of this case is a long-wave trough (LW). The trough became deeper between time 00 UTC and 06 UTC; however, it was blocked from 06 UTC to 12 UTC. During this period, this trough moves from west to east. These isobars are showing the direction of the upper-level wind movement, which was turning over the location of interest. Besides, Figure 6.5 (d), (e) show the synoptic condition at surface. A noticeable low-pressure center was located in the northwest of the interest area, and the low-pressure moved to the east. The waterspout occurred at the outer edge of a high-pressure center, moving to the southwest side. In general, the high-pressure area always associates with good weather. Hence, further evidence of this waterspout is a fair-weather type waterspout. Moreover, an upper occluded front and a trough were present not far from the region of interest.

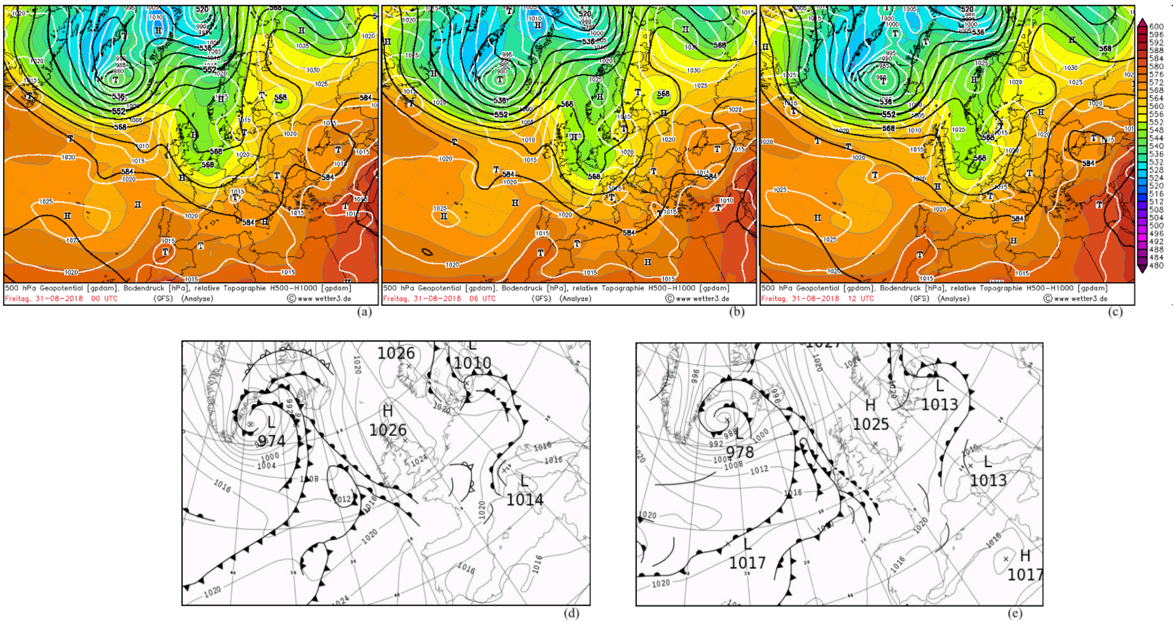

Figure 6.5: Forecast System (GFS) analysis at 00 UTC (a), 06 UTC (b), 12 UTC (c) showing geopotential height [gpdm] at 500 hPa (thick bold lines) (R. Behrendt H.Mahlke, Since 2003); Surface synoptic chart at 00 UTC (d) and 12 UTC (e) (The Met Office, 2020)

6.2. Radar reflectivity with different microphysics schemes

Figure 6.7 shows the spatial distribution of simulated maximum reflectivity on August 31, 2018, at 05.40 UTC in domain 2 and 3. To make a comparison, observed radar images (Figure 6.6 (a)-(e)) from Buienradar website (RTL Nederland, 2020) are used. Figure 6.6 (a)-(e) show radar precipitation around documented waterspout time for five times. At this point, one thing that needs to be mentioned is that because this website did service for the Netherlands, the time is in Central European Summer Time (CEST), two hours ahead of Coordinated Universal Time (UTC). Those images of rain radar are utilized because they captured more detail for the area interest. Moreover, by using the Marshall-Palmer Equation 6.1, radar reflectivity (L_z) can be converted to rainfall rates (R) in millimeters per hour. As a result, to compare the modeled reflectivity with the radar images, one can follow the reference range shown in Table 6.1.

$$R = \left(\frac{10^{L_z/10}}{200}\right)^{\frac{5}{8}} \tag{6.1}$$

Reflectivity in dBZ versus Rainrate in mm/h		
L_z(dBZ)	R(mm/h)	Intensity
10	0.15	Light mist
20	0.6	Very light
30	2.7	Light to moderate
40	11.53	Moderate rain
45	23.7	Moderate to heavy
50	48.6	Heavy
60	205	Extreme/moderate hail
65	421	Extreme/large hail

Table 6.1: Radar reflectivity (L_z) converted to rainfall rates (R) (Bateaux, 2016)

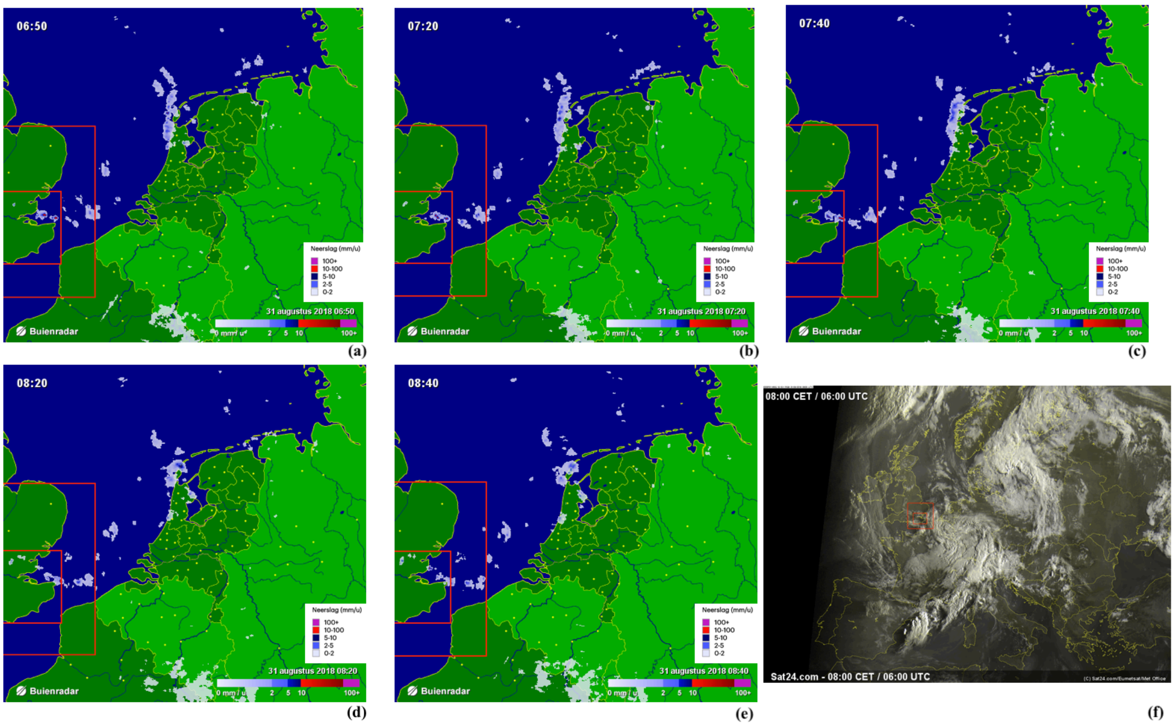

Figure 6.6: Precipitation [unit: mm/h] from 06:50 CEST (a), 07:20 CEST (b), 07:40 CEST (c), 08:20 CEST (d), 08:40 CEST (e), and satellite image at 06:00 UTC on September 1, 2017 (RTL Nederland, 2020; The Meteo Company B.V., 2006-2020)

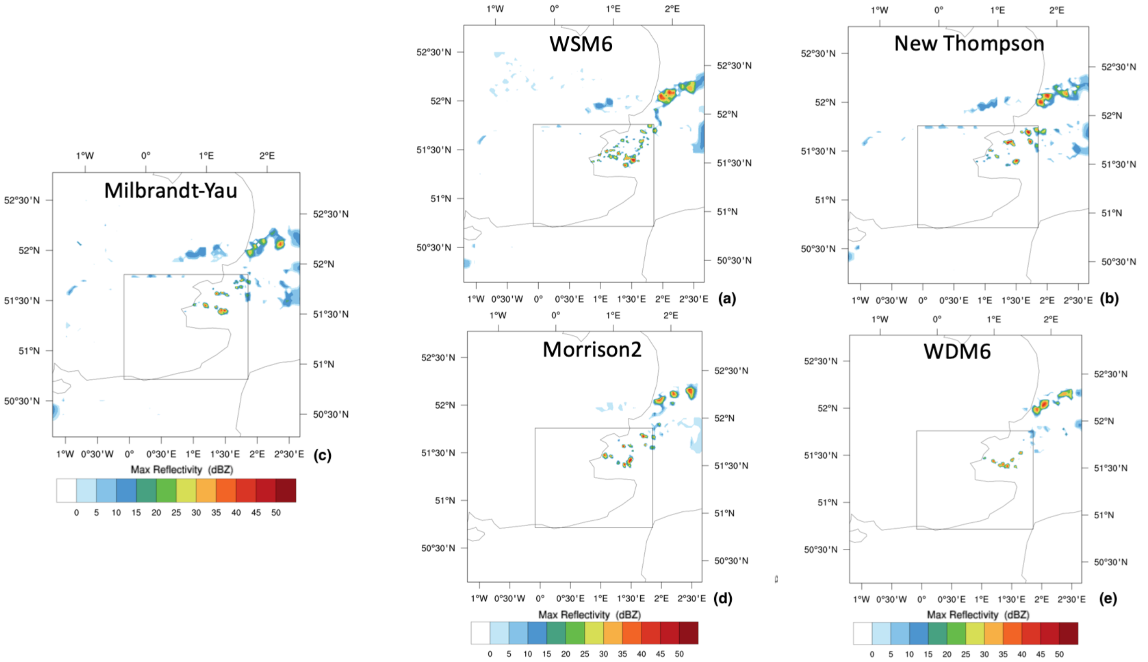

Figure 6.7: Max reflectivity [unit: dBZ] 05:40 UTC for domain 2 and domain 3 of five microphysics schemes: WSM6 (a), Thompson (b), Milbrandt-Yau (c), Morrison-double (d), WDM6 (e)

Firstly, for satellite image (The Meteo Company B.V., 2006-2020), Figure 6.6 (f) shows a clear occluded front and a comma cloud at 06 UTC on August 31, 2018. The study area is located on the edge of the occluded front. In terms of the radar images that present the rain areas at 07:40 CEST (which is

05:40 UTC) and show that the rain areas are further south than the modelled results, the simulations seem more like the observation at 06:50 CEST in the finest domain. If taking this time's image as a reference, the precipitation rate between 10 mm/h and 100 mm/h is equal to reflectivity larger than 40 based on Table 6.1. Furthermore, taking location and strength into account, the Morrison double and Milbrandt-Yau scheme give results that are the closest to reality. Besides, the modelled reflectivity from the WDM6 scheme is quite similar to the radar image at 07:20 CEST, which is 05:20 UTC.

In the finest domain, all schemes were given several individual thunderstorm activity spots. At the same time, all schemes show clusters of 2-3 single cells moving together as a multicell thunderstorm. As for their strength of reflectivity, the Milbrandt-Yau and WDM6 scheme are clearly weaker (about 40-45 dBZ) than the other three schemes. Overall, it was found that the WSM6 scheme simulated the most numerous cells in the innermost domain, and the outer domains show a similar thunderstorm activity location towards the northeast of the inner domain boundary.

6.3. Thermodynamic environment

6.3.1. Sounding

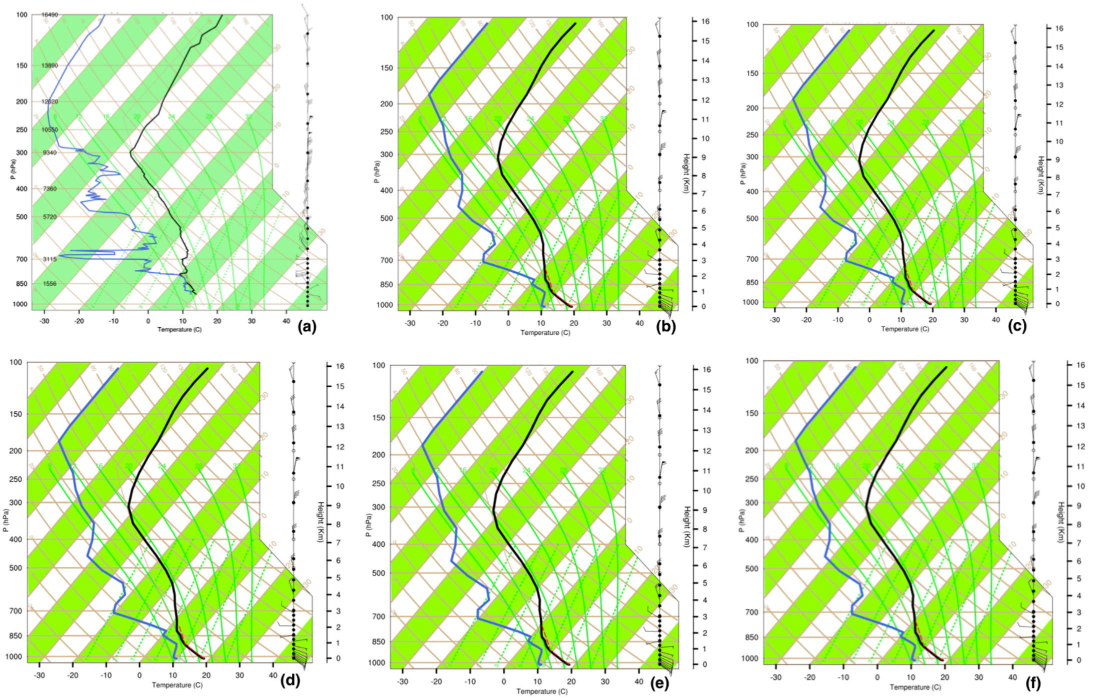

Figure 6.8: (a)Skew-T log-p diagram of radiosounding at Herstmonceux station on August 31, 2018 at 12 UTC (The University of Wyoming, 2020), Skew-T log-p diagram of simulation result by WSM6 scheme (b), Thompson (c), Milbrandt-Yau (d), Morrison (e), WDM6 (f)

In order to assess the results of the simulations, one atmospheric sounding station called Herstmonceux ($50.90^{o}N, 0.32^{o}E$) is selected. Figure 6.8 shows the Skew-T log-p diagram, including a comparison between radiosounding and simulation at the stations on August 31, 2018, at 12 UTC. First of all, simulations of the wind speed and direction perform quite well, and all schemes show similar wind variations. Subsequently, regarding the thermodynamic side, the simulation shows that the trend is more or less the same with each other. At the same time, the simulations are found to be similar as the general tendency of observation. However, there are two obvious differences between observation and simulation. The first difference appears at 700 hPa level, which is a super dry layer in observation with a dew point temperature of -40 °C. In comparison, the model gave the level's dew point just about -20 °C. Another difference is found at the lower level, from 850 hPa to some height between 850 hPa and 700 hPa. Measured results show saturation at this range. Besides, another really low level, between 850 hPa and surface, shows that the environment is close to saturation. However, the model for all schemes did not simulate the two very moist layers; instead, only two moderately moist levels were simulated.

According to Table 6.2, the values of CAPE from the model are quite close to each other, except the Milbrandt-Yau scheme, which gives a slightly lower value of 41 J/kg. Nonetheless, the observation by the Herstmonceux station's data shows that the CAPE value is 26 J/kg as half of the largest modeled value 52 J/kg from Morrison and WDM6 schemes. For the rest of the parameters, the model gives slightly higher values for both LCL and EL level compared with the sounding values. Overall, simulations are quite close to reality, except the CAPE values.

Table 6.2: Thermodynamic parameters of August 31, 2018 based on observed and sounding soundings data of Herstmonceux station

Parameter	Sounding	WSM6	Thompson	Milbrandt-Yau	Morrison-2	WDM6
EL (hPa)	789.21	772.91	785.02	774.63	771.67	771.36
EL_T (°C)	2.31	1.44	2.13	1.54	1.35	1.4
LCL (hPa)	903.21	896.65	895.19	896.53	895.52	896.44
LCL_T (°C)	8.43	7.95	7.90	8.00	7.92	8.03
ΔT (°C)	13.40	13.05	13.10	13.09	13.13	13.18
CAPE (J/kg)	26	48	46	41	52	52

6.3.2. Simulation of thermodynamic indies

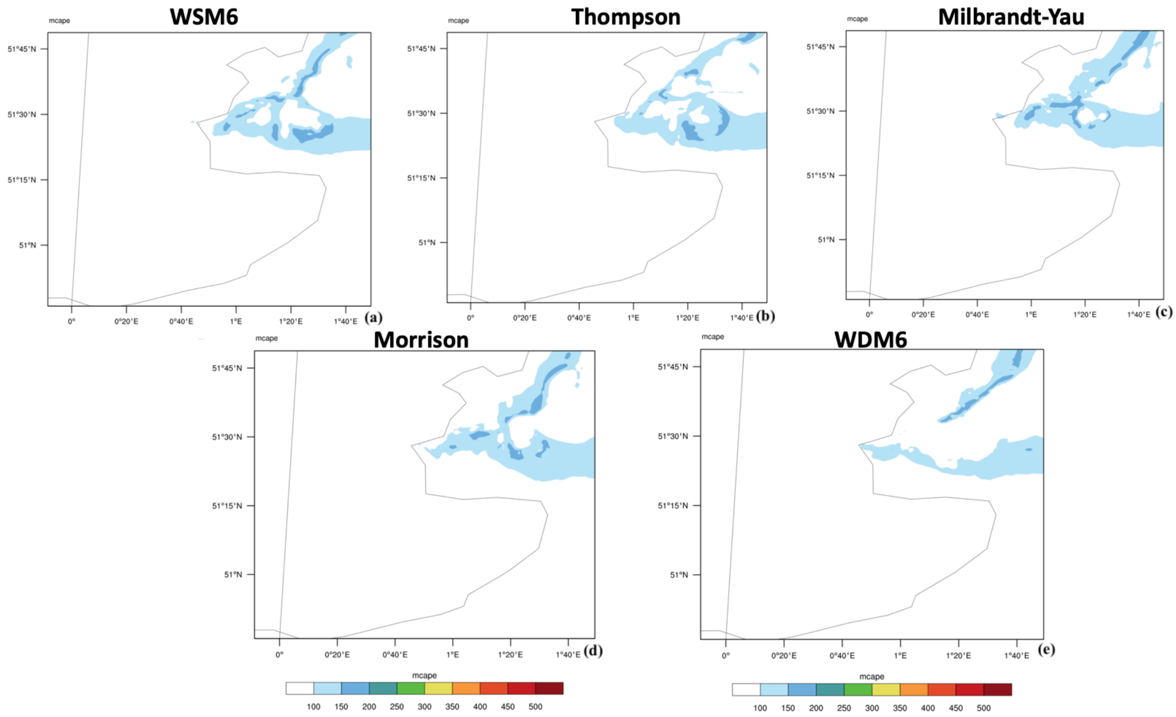

Figure 6.9: Maximum convective available potential energy (MCAPE) at 05.40 UTC by WSM6 scheme (a), Thompson (b), Milbrandt-Yau (c), Morrison (d), WDM6 (e)

The maximum convective available potential energy (MCAPE) values in the finest domain are presented in Figure 6.9 at 05.40 UTC. According to Figure 6.9, all of the distribution of simulated MCAPE are less than 200 J/kg, which belongs to a weak instability range at this moment. This marginally unstable environment is matched with the situation of fair-weather waterspouts occurrence. Moreover, except for the WDM6 scheme simulation, the other four schemes show almost the same shape in the unstable areas. The approximate location of waterspout occurrence is included in the region with the high CAPE values.

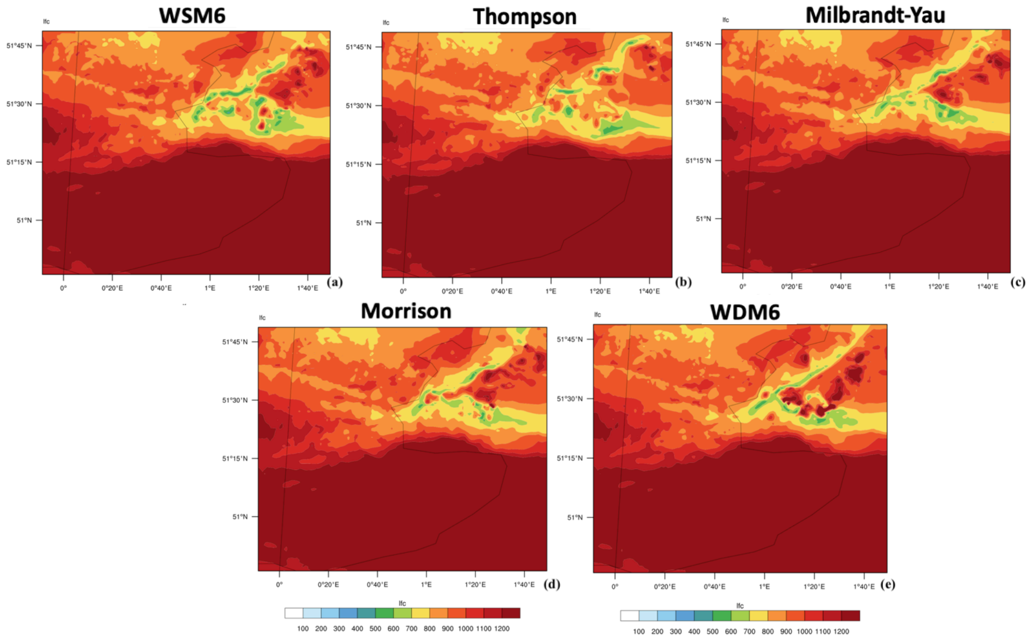

Figure 6.10: Level of free convection (LFC) at 05.40 UTC by WSM6 scheme (a), New Thompson (b), Milbrandt-Yau (c), Morrison (d), WDM6 (e)

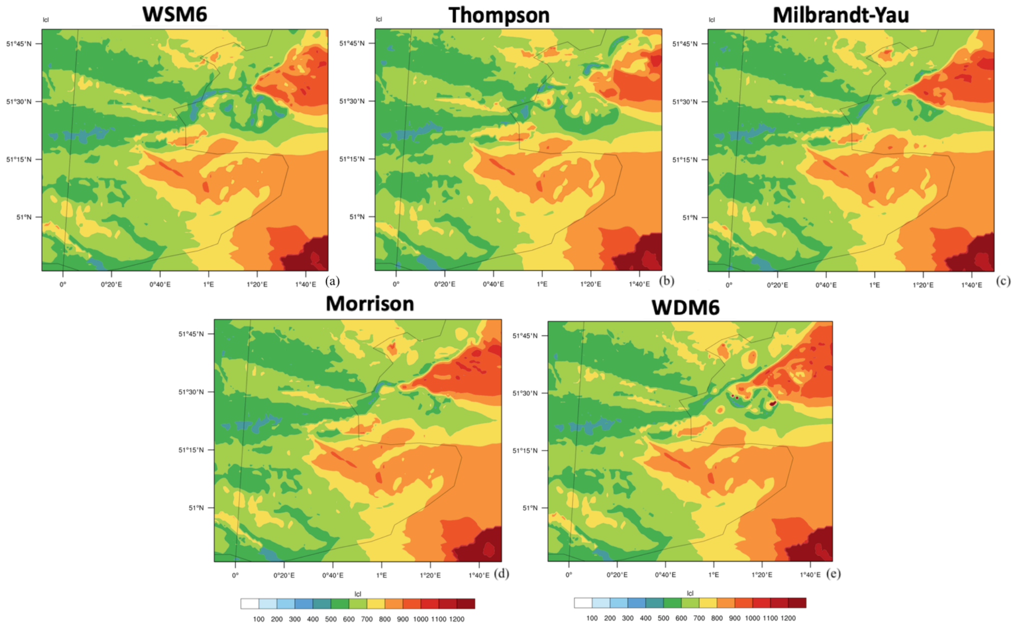

Figure 6.11: Lifting Condensation Level (LCL) at 05.40 UTC by WSM6 scheme (a), Thompson (b), Milbrandt-Yau (c), Morrison (d), WDM6 (e)

There is a strong relation between tornadoes and low level of free convection (LFC). This relation was found by Davies in 2004. Low LFC height provides a lower starting level of upward acceleration. That means vortex stretching, which is a important ingredient of waterspouts, can develop at near surface layer. Besides, a low LFC height implies a low LCL level, but a low LCL does not necessarily lead to a low LFC. In fact, it is also true that low LCL heights are associated closely with tornadic storms (Thompson et al., 2003; Craven et al., 2004). The LCL and LFC heights are modeled by five schemes on August 31, 2018 at 05:40UTC (Figure 6.11, Figure 6.10).

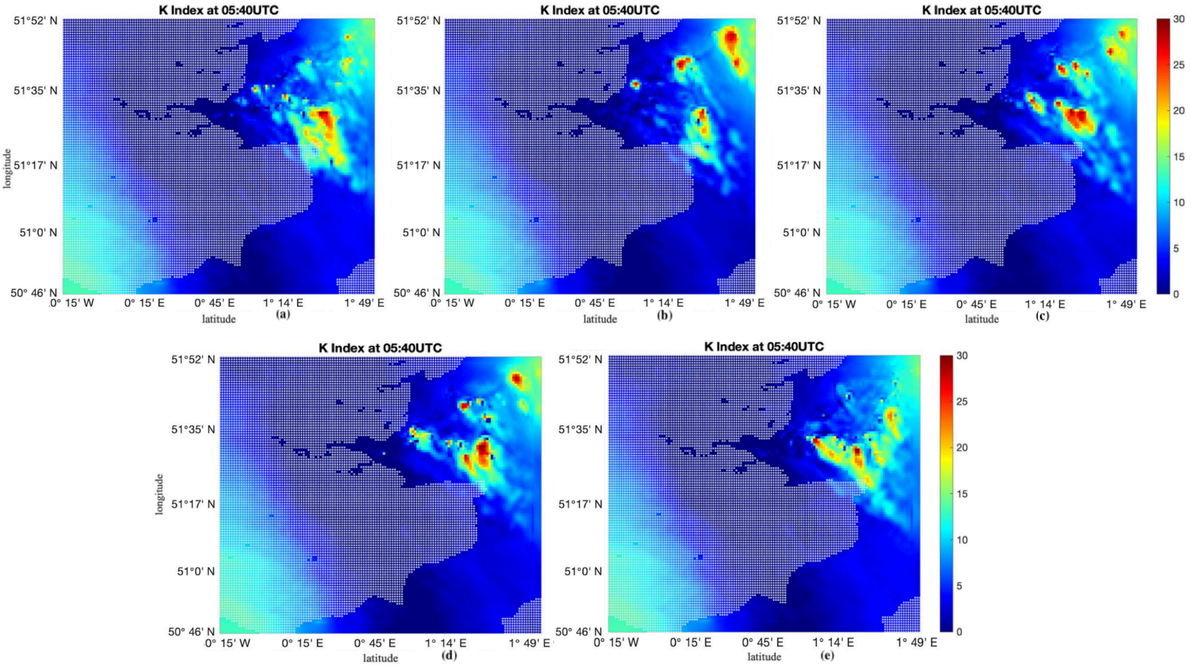

Figure 6.12: K Index at 05:40 UTC by WSM6 scheme (a), Thompson (b), Milbrandt-Yau (c), Morrison (d), WDM6 (e)

Figure 6.10 clearly show the low LFC areas overlapped with high CAPE values regions. Moreover, the highest CAPE areas also present the lowest LFC (in the range of 500-600 m). The simulation from the WDM6 scheme shows the strongest LFC height at the co-located area. And the lowest LFC area (500-600 m) is next to the highest LFC area (over 1200 m). As for plots of LCL height, the waterspout location is also the region that both Kentish Flats and Thanet Extension wind farms located in present relative low LCL height, which is below 600 m. WSM6 and WDM6 schemes show that the lowest LCL height at the area of interest is 400-500 m, and the WDM6's result gives more than 1200 m LCL areas which are the neighbor of the lowest area. The heights are contained in the range of statistical results, which is the most destructive tornadoes form when LCL heights are extremely low in the 400-600 m range.

In Figure 6.12, the simulations of KI show that the areas of high KI value are corresponding to reported waterspout location. Especially for Milbrandt-Yau, Morrison double, and WDM6 schemes, their simulation is closer to the wind farm location. The areas with high values from the rest two schemes are more easterly than expected. As mentioned before, KI values are empirically divided into three threshold ranges, which are related to severe weather likelihood: the first range is the KI value smaller than 30; the second one is a value between 30 and 40. The third range is the value higher than 40. In brief, as the index value increase, the likelihood of thunderstorms will become higher. Furthermore, in Figure 6.12, the highest KI values from all schemes present to be more or less 30, which is the junction of the first and the second range of KI empirical threshold.

The high TT Index value distributes relatively widely. Concerning the empirical three threshold ranges of TT value mentioned before: the first range is 45-50, which represents thunderstorms possible; the second one is thunderstorms more likely to occur in possibly severe values range (50-55); when TT index is larger than 55, severe thunderstorms are most likely to happen. Figure 6.13 shows the TT index from five microphysics schemes in the innermost domain at 05:40 UTC. All of them include some grids TT index near 49, which belongs to the first range. This is corresponding with KI values, and it is not very likely to occurrence severe weather. Compared with case 1, case 2 is in a relatively weak thermodynamic environment for severe weather. Overall, from these five simulated results, the Thompson scheme (Figure 6.13 (b)) shows that its high magnitude TT areas are slightly in the north of the expected region (location of Kentish Flats Extension and Thanet Extension).

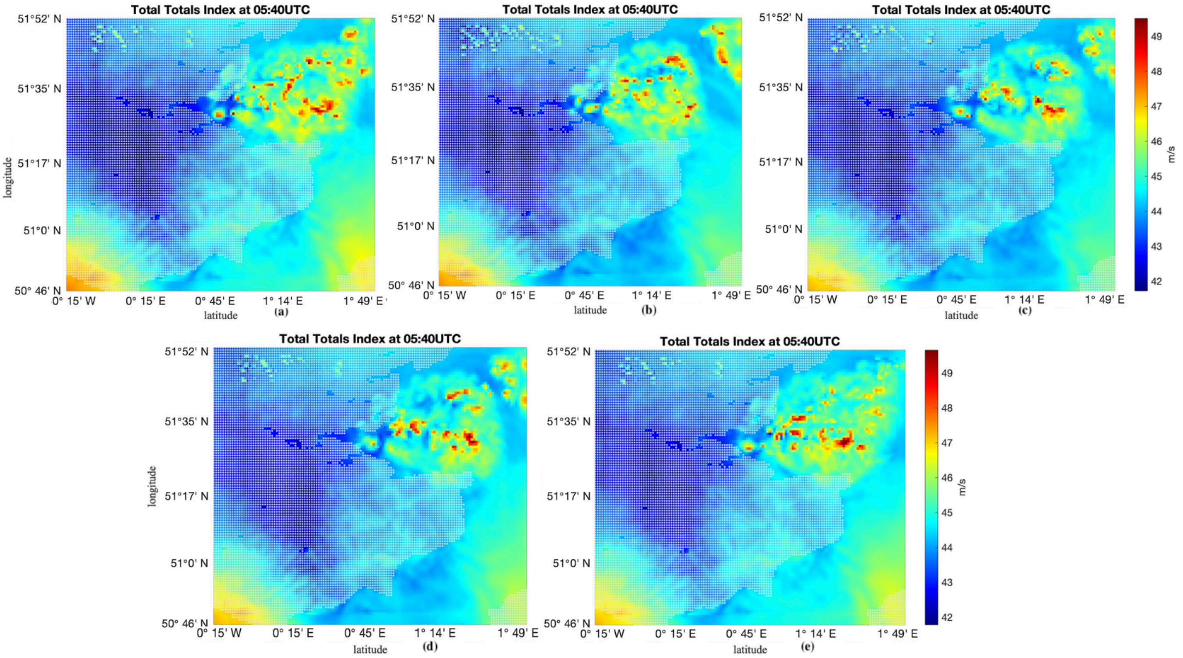

Figure 6.13: Total Totals Index at 05:40 UTC by WSM6 scheme (a), Thompson (b), Milbrandt-Yau (c), Morrison (d), WDM6 (e)

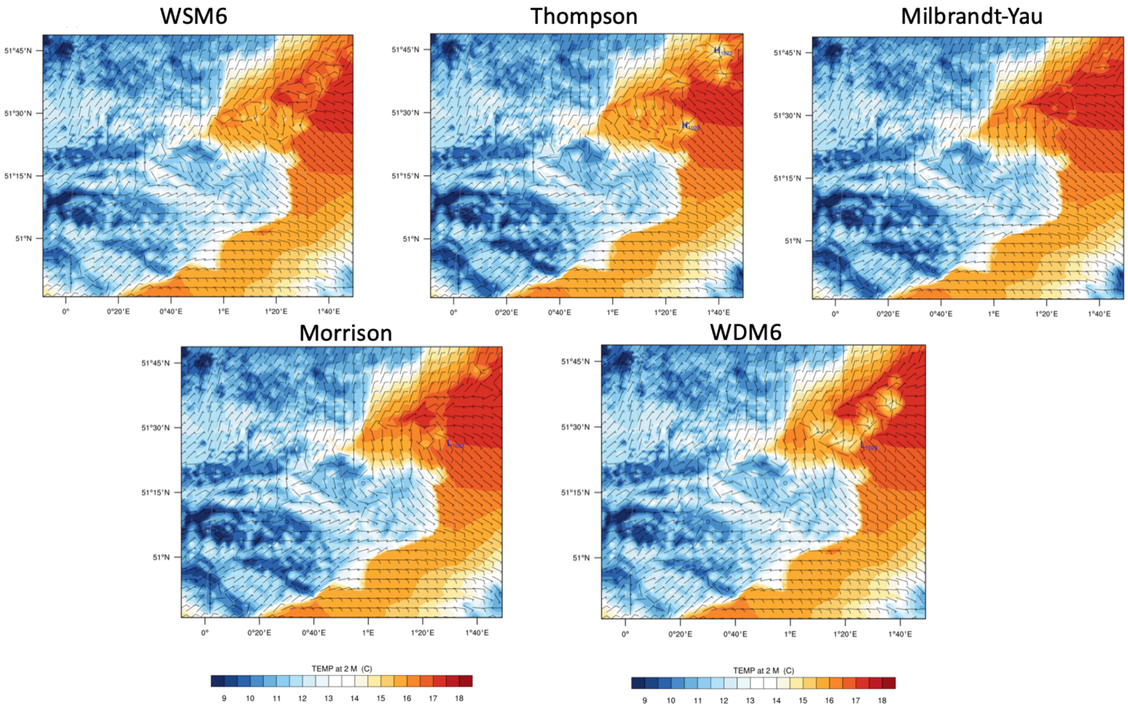

Figure 6.14: Surface temperature (shaded), wind barb and surface pressure centers from five schemes at 05:40 UTC

Similarly, as the case I in chapter 5, a persistent SST gradient is shown clearly in the preferred area at the time of all five reported waterspouts, and this gradient can also be noticed from all schemes (Figure 6.14). Nevertheless, several differences can be found in each scheme. Specifically, the WDM6 and New Thompson schemes present clear surface divergence with an apparent lower temperature than its surroundings, and the temperature difference is about 2-3 °C. Besides, the Morrison and WSM6 schemes show a similar pattern, but their strength is weaker due to the difference within 1 °C. In this case, the SST gradient pattern is the same as in case study I, which means waterspouts might relate to the SST gradient.

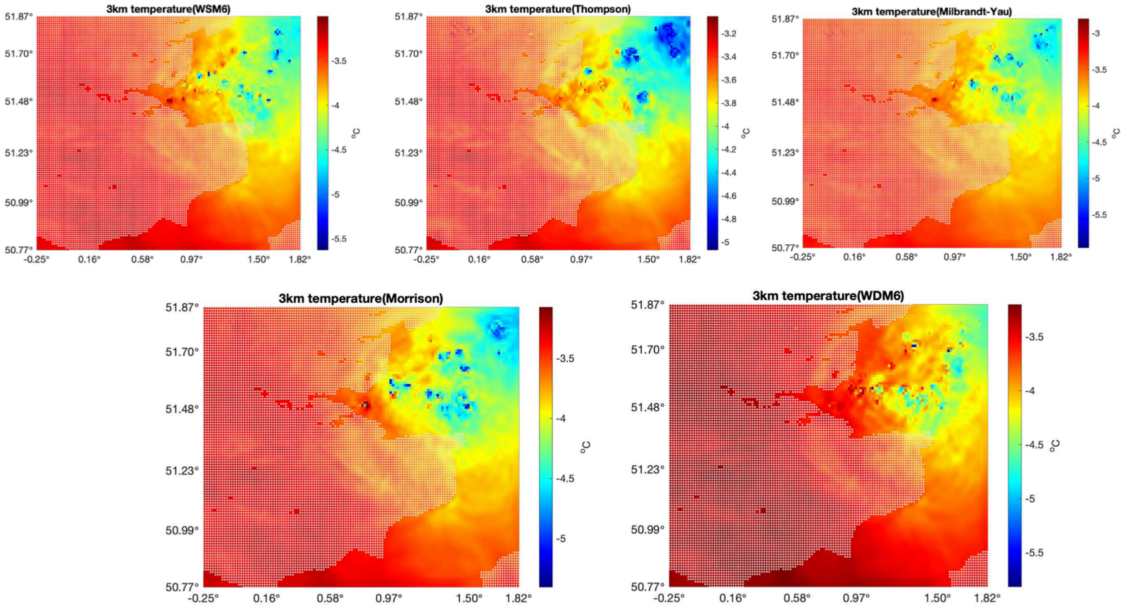

Figure 6.15: 3km temperature from five schemes scheme at 05:40 UTC

In addition, Figure 6.15 shows the cold pool aloft at the corresponding location of the SST gradient area. As mentioned above, the cold pool aloft is a cooler pocket of air in the higher levels of the atmosphere, between about 3 km and 6 km. Therefore, the cold pool aloft helps the development of clouds and thunderstorms in the higher part of the atmosphere. This is because the air parcel passes through the cold pool aloft, and then the parcel was cooling as it rises. Finally, it is still relatively warmer than the cold pool, and it can continue going up. In fact, since the air parcel is allowed to rise, it induces more cloud development and thunderstorm potential, matching what waterspouts need.

To summarise, the areas that are reported waterspouts occurrence show up in the simulations from five microphysics schemes (thermodynamic parameters):

- When the CAPE values are higher than the surrounding regions; however, the CAPE values should not be too large.
- When the LCL and LFC heights are lower than their surroundings.
- When the areas have higher values of two thermodynamic parameters K Index and TT values than the neighbor.
- When the areas show a strong SST gradient at the wind convergence boundary, and the corresponding higher temperature at 3km show cold pool aloft.

In line with expectations, the location of waterspouts occurrence shows that CAPE values are higher than that of other places. For example, this case shows that CAPE values are regarded as a weak instability range because the value is no more than 200 J/kg in the interest area. According to the CAPE values computed in case I, the values are larger than that in case II. Therefore, the environment of the case I is more unstable than that in case II. In fact, waterspouts of the case study I are stronger than that in case study II. Especially low-level layers, CAPE might have a relation with strong upward accelerations. This updraft, which has already shown in the results, implies the stretch vertical vorticity, and this will be discussed in detail later. Besides, the same effect is associated with the occurrence of waterspouts with low LFC height, which means that air parcel gains positive buoyancy at a low level. In this condition, upward acceleration can start from a low height, and vortex stretching is closer to the surface. Moreover, the same result for LCL height can be seen. Based on the research of Rasmussen and Blanchard (1998), LCL that is lower than 800 m can be used as an indicator for significant tornadoes. Overall, from the results of this study, the LCL heights are satisfied for both cases.

The KI consists of two parts: the vertical temperature lapse rate, and low-level moisture, and it provides thunderstorm potential. The temperature lapse rate also plays a role in the process of tornadogenesis if it is steep enough. Based on the KI range for waterspouts from previous researches, it is expected to be between 20 and 35. In this research, KI values,30, are shown in the second case. This value is in this range, but it is slightly smaller than that in case I. Compared with KI, TT represents a condition of lapse rate from higher levels. Furthermore, a range of TT value is between 40 to 60. For case II, 49 is provided for the TT value, which is also slightly smaller than that in case I. Therefore, these smaller values can tell whether the environmental instability of case II is relatively weaker than that in the first case.

6.4. Wind shear

According to Chapter 5, the threshold for 0–1 km storm-relative helicity (SRH_{0-1km}) is 75 m^2/s^2. Figure 6.16 (e) is the only one that presents SRH value,which is higher than the threshold 75 m^2/s^2 at a similar area of high CAPE, KI and TT values. This area overlaps with the region where presented low LFC and LCL height. Besides, SRH_{0-1km} values are equal to about 15-35 m^2/s^2 at the area of interest. Because the helicity value is computed relative to a given storm's motion, SRH is also called Storm-Relative Helicity. Regarding the physical meaning of SRH_{0-1} value, the negative sign represents the moving direction of a storm system, which is a left mover. Therefore, for any given wind profile, a storm motion resulting in a negative SRH value can be provided. Also, SRH is a measurement of the potential for cyclonic updraft rotation in right-moving supercells. Thus, a left mover shows a negative value. Based on the threshold of SRH_{0-1} from Table 5.3, there are possibilities of weak waterspouts (F0) when SRH_{0-1} is in the range 15-35 m^2/s^2.

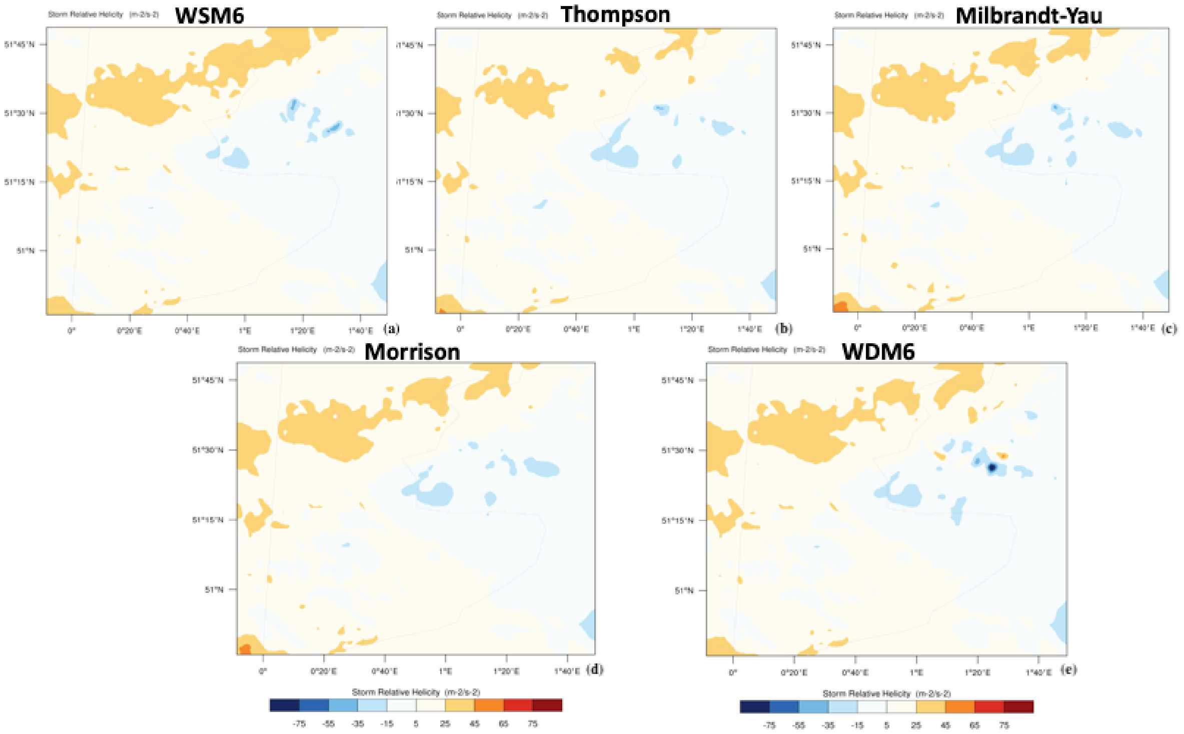

Figure 6.16: Storm Relative Helicity (SRH) at 05.40 UTC by WSM6 scheme (a), Thompson (b), Milbrandt-Yau (c), Morrison (d), WDM6 (e)

From Figure 6.17 and Figure 6.18, the maximum values of the 0-1 km vertical wind shear and 0-6 km vertical wind shear are 11 m/s and 10 m/s, respectively. These two values are similar. Most interestingly, north of the channel shows higher shear at the low level (0-1 km bulk shear), but higher shear areas are shown south of the channel at a high level (0-6 km bulk shear). Although some large shear values are shown on land, the large shears are given at our target region overseas from simulations. The 0-1 km bulk shear (BS01) for the WDM6 scheme illustrates three-circle shape areas with a higher BS01 value (up to about 11 m/s) at the location, overlapping with the special areas of other parameters. WSM6 and Thompson scheme present similar but weak situations, especially WSM6 with a maximum of 10 m/s. Thompson scheme shows the same strength as that in WDM6. However, the shape of the high-value region is only the half-circle. On the other hand, Milbrandt-Yau and Morrison schemes show the weakest simulation of these five schemes. Note that a maximum BS01 value is about 8 m/s in these two weak schemes. Recalling from Chapter 5, the indicators of tornado strength for bulk shear from SkyStef's weather are given in Table 5.4, and these indicators can be used for comparisons. Based on these, the BS01 value from all schemes is satisfied with the intensity of F0, which means a possibility of relatively weak waterspouts form. As for 0-6 km bulk shear (BS06), the WDM6 scheme gives the largest value, about 10 m/s at interest area. Subsequently, Thompson and Morrison's simulation show BS06 at the same strength but in a smaller high-value area. Besides, the Milbrandt-Yau scheme shows the weakest result of BS06 (about 8 m/s). Compared with SkyStef's weather threshold (Table 5.4), BS06 values for all simulations, however, are too small.

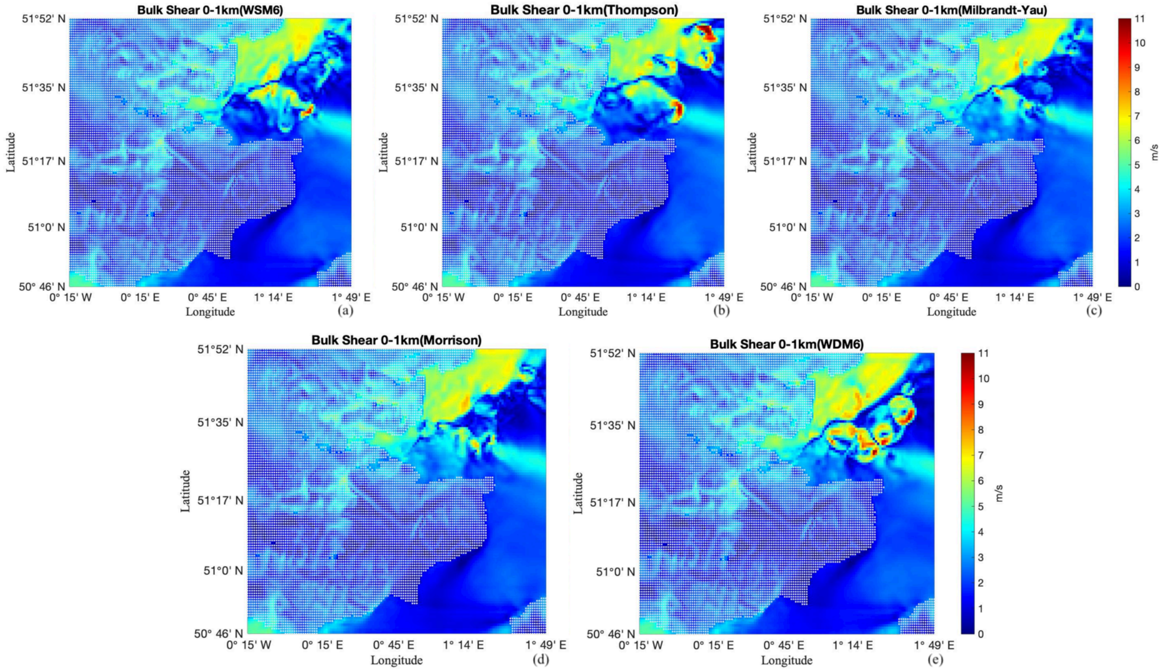

Figure 6.17: 0–1 km Bulk Shear (BS01) at 05.40 UTC by WSM6 scheme (a), Thompson (b), Milbrandt-Yau (c), Morrison (d), WDM6 (e)

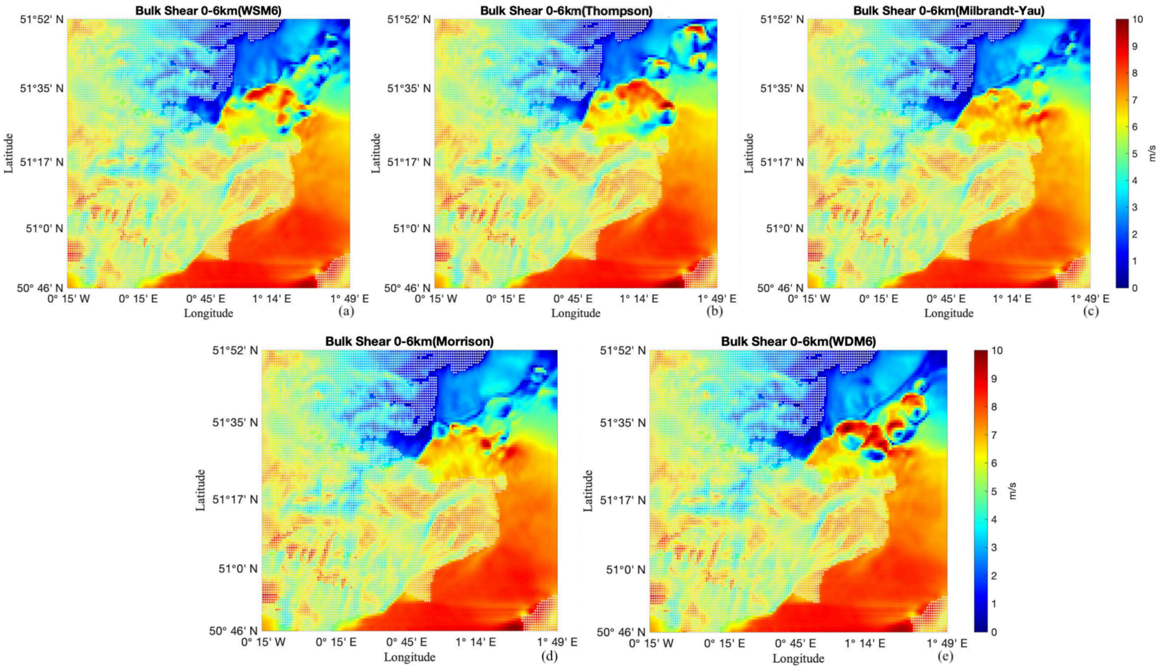

Figure 6.18: 0–6km Bulk Shear (BS06) by WSM6 scheme by WSM6 scheme (a), New Thompson (b), Milbrandt-Yau (c), Morrison (d), WDM6 (e)

The BRN shear term (Equation 2.6) is the denominator of the bulk Richardson number. From the empirical scale of BRN shear, values from 25 to 50 reflect the likelihood of tornadic and non-tornadic storms. Otherwise, values near and above 50 are associated with tornadoes. BRN shear is sensitive to low-level winds. Higher values of low-level winds represent more possibilities of tornadic storms than that for non-tornadic storms. On the other hand, lower BRN shear values represent weaker environmental wind shear. In contrast, higher values are generally associated with an increased risk of tornadic supercells, as shown in Figure 6.19, which denominates BRN shear from five schemes. Similarly, in the area of interest, the result of the WDM6 scheme gives the largest and strongest BRN shear value, which is about 22 m^2/s^2, followed by simulation from Thompson, which shows slightly weak (about 20m^2/s^2) and smaller region. Last but not least, the rest three schemes present BRN shear between 10-14 m^2/s^2, which are associated with quite a slight possibility of tornadic and non-tornadic storms.

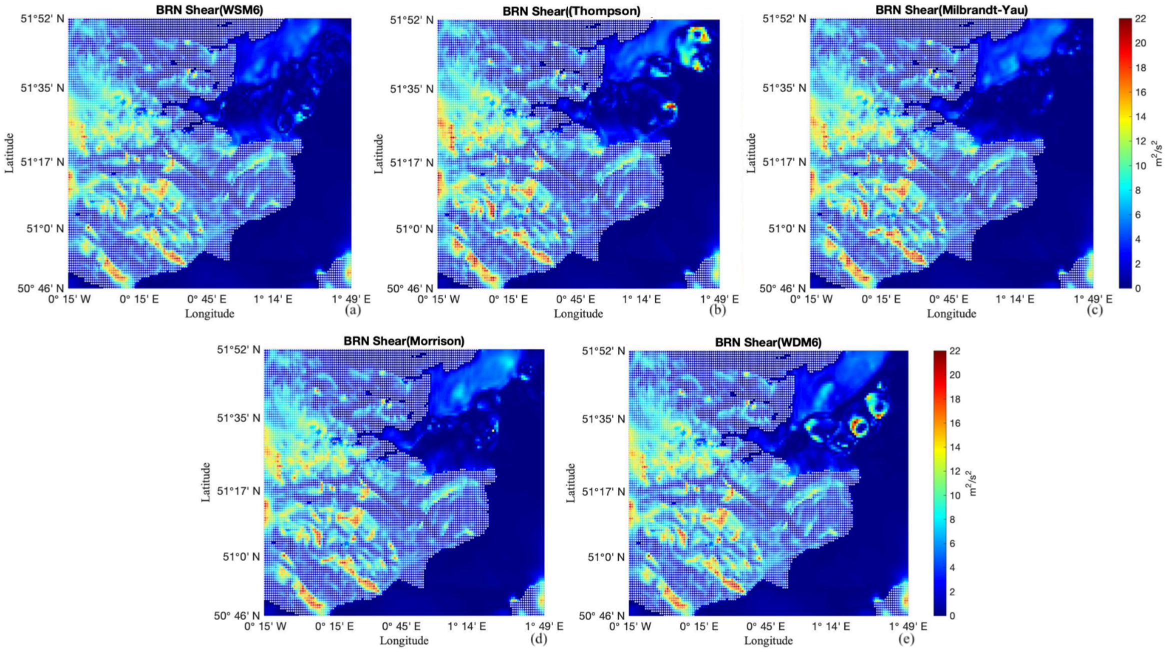

Figure 6.19: BRN shear at 05.40 UTC by WSM6 scheme (a), Thompson (b), Milbrandt-Yau (c), Morrison (d), WDM6 (e)

To summarise, in terms of wind shear, the areas that are reported waterspouts occurrence show up in the simulations from five microphysics schemes:

- When the SRH values are higher than the surrounding regions, and the locations are overlapping with other specific regions as mentioned in Section 6.3.
- When the bulk shear value is higher than its surrounding value.
- When the areas have higher values of BRN shear in comparison with the surrounding areas.

In general, low-level shear increases strongly with the intensity of the waterspouts. That is, BS01 is a good indicator to distinguish different intensity levels of a waterspout. Also, strong low-level wind shear implies vorticity along a horizontal axis, which is an important ingredient of waterspouts development. Although a few events are associated with strong waterspouts, most of the events belong to non-mesocyclonic tornadoes. Note that the mean BS01 value of waterspouts is 5.6 m/s that is in the range of F0 possibility (Groenemeijer and Van Delden, 2007). In the case II study, the WDM6 scheme did not give a too large BS01 value (about 11 m/s). Besides, for the other schemes, three of them simulate BS01 values, which are more than 7 m/s. Moreover, the 0–6 km shear shows much less difference between the F0 and F1 than that from 0–1 km bulk shear. The BS06 from case study II for all schemes are less than the smallest value from the range of F0 (23 m/s) and F1 (19 m/s) range.

0–1 km storm-relative helicity (SRH_{0-1km}) is also used in this study. Rasmussen shows that SRH_{0-1km} is useful to separate tornadic and non-tornadic supercells. Moreover, SRH shows the environmental horizontal vorticity, and the low-level shear is important, especially for non-mesocyclonic tornadoes. The mean value for SRH_{0-1km} is 7 m^2/s^2, which is easy to match. For example, in Figure 6.16, the light yellow shaded area shows that the values of SRH_{0-1km} are in the range of 0-25 m^2/s^2.

In conclusion, wind shear is another essential part of waterspouts. In this study, three parameters, including bulk shear 0-1km (BS01), bulk shear 0-6 km (BS06) and storm-relative helicity (SRH), are mainly analyzed. All of them show higher values in the interest area.

6.5. Updraft and downdraft profiles

Figure 6.20 and Figure 6.21 show the simulated 10 m maximum updraft and downdraft velocities at 05:40 UTC in the finest domain. An interesting phenomenon is that no visible divergence presents in plots of 10 m maximum wind speed for Milbrandt-Yau and Morrison scheme (Figure 6.24 (c), (d)). However, quite strong upward movements (approximate 8 m/s) were given by Figure 6.20 (C) and (d). Meanwhile, they also have relatively large downdraft velocity (about 3 m/s). It is noticeable that the WDM6 scheme simulated the strongest downdraft velocity with about 4 m/s and strongest updraft velocity about 9 m/s.

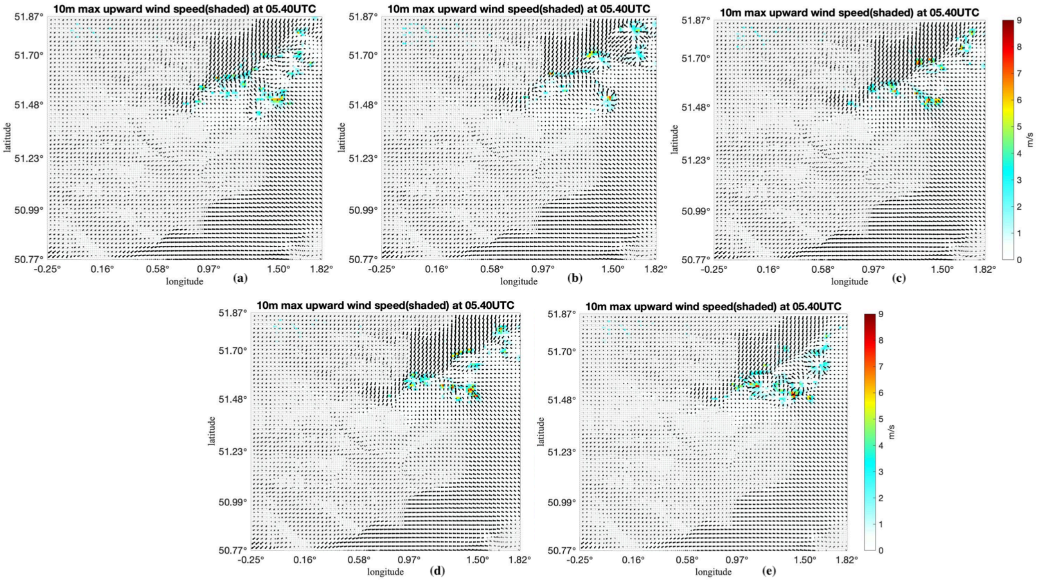

Figure 6.20: 10 m max updraft velocity at 05:40 UTC by WSM6 (a), Thompson (b), Milbrandt-Yau (c), Morrison (d), WDM6 (e) schemes

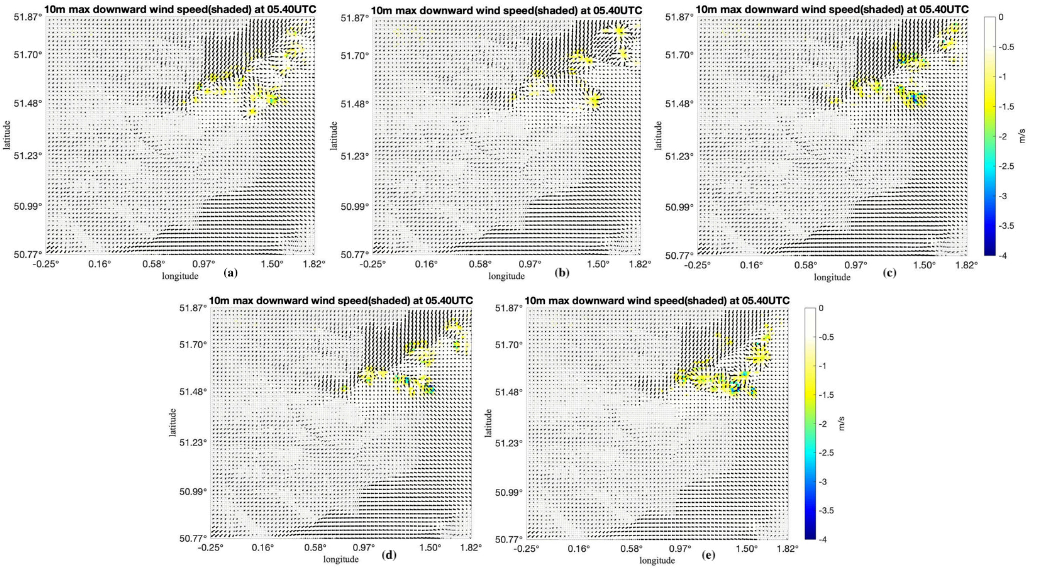

Figure 6.21: 10 m max downdraft velocity at 05:40 UTC by WSM6 (a), Thompson (b), Milbrandt-Yau (c), Morrison (d), WDM6 (e) schemes

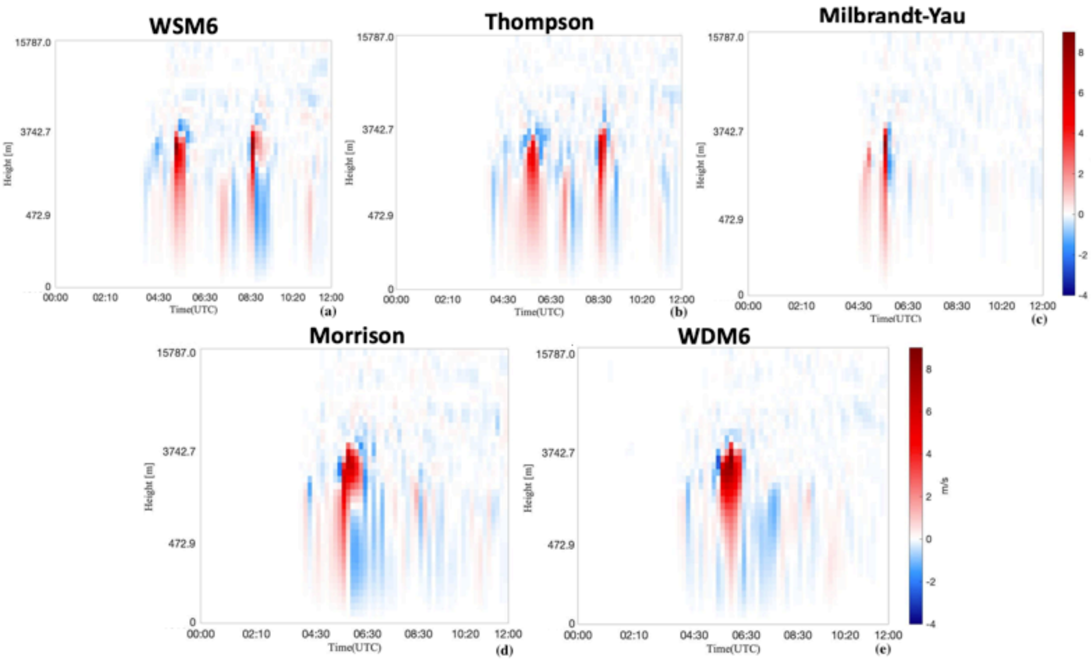

Figure 6.22: Model simulated vertical velocity (upward) at 05:40 UTC by WSM6 (a), Thompson (b), Milbrandt-Yau (c), Morrison (d), WDM6 (e) schemes

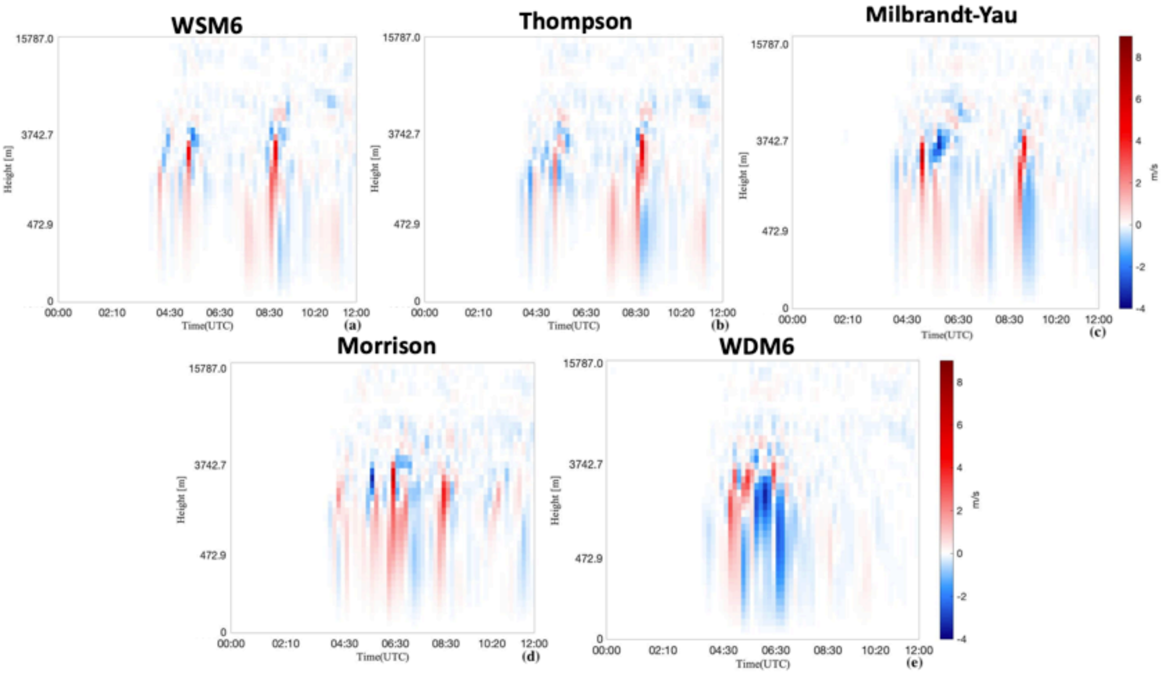

Figure 6.23: Model simulated vertical velocity (downdraft) at 05:40 UTC by WSM6 (a), Thompson (b), Milbrandt-Yau (c), Morrison (d), WDM6 (e) schemes

Figure 6.22 and Figure 6.23 show the time series of the strongest points of vertical movement from 10 m maximum updraft and downdraft velocity maps. From the upward simulation (Figure 6.22), only the Morrison scheme simulates an updraft core with the associated downdrafts around 05:40 UTC. Besides, others present updraft cores (magnitude more or less between 6 m/s and 8 m/s) with increasing ascent movement from the low level. And the WDM6 scheme shows the strongest updraft core at the same time. The simulation of the Milbrandt-Yau scheme shows the shortest duration, and the Thompson scheme shows the weakest strength(approximate 6 m/s). For the downdraft simulation (Figure 6.23), only the WDM6 scheme simulates a clear and strong downdraft at around 05:40 UTC, whereas other schemes only show about 2 or 3 m/s downward movement. For example, Thompson and WSM6 schemes give relatively weak vertical velocity.

6.6. Surface winds

Figure 6.24 is derived from modeled 10 m max wind field in the innermost domain at 05.40 UTC of August 31, 2018. It is noticeable that Figure 6.24 (e) shows two clear relative strong divergences with the highest wind speed (10 m/s) and two relatively weaker wind speeds that are between 7 m/s and 8 m/s. The simulation of 10m max wind by Thompson scheme (Figure 6.24 (b)) also presents a divergence pattern, but it is much weaker (about 7-8 m/s) than that in WDM6. On the other hand, the rest three schemes simulate a clear surface wind convergence line, and the line is near the interest area. At the high wind speed side of the line, wind speeds are in the range of 6-7 m/s, and the low wind speed side is clam, which means that the speed is no more than 4 m/s.

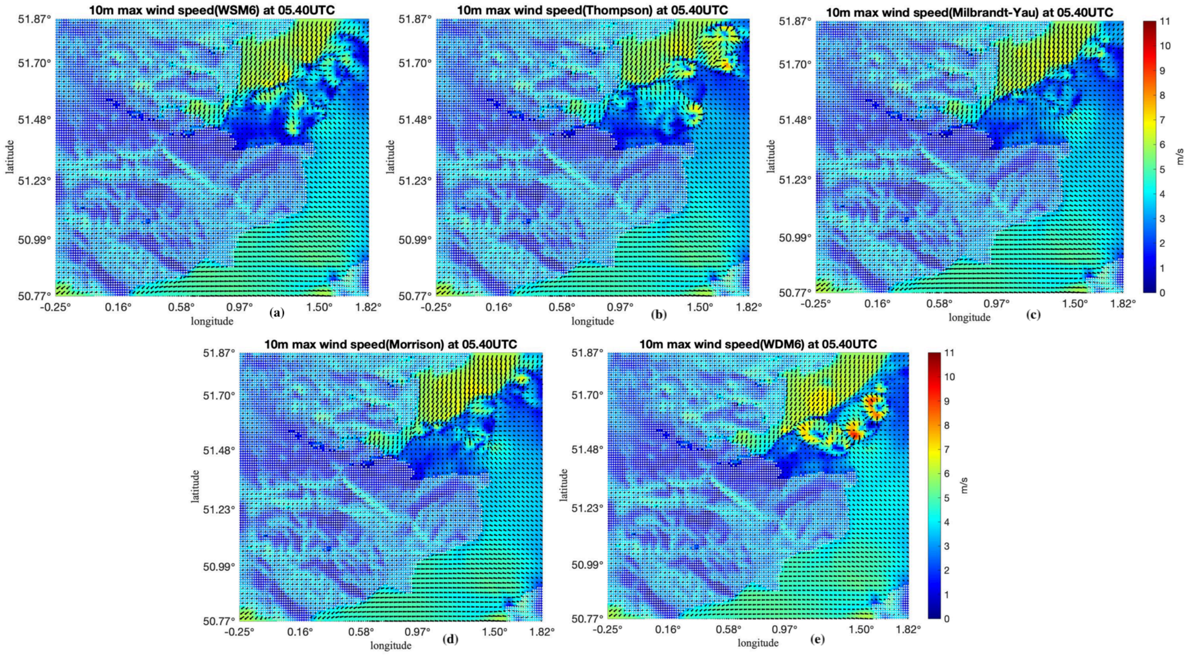

Figure 6.24: 10 m maximum wind speed at 05:40 UTC (shaded present wind speed, vector present wind direction) by WSM6 (a), Thompson (b), Milbrandt-Yau (c), Morrison (d), WDM6 (e) schemes

Figure 6.25 presents time series of 10 m max wind, surface pressure, surface temperature, and total accumulated precipitation of five points selected from each scheme. All schemes' simulations at least capture a clear wind speed peak between 04 UTC and 06 UTC. Especially for the peak of the WDM6 scheme, it is the only one speed more than 10 m/s. As for the corresponding time of surface pressure, only the WDM6 scheme shows that the pressure is increasing, and the pressure of the WSM6 scheme rise slightly. Overall, temperatures for all of them decrease at the corresponding time. Moreover, the fluctuation of temperatures from Thompson and Morrison schemes are shown before the heavier rain coming.

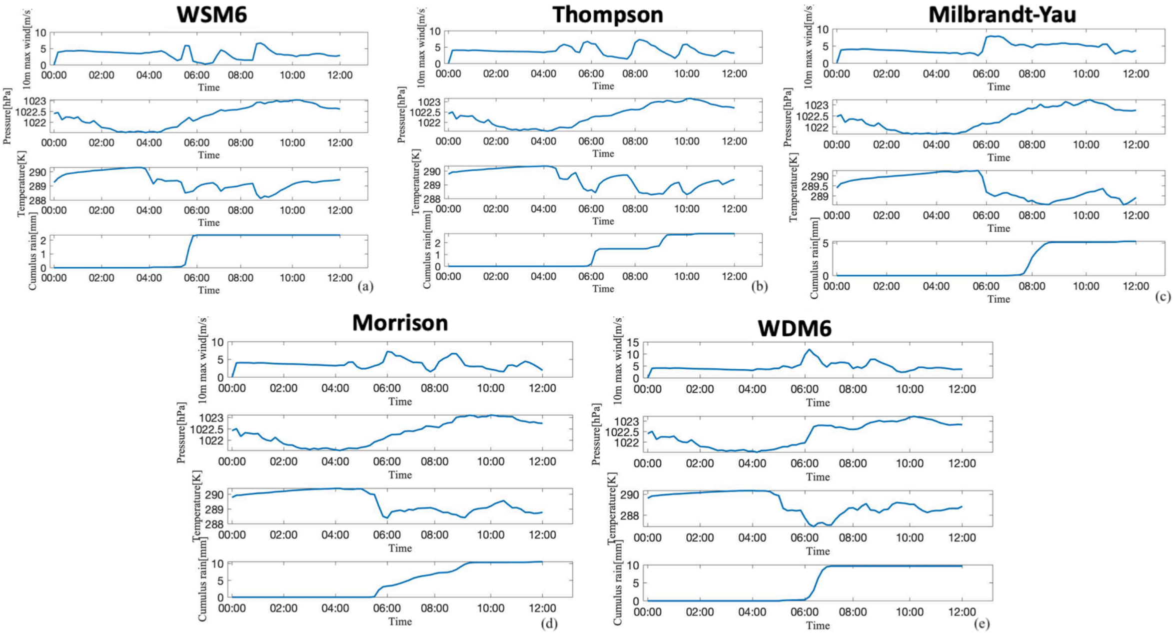

Figure 6.25: Time series of 10 m max wind, surface pressure, surface temperature and total cumulus precipitation by WSM6 (a), Thompson (b), Milbrandt-Yau (c), Morrison (d), WDM6 (e) schemes)

6.7. The Szilagyi Waterspout Nomogram

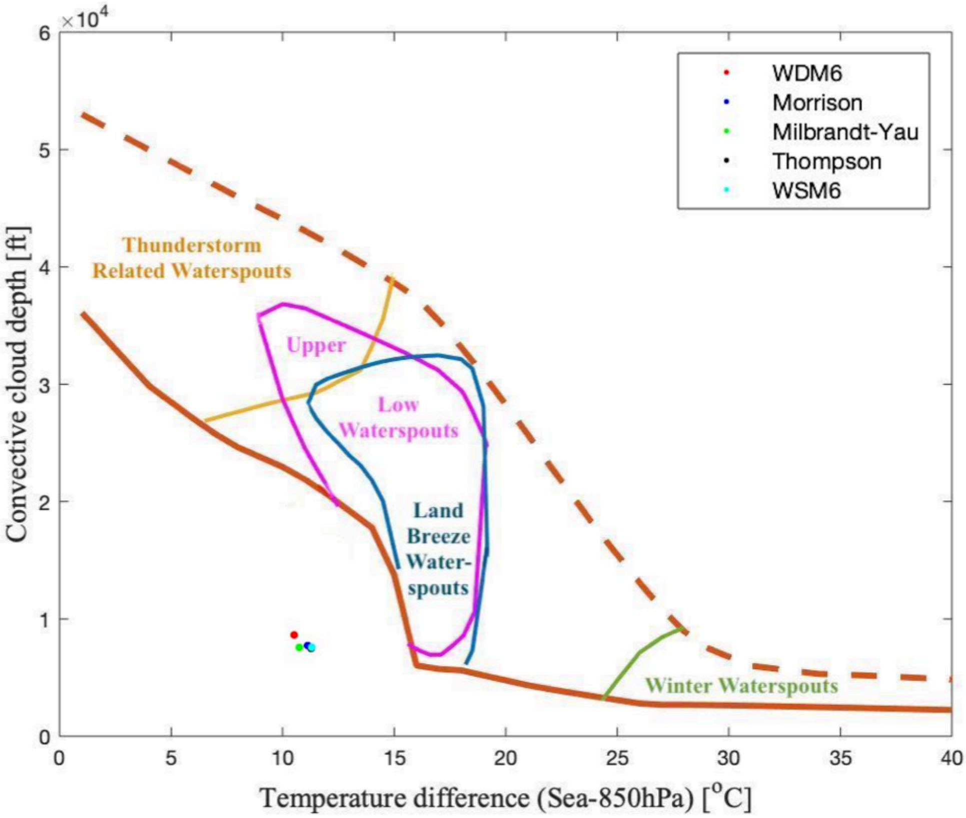

Figure 6.26: The Szilagyi Waterspout Nomogram for the second case

The Szilagyi Waterspout Nomogram is an empirical technique that consists of three predictors: temperature difference, convective cloud depth, and a wind speed at 850 hPa. The convective cloud depth match with vertical movement profile as well (Figure 6.22 and Figure6.23). The vertical velocity reaches to more than 3000 m, which is approximately 9000-10000 ft. The temperature difference of this case is between 10-11 °C. Compared with the case study I, case study II is a relatively weaker event. This conclusion is implied by many other parameters mentioned before. It makes sense, as we know that the second case is a fair-weather waterspout.

The values from this case study in the Szilagyi nomogram are depicted by Figure 6.26. In this case, five points are totally used. Each scheme selects one point. As we can see from the nomogram, none point from this case is shown in the range. Besides, many waterspouts show at a similar area of case study II (Dotzek et al., 2010), it might add a new possible region if the Szilagyi nomogram use outside of the Great Lakes area.

7

Conclusion and Future Work

7.1. Summary

In this research, two waterspout events are analyzed. Both of them occurred near or across offshore wind farms over the southern part of the North Sea. For the first outbreak case, five waterspouts events were reported on September 1, 2017. Events on this day belong to the tornadic type. Because of many lightning strikes in that area during the period. In contrast, the second case is a fair-weather type, and only one waterspout was observed. Fortunately, none of them result in any loss or damage so far. However, some common characters are found in the environment during the occurrence of waterspouts. Through state-of-the-art mesoscale modelling in conjunction with five microphysics schemes, the environment in terms of synoptic, thermodynamic, and wind conditions, and a few common features are identified.

According to literature, five synoptic types are strongly correlated with waterspouts, southwesterly flow (SW), long-wave trough (LW), short-wave trough (SWT), closed low (CLOSED) and non-gradient pressurefield (NG). For both cases selected in this study, the circulation flow at the 500 hPa level belongs to the SW and LW, and the surface synoptic charts show some unstable system, such as trough and front.

Five thermodynamic indices of instability are used in this research, including CAPE, LFC, LCL, TT, and KI. It was found that waterspouts can develop in different values of CAPE. However, the location of the event's occurrence always shows a relatively high CAPE value than that of the surrounding area. Besides, in general, CAPE value is in a weak range (under 1000 J/kg). For LFC and LCL, their heights are relatively low (below 600 m) in these two cases. Finally, TT and KI indices quantify the condition of lapse rate below the 500 hPa layer and low-level moisture. Furthermore, the steep lapse rate and moist low level have a positive effect on the formation of waterspouts.

We have also found that wind shear is stronger than the surrounding at events' locations. For example, bulk shear in 0-1 km and 0-6 km show higher values than the surrounding areas. According to Renko et al. (2019), the BS06 values higher than 20 m/s mostly implies occurrence of mesocyclonic tornadoes. In these two case studies, all BS06 values are less than 20 m/s, but the simulations from WDM6 scheme provide the closest value (16m/s) to 20 m/s. Besides, most simulations show that BS01 values are more or less equal to the median value of BS01 (7 m/s). Similarly, only the BS01 values from WDM6 scheme (18 m/s) are far more than the others. Therefore, we can generally conclude that case study II and the waterspout occurred at 10:20 UTC in the case study I are non-mesocyclonic. For non-mesocyclonic type, a convergence line or boundary is one of the most significant roles, and this pattern also appears in most of the simulations.

High SRH values indicate the existing of environmental horizontal vorticity. When the high SRH value encounters strong vertical movements, the surface vorticity is stretching to higher levels, which is the main process of non-mesocyclonic tornadogenesis. Both these cases show higher SRH value areas overlapped with the lines of strong vertical movement.

In addition, five microphysics schemes of the WRF model are used in this study. It was found that the WDM6 scheme always generates the strongest convective environment, and thus, its results can be the most representative of the waterspout environment. For the other four schemes, the general features can be found as well, but the much weaker intensity was found in those simulations.

Meteorologists utilize the Szilagyi waterspouts nomogram for the forecast of waterspouts. Based on our research, we reckon that the threshold area should be modified for the North Sea region.

In conclusion, if one area is co-located with all required values from the parameters mentioned above, this area is in a favorable environment for waterspout and has a high possibility to occur waterspout events.

7.2. Limitations and future works

This research has a few limitations. The first and foremost is the lack of severe weather observation. Visual observations by one or two observations may lead to uncertainty in the location and/or timing of the waterspout events. Additionally, the availability of more radiosondes and other instruments (e.g. floating lidar) with higher spatial density would have tremendously benefited this study. Another limitation is the small sample size over the study area, and excessive uncertainty in individual cases.

For future research about this topic, except deal with the limitations, grid size can be increased. The diameter of waterspouts is usually several hundred meters, the finest domain uses a 1km grid in this research; it may cause that some interesting characters can not be resolved. Simulations at gray-zone resolutions are recommended for further studies.

In this study, the effects of the planetary boundary layer (PBL) physics schemes are not examined. All the simulation utilized a non-local PBL scheme, called the Yonsei University (YSU) scheme. More PBL parameterization can be used for simulation. For example, Shin-Hong, which is scale aware, and MYNN3, which is a higher-order closure scheme. Moreover, different combinations of PBL physics schemes and microphysics schemes can be designed for better performance. WRF provides several other microphysics schemes which should be tested in further research.

Bibliography

[1] 4C Offshore. Offshore wind installations map over the north sea. `https://www.4coffshore.com/offshorewind/`, 2019. Accessed 2020.

[2] Bateaux. Reflectivity. `https://www.pinterest.com/pin/158400111864762535/`, 2016. Accessed 2020.

[3] Blitzortung.org Contributors. A worldwide, real time, community collaborative lightning location network. `https://www.lightningmaps.org/#m=oss;t=3;s=0;o=0;b=;ts=0;`, 2003-2020. Accessed 2020.

[4] Raymond H Brady and Edward J Szoke. A case study of nonmesocyclone tornado development in northeast colorado: Similarities to waterspout formation. *Monthly weather review*, 117(4):843–856, 1989.

[5] D Brown and J Rothfuss. An approach to waterspout forecasting for south florida and the keys. Technical report, Internal report, National Oceanic and Atmospheric Administration, Miami ..., 1998.

[6] D Burgess and M Foster. Test of helicity as a tornado forecast parameter. In *Preprints, 1 61h Conf on Severe Local Storms, Alberta, Canada, Amer. Meteor. Soc*, pages 588–592, 1990.

[7] HR Byers. „and rr braham, jr., 1949: The thunderstorm. *US Govt. Printing Off., Washington, DC*, 1949.

[8] Merete Bruun Christiansen and Charlotte B Hasager. Wake effects of large offshore wind farms identified from satellite sar. *Remote Sensing of Environment*, 98(2-3):251–268, 2005.

[9] Jean-Martial Cohard and Jean-Pierre Pinty. A comprehensive two-moment warm microphysical bulk scheme. i: Description and tests. *Quarterly Journal of the Royal Meteorological Society*, 126 (566):1815–1842, 2000.

[10] Jean-Martial Cohard, Jean-Pierre Pinty, and Carole Bedos. Extending twomey's analytical estimate of nucleated cloud droplet concentrations from ccn spectra. *Journal of the atmospheric sciences*, 55(22):3348–3357, 1998.

[11] Waylon G Collins, Charles H Paxton, and Joseph H Golden. The 12 july 1995 pinellas county, florida, tornado/waterspout. *Weather and forecasting*, 15(1):122–134, 2000.

[12] Jeffrey P Craven, Harold E Brooks, John A Hart, et al. Baseline climatology of sounding derived parameters associated with deep, moist convection. *Natl. Wea. Dig*, 28(1):13–24, 2004.

[13] Jonathan M Davies. Estimations of cin and lfc associated with tornadic and nontornadic supercells. *Weather and forecasting*, 19(4):714–726, 2004.

[14] Jonathan M Davies. Tornadoes in environments with small helicity and/or high lcl heights. *Weather and forecasting*, 21(4):579–594, 2006.

[15] Jonathan M Davies. Total cape, low-level cape, and lfc in significant tornado events with relatively high lcl heights. In *Preprints, 23rd Conf. Severe Local Storms, St. Louis, MO, Amer. Meteor. Soc*, pages 1–3. Citeseer, 2006.

[16] Charles A Doswell. Severe convective storms—an overview. In *Severe convective storms*, pages 1–26. Springer, 2001.

[17] Charles A Doswell III and Jeffry S Evans. Proximity sounding analysis for derechos and supercells: An assessment of similarities and differences. *Atmospheric Research*, 67:117–133, 2003.

[18] Nikolai Dotzek. An updated estimate of tornado occurrence in europe. *Atmospheric Research*, 67:153–161, 2003.

[19] Nikolai Dotzek, Stefan Emeis, Christiana Lefebvre, and Jürgen Gerpott. Waterspouts over the north and baltic seas: Observations and climatology, prediction and reporting. *Meteorologische Zeitschrift*, 19(1):115–129, 2010.

[20] ECMWF. Era5. `https://cds.climate.copernicus.eu/cdsapp#!/dataset/reanalysis-era5-pressure-levels?tab=form`, 2020. Accessed 2020.

[21] Muhammed ElTahan and Mohammed Magooda. Evaluation of different wrf microphysics schemes: severe rainfall over egypt case study. *arXiv preprint arXiv:1711.04163*, 2017.

[22] European Severe Weather Database. A waterspout near wind farm on 2019 august 1. `https://www.eswd.eu`, 2018. Accessed 2020.

[23] Georg Müller and Rogier Floors. Radar and satellite images. `https://www.wetterzentrale.de`, 2020. Accessed 2020.

[24] J George. 1960: Weather forecasting for aeronautics.

[25] JH Golden. Waterspouts. 2003.

[26] Joseph H Golden. The life cycle of florida keys' waterspouts. i. *Journal of Applied Meteorology*, 13(6):676–692, 1974.

[27] Joseph H Golden. Scale-interaction implications for the waterspout life cycle. ii. *Journal of Applied Meteorology*, 13(6):693–709, 1974.

[28] Joseph H Golden. An assessment of waterspout frequencies along the us east and gulf coasts. *Journal of Applied Meteorology*, 16(3):231–236, 1977.

[29] Joseph H Golden and Howard B Bluestein. The noaa–national geographic society waterspout expedition (1993). *Bulletin of the American Meteorological Society*, 75(12):2281–2288, 1994.

[30] PH Groenemeijer and A Van Delden. Sounding-derived parameters associated with large hail and tornadoes in the netherlands. *Atmospheric research*, 83(2-4):473–487, 2007.

[31] Pieter Groenemeijer and Thilo Kühne. A climatology of tornadoes in europe: Results from the european severe weather database. *Monthly Weather Review*, 142(12):4775–4790, 2014.

[32] Higgins Storm Chasing. Illustration of a waterspout life cycle and structures. `https://higginsstormchasing.com/what-are-waterspouts/`, 2019. Accessed 2020.

[33] Song-You Hong and Jeong-Ock Jade Lim. The wrf single-moment 6-class microphysics scheme (wsm6). *Asia-Pacific Journal of Atmospheric Sciences*, 42(2):129–151, 2006.

[34] Song-You Hong, Jimy Dudhia, and Shu-Hua Chen. A revised approach to ice microphysical processes for the bulk parameterization of clouds and precipitation. *Monthly weather review*, 132(1):103–120, 2004.

[35] IEC. Iec international standard 61400-1 part i: Design requirements, 2005.

[36] IEC. Iec 61400-3. *Wind Turbines—Part 3: Design Requirements for Offshore Wind Turbines*, 2009.

[37] DRP Jones, D Burgess, and M Foster. Test of helicity as a tornado forecast parameter, preprints, 16th conf. on severe local storms, kanaskis, ab, canada. *Amer. Meteor. Soc*, pages 588–592, 1990.

[38] Edwin Kessler. On the distribution and continuity of water substance in atmospheric circulations. In *On the distribution and continuity of water substance in atmospheric circulations*, pages 1–84. Springer, 1969.

[39] Marat Khairoutdinov and Yefim Kogan. A new cloud physics parameterization in a large-eddy simulation model of marine stratocumulus. *Monthly weather review*, 128(1):229–243, 2000.

[40] Peter J Kirk. An updated tornado climatology for the uk: 1981–2010. *Weather*, 69(7):171–175, 2014.

[41] Humphrey W Lean, Peter A Clark, Mark Dixon, Nigel M Roberts, Anna Fitch, Richard Forbes, and Carol Halliwell. Characteristics of high-resolution versions of the met office unified model for forecasting convection over the united kingdom. *Monthly Weather Review*, 136(9):3408–3424, 2008.

[42] Bowen Li, Sukanta Basu, Simon J Watson, and Herman WJ Russchenberg. Mesoscale modeling of a 'dunkelflaute'event.

[43] Kyo-Sun Sunny Lim and Song-You Hong. Development of an effective double-moment cloud microphysics scheme with prognostic cloud condensation nuclei (ccn) for weather and climate models. *Monthly weather review*, 138(5):1587–1612, 2010.

[44] Yuh-Lang Lin, Richard D Farley, and Harold D Orville. Bulk parameterization of the snow field in a cloud model. *Journal of climate and applied meteorology*, 22(6):1065–1092, 1983.

[45] Agostino Manzato. The 6 h climatology of thunderstorms and rainfalls in the friuli venezia giulia plain. *Atmospheric research*, 83(2-4):336–348, 2007.

[46] Paul M Markowski and Yvette P Richardson. Tornadogenesis: Our current understanding, forecasting considerations, and questions to guide future research. *Atmospheric Research*, 93(1-3): 3–10, 2009.

[47] Paul M Markowski, Jerry M Straka, and Erik N Rasmussen. Direct surface thermodynamic observations within the rear-flank downdrafts of nontornadic and tornadic supercells. *Monthly weather review*, 130(7):1692–1721, 2002.

[48] GM Martin, DW Johnson, and An Spice. The measurement and parameterization of effective radius of droplets in warm stratocumulus clouds. *Journal of the Atmospheric Sciences*, 51(13): 1823–1842, 1994.

[49] Met Office: Learn About Weather. Two types of waterspouts. `https://www.youtube.com/watch?v=TSLRSFpgIbI`, 2018. Accessed 2020.

[50] JA Milbrandt and MK Yau. A multimoment bulk microphysics parameterization. part i: Analysis of the role of the spectral shape parameter. *Journal of the atmospheric sciences*, 62(9):3051–3064, 2005.

[51] Robert C Miller. *Notes on analysis and severe-storm forecasting procedures of the Air Force Global Weather Central*, volume 200. AWS, 1975.

[52] David L Mitchell and Andrew J Heymsfield. Refinements in the treatment of ice particle terminal velocities, highlighting aggregates. *Journal of the atmospheric sciences*, 62(5):1637–1644, 2005.

[53] H Morrison and JO Pinto. Mesoscale modeling of springtime arctic mixed-phase stratiform clouds using a new two-moment bulk microphysics scheme. *Journal of the atmospheric sciences*, 62 (10):3683–3704, 2005.

[54] Hugh Morrison, Gregory Thompson, and V Tatarskii. Impact of cloud microphysics on the development of trailing stratiform precipitation in a simulated squall line: Comparison of one-and two-moment schemes. *Monthly weather review*, 137(3):991–1007, 2009.

[55] NWS NEXRAD. Waterspouts (c). `https://web.archive.org/web/20160113151652/http://www.desktopdoppler.com/help/nws-nexrad.htm#rainfall%20rates`, April 2009. Accessed 2020.

[56] HWT Owen. Waterspouts in the north sea. *Weather*, 1:215–216, 1946.

[57] Pennsylvania State University. Introductory meteorology. https://www.e-education.psu.edu/meteo3/node/2230, 2018. Accessed 2020.

[58] R. Behrendt H.Mahlke. Synoptic charts. www.wetter3.de, Since 2003. Accessed 2020.

[59] M Rajeevan, A Kesarkar, SB Thampi, TN Rao, B Radhakrishna, and M Rajasekhar. Sensitivity of wrf cloud microphysics to simulations of a severe thunderstorm event over southeast india. In *Annales Geophysicae*, volume 28, pages 603–619, 2010.

[60] VCPJ Ramanathan, PJ Crutzen, JT Kiehl, and Daniel Rosenfeld. Aerosols, climate, and the hydrological cycle. *science*, 294(5549):2119–2124, 2001.

[61] Erik N Rasmussen and David O Blanchard. A baseline climatology of sounding-derived supercell andtornado forecast parameters. *Weather and forecasting*, 13(4):1148–1164, 1998.

[62] Tanja Renko, Tomislav Kozarić, and Martina Tudor. Testing of waterspout forcasting indices over the adriatic sea using aladin model. In *6th European Conference on Severe Storms*, 2011.

[63] Tanja Renko, Josipa Kuzmic, and Natasa Strelec Mahovic. Synoptic and mesoscale analysis of waterspouts in the adriatic (2001–2011 preliminary climatology). In *Seventh European Conf. on Severe Storms*, 2013.

[64] Tanja Renko, Josipa Kuzmić, Vinko Šoljan, and Nataša Strelec Mahović. Waterspouts in the eastern adriatic from 2001 to 2013. *Natural hazards*, 82(1):441–470, 2016.

[65] Tanja Renko, Sarah Ivušić, Maja Telišman Prtenjak, Vinko Šoljan, and Igor Horvat. Waterspout forecasting method over the eastern adriatic using a high-resolution numerical weather model. In *Meteorology and Climatology of the Mediterranean and Black Seas*, pages 39–58. Springer, 2019.

[66] David J Reynolds. *Severe local storms in the United Kingdom: climatology and forecasting*. PhD thesis, University of Wales Swansea, 1999.

[67] Richard R. Waite. Waterspouts (a). https://commons.wikimedia.org/wiki/File:US_Navy_040905-N-1513W-085_An_HH-60H_Seahawk_keeps_an_eye_on_a_nearby_vessel_while_a_waterspout_takes_form_off_the_coast_of_Malaysia.jpg, September 5, 2004. Accessed 2020.

[68] Vernon John Rossow. *Observations of waterspouts and their parent clouds*. National Aeronautics and Space Administration, 1970.

[69] RTL Nederland. Radar images for case study 2. https://www.buienradar.nl, 2020. Accessed 2020.

[70] Sailing Journal. Waterspouts (b). https://www.giornaledellavela.com/2019/03/03/tromba-marina-sapete-come-evitarla/, March 3, 2019. Accessed 2020.

[71] Joanne Simpson. *Waterspouts, Gust Fronts and Associated Cloud Systems*, volume 85032. NASA, Goddard Space Flight Center, 1983.

[72] Michalis V Sioutas and Alexander G Keul. Waterspouts of the adriatic, ionian and aegean sea and their meteorological environment. *Atmospheric research*, 83(2-4):542–557, 2007.

[73] MV Sioutas and HA Flocas. Hailstorms in northern greece: synoptic patterns and thermodynamic environment. *Theoretical and Applied Climatology*, 75(3-4):189–202, 2003.

[74] SKYbrary. Accidents and incidents of waterspouts. https://www.skybrary.aero/index.php/Waterspout, 2019. Accessed 2020.

[75] Skystef. Tornado indicators. http://www.skystef.be/storm-indices.htm, 2004-2020. Accessed 2020.

[76] Scott M Spratt and BK Choy. Employing the wsr-88d for waterspout forecasting. In *Postprints, NEXRAD Users Conference*, pages 248–258. NWS Norman, OK, 1994.

[77] David J Stensrud, John V Cortinas Jr, and Harold E Brooks. Discriminating between tornadic and nontornadic thunderstorms using mesoscale model output. *Weather and forecasting*, 12(3): 613–632, 1997.

[78] W Szilagyi. A waterspout forecasting technique. In *5th European conference on severe storms*, pages 12–16, 2009.

[79] The Met Office. Surface synoptic charts. `https://metoffice.gov.uk`, 2020. Accessed 2020.

[80] The Meteo Company B.V. Satellite image. `https://en.sat24.com/en`, 2006-2020. Accessed 2020.

[81] The University of Wyoming. A publicly available repository of radiosonde data. `http://weather.uwyo.edu/upperair/sounding.html`, 2020. Accessed 2020.

[82] Gregory Thompson, Roy M Rasmussen, and Kevin Manning. Explicit forecasts of winter precipitation using an improved bulk microphysics scheme. part i: Description and sensitivity analysis. *Monthly Weather Review*, 132(2):519–542, 2004.

[83] Gregory Thompson, Paul R Field, Roy M Rasmussen, and William D Hall. Explicit forecasts of winter precipitation using an improved bulk microphysics scheme. part ii: Implementation of a new snow parameterization. *Monthly Weather Review*, 136(12):5095–5115, 2008.

[84] Richard L Thompson, Roger Edwards, John A Hart, Kimberly L Elmore, and Paul Markowski. Close proximity soundings within supercell environments obtained from the rapid update cycle. *Weather and Forecasting*, 18(6):1243–1261, 2003.

[85] Ali Tokay and David A Short. Evidence from tropical raindrop spectra of the origin of rain from stratiform versus convective clouds. *Journal of applied meteorology*, 35(3):355–371, 1996.

[86] Roger M Wakimoto and James W Wilson. Non-supercell tornadoes. *Monthly Weather Review*, 117(6):1113–1140, 1989.

[87] A Waldvogel. The n 0 jump of raindrop spectra. *Journal of the Atmospheric Sciences*, 31(4): 1067–1078, 1974.

[88] Leela Watson. Upgrade summer severe weather tool. 2011.

[89] A Wegener. Wind-und wasserhosen in europa (tornadoes in europe). *Verlag Friedrich Vieweg und Sohn, Braunschweig*, 1917.

[90] Mark M Wheeler. Severe weather and weak waterspout checklist in midds. 2009.

[91] Wikipedia. List of european tornadoes and tornado outbreaks. `https://en.wikipedia.org/wiki/List_of_European_tornadoes_and_tornado_outbreaks`, 2020. Accessed 2020.

[92] WindEurope. wind energy. `https://windeurope.org/about-wind/statistics/`, 2020. Accessed 2020.

A

Microphysics schemes

Microphysics processes play an essential role in simulating different situations related to water vapor, cloud and hydrometeors, and latent heat. Although we know the aerosol effects of microphysics schemes might change properties of any cloud type, the interaction between aerosols and convective clouds are uncertain. As a result, microphysical parameterizations could be a principal source of uncertainty in convection in NWP simulations.

Microphysics is the process by which moisture is removed from the air, based on other thermodynamic and kinematic fields represented within the numerical models (ElTahan and Magooda, 2017). It attempts to accurately account for sub-grid scale updrafts, clouds, and precipitation. Generally, there are two distinct directions for microphysical parameterization in atmospheric simulation, the bulk microphysics parameterization and spectral (bin) microphysics. Although these two methods simulate the same microphysical processes and provide similar outputs, spectral (bin) microphysics explicitly calculate the particle size distribution (PSD) and provide more accurate solutions than the bulk method. However, the bin method is too expensive for operational use. In order to improve the efficiency of computation, the bulk microphysics parameterization scheme calculates with a semi-empirical PSD for different hydrometeor types instead of themselves.

The bulk microphysics parameterization scheme can be divided into single-moment schemes, and two-moment schemes. There is a kth moment equation of particle size distributions Equation A.1 with k primarily an integer value. For a single-moment bulk scheme, it only predicts the hydrometeors' mixing ratios (k=1). Particle Size Distribution (PSD) can be used to represent these hydrometeors, Gamma function is most frequently used. As for double-moment, it predicts not only the mass densities of hydrometeors (k=1) but also the number of concentrations (k=0).

$$M^{(k)} = \int m^k f(m) dm \tag{A.1}$$

Kessler (1969) presented a bulk scheme only takes warm rain processes into account, no ice process are considered. Later on, Lin et al. (1983) simulated a moderate intensity thunderstorm, and the result shows an improving reality by including snowfield. After this, the bulk parameterization scheme development, which included warm and ice processes, became normal. Many bulk schemes are used in mesoscale models nowadays. There are various choices of the bulk scheme, but many double-moment schemes can not predict all number of concentration of hydrometeor species. For example, the number concentration of the Thompson scheme only include cloud ice and rain (Thompson et al., 2008). The cloud number concentration is diagnosed in Morrison 2–moment Scheme (Morrison et al., 2009). New schemes contain more types of hydrometeors and more moments used to describe the PSDs of the hydrometeors. Despite differences in a larger number of bulk parameterization schemes, most bulk schemes are based on the same system of equations for PSDs, which is a three parameters gamma distribution (Equation A.2).

$$f(m) = N_o m^{\nu} exp(-\lambda m^{\mu}) \tag{A.2}$$

where ν is the shape parameter, when $\nu = 0$, the equation reduces to an inverse-exponential distribution. Thus, N_o usually is the intercept, λ is the slope or scale parameter by single or multiple of the moments distribution function to accomplish the simulation of distribution variation. One prognostic parameter is connected with one predicted moment; hence three parameters in the gamma distribution (Equation A.2) need three predictive moment equations. However, research in decades use more one- or two-moment instead of three-moment parameterization. The hydrometeor size distribution is predicted in one moment scheme, and the other two parameters are prescribed or diagnosed. The mass content and the total number concentration are predicted by a two-moment scheme, λ and N_0 become independent prognostic variables, ν is constant.

In the mesoscale modelling field, a double-moment scheme shows more flexibility of the size distribution to allow the mean diameter evolving compared with the single-moment scheme, even though it consumes more time to run than the single-moment scheme. Several studies have shown the advantage of the double-moment method in simulating precipitating convective clouds (Thompson et al., 2004; Milbrandt and Yau, 2005). Prognostic equations of the raindrop number concentration allow large drops concentration in a reasonable range for a heavily precipitating situation. In 2009, Morrison et al. found the double-moment method intensifies the precipitation in the trailing stratiform location. However, convective activities around the convection core become weaker due to the difference in raindrop size distribution. A three-moment parameterization has been developed by diagnosing ν is a function of the predicted moments, because it is difficult to separate the particular impacts when ν is varying in a nonlinear simulation. This was described in detail by Milbrandt and Yau (2005).

Table A.1 show the detail of five microphysics parameterization schemes which were used in this research. Q denotes the mass variable, N represents the number variable, v, c, r, i, s, g, h are short for water vapor, cloud water, rainwater, cloud ice, snow, graupel, and hail respectively. The following parts will describe these five microphysics schemes individually.

Table A.1: Details of selected microphysics parameterization schemes in the WRF model

MP Options	Scheme Name	Mass Variables	Number Variables	Moment	Class
6	WSM6	$Q_v, Q_c, Q_r, Q_i, Q_s, Q_g$		1	6
8	New Thompson	$Q_v, Q_c, Q_r, Q_i, Q_s, Q_g$	N_i, N_r	2	6
9	Milbrandt-Yau	$Q_v, Q_c, Q_r, Q_i, Q_s, Q_g, Q_h$	$N_c, N_r, N_i, N_s, N_g, N_h$	2/3	7
10	Morrison 2-moment	$Q_v, Q_c, Q_r, Q_i, Q_s, Q_g$	N_c, N_r, N_i, N_s, N_g	2	6
16	WDM6	$Q_v, Q_c, Q_r, Q_i, Q_s, Q_g,$	N_c, N_r	2	6

A.1. WSM6 Scheme

Hong et al. assessed two classifications of the WRF-Single-Moment-Microphysics schemes (WSMMPs). The first is class 3, called WSM3, with prognostic water substance variables of water vapor, cloud water/ice, and rain/snow. The second is class 5, called WSM5, with water vapor, cloud, ice, rain, and snow in 2004 (Hong et al.,2004). A new scheme called WRF Single-Moment 6-class scheme (WSM6) was developed based on WSM5 and added a new predictive variable: graupel. It assumed the particle comprising graupel (Q_g) follow the size distribution as Equation A.3

$$n_g(D)dD_g[m^{-4}] = n_{0g} exp(-\lambda_G D_g)dD_g \tag{A.3}$$

where $n_g(D)dD_g[m^{-4}]$ is the number of graupel particles per cubic meter of air with diameters between D_g and $D_g + dD_g$; $n_{0g}(m^{-4})$ is the intercept value ($n_{0g} = 4 * 10^6 m^{-4}$ here) and $\lambda_g(m^{-1})$ is the slope of distribution (Hong and Lim, 2006).

The WSMMPs compute the sedimentation of falling hydrometeors at first, then turn to the microphysical processes. This is different from some other schemes. The freezing or melting processes are computed during falling sub-steps result in an increasingly accurate vertical heating profile.

Overall, a more elaborate scheme WSM6 was developed, and there are two unique features, the first is that it assumes the ice nuclei number concentration as a function of temperature in order to show the ice processes. The second is a new assumption, which is the ice crystal number concentrations as a function of the ice. Additionally, the WSMMPs show a resolution dependency. A higher resolution grid increases the effect on each grid (Hong and Lim, 2006).

A.2. New Thompson Scheme

New Thompson is a new snow parameterization for the WRF model and other mesoscale models. In its setting, snow size distribution, as a sum of exponential and gamma distribution, is a result of ice water content and temperature. Thompson et al. (2004) developed an additional prognostic variable for the number concentration of cloud ice. The following research added a prognostic variable, the number of concentrations for rain species, so this scheme is more like a quasi-double moment, called the New Thompson scheme. Thus, the New Thompson scheme includes water vapor and cloud drops, rain, ice, snow, graupel these five hydro physics, and it is a two-moment scheme for ice and raindrops.

The assumption of spherical snow is the constant bulk density for most bulk microphysical parameterization. In fact, according to several decades of observation, the density varies inversely with size. New Thompson scheme uses early research to deviate from spherical snow relation:

$$m(D) = 0.069D^2 \tag{A.4}$$

where D is particle diameter.

Another difference with other microphysics is the snow size distribution. The New Thompson scheme adopted the following function:

$$N(D) = \frac{\mu_2^4}{\mu_3^3}[\kappa_0 e^{-\frac{\mu_2}{\mu_3}\Lambda_0 D} + \kappa_1(\frac{\mu_2}{\mu_3}D)^{\mu_s} e^{-\frac{\mu_2}{\mu_3}\Lambda_1 D}] \tag{A.5}$$

$$\mu_n = \int D^n N(D) dD \tag{A.6}$$

where μ_n is the nth moment of the snow size distribution,snow size distribution constant κ_0=490.6, κ_1=17.46, Λ_0=20.78,Λ_1=3.29. In the bracket of Equation A.5, the first term presents an exponential distribution and the second term represents a gamma distribution (Thompson et al., 2008).

Moreover, in the new Thompson scheme, snow forms by vapor depositional growth onto cloud ice particles until those ice crystals grow beyond a threshold size. Currently, the value is 200 μm (Thompson et al., 2008). The threshold is not precise but allow exiting both slow tiny ice crystals and rapidly falling snow.

One more feature of the new Thompson scheme is that it utilizes a variable efficiency based on the median volume diameter of snow and cloud water instead of a constant collection efficiency commonly used by other scheme (Thompson et al., 2008).

Last but not the least, the snow terminal velocity constants were set, which match vertically pointing Doppler radar data and observations (Mitchell and Heymsfield, 2005).

A.3. Milbrandt-Yau Scheme

Most of the existing microphysics schemes use a three-parameter gamma distribution (Equation A.10) to describe the size spectrum of each hydrometeor category. With computer power improving, the spectral shape parameter μ can be varied rather than a constant. A multi moment bulk microphysics scheme Milbrandt-Yau scheme has been developed.

$$N(D) = N_0 D^{\mu} e^{-\lambda D} \tag{A.7}$$

Milbrandt-Yau scheme is a triple-moment scheme for hail. The radar reflectivity as a tendency (Equation A.8) for three moment, the shape parameter ν in Equation A.2 was set as a prognostic variable and predicted based on an additional prognostic equation (Milbrandt and Yau, 2005).

$$\frac{\partial Z_x}{\partial t} = -\nabla \cdot (Z_x U) + TURB(Z_x) + \frac{\partial Z_x V_{Zx}}{\partial t} + \frac{\partial Z_x}{\partial t}|_s \tag{A.8}$$

The terms on the right provide advection/divergence, turbulent mixing, sedimentation, and microphysical sources respectively. Z_x can be separated into three classes, the first one assumed the ν changes could neglect due to a specific process A. The second class is about processes in which hydrometeors are being initiated in a category, such as during nucleation. At the first step, $Z_x = Q_x = N_x = 0$. The third class is that category x is converted into another category y, here:

$$\frac{\partial Z_x}{\partial t}|_A = -(\frac{c_y}{c_x}^2)\frac{\partial Z_y}{\partial t}|_A \tag{A.9}$$

One of the significant features of Milbrandt-Yau is using the relation between the number of active cloud condensation nuclei (CCN) and supersaturation (Cohard et al., 1998) instead of the number concentration of cloud droplet. A variate cloud droplet number concentration provides a more realistic simulation results. Besides, graupel was added into variables to make this scheme a 7-class scheme. Considering the difference in density and terminal fall velocity in different hydrometeors, this new variable makes the scheme more realistic.

A.4. Morrison 2-moment Scheme

A two-moment microphysics scheme called Morrison double-moment scheme is used to examine trailing stratiform precipitation in an idealized situation of the 2D squall line.

This scheme stood on Morrison and Pinto (2005) parameterization, and added mixing ratio and number concentration of graupel. Equation A.10 was used by Morrison2-moment scheme to represent particle size distribution of cloud and precipitation.

$$N(D) = N_0 D^{\mu} e^{-\lambda D} \tag{A.10}$$

where N_0, λ, μ, and D represent the intercept, slope, shape parameters of the size distribution and the particle diameter, respectively. Here, all particles are assumed to be spheres. The shape parameters of size distribution μ=0, for the precipitation species, so the size distributions are exponential functions. For cloud droplets, μ is a function of the predicted droplet number concentration according to observations from Martin et al., 1994.

In the Morrison 2-moment scheme, the setting assumes that the mean size has no change. That is to say, the decreasing number of concentration decreases equal to mixing ratio during rain evaporation and snow or graupel sublimation. The number concentration of graupel and snow decreases by the equal rain number concentration increase due to melting.

Compared with single-moment simulation, Morrison double-moment shows a decrease of rain evaporation rate, and a more significant mean raindrop size causes larger radar reflectivity in the stratiform area. Also, an increase of rain evaporation rate in the convective area, which induced a decline in the convective updrafts, and the intensity of mesoscale updraft increases, shows an association with the faster ice growth rate.

A.5. WDM6 Scheme

The WRF Double-Moment 6-class scheme (WDM6) microphysics scheme is based on the WRF single-moment 6-class (WSM6) scheme and includes the number concentration of rain and cloud. The Cloud Condensation Nuclei (CCN) number concentration is predicted depending on the relationship between the number of activated CCN and environmental supersaturation. Additionally, in the WSM6 scheme, the ice phase processes are included, warm rain microphysics are added into the WDM6 scheme. According to Ramanathan et al. in 2001, aerosols can increase solar radiation scattered and absorbed, and generate bright clouds which affects radiation and precipitation. In a following research by Khan et al. in 2008 shows aerosols have effects on microphysics and rainfall of warm cloud-based cloud aspects. Thus, the WDM6 scheme adds a prognostic treatment of CCN particles to activate cloud waters. In contrast to other double-moment bulk microphysics schemes, WDM6 includes prognostic equation for cloud water and CCN number concentration. This means that aerosol impacts on cloud and precipitation are considered.

All microphysical processes use the cloud–raindrop size distribution that are computed by Equation A.11

$$n_X(D_X) = N_X \frac{\alpha_X}{\Gamma(\nu_X)} \lambda_X^{\alpha_X \nu_X} D_X^{\alpha_X \nu_X - 1} exp[-(\lambda_X D_X)^{\alpha_X}] \tag{A.11}$$

where the index X∈[C, R],C and R represent clouds and rain respectively. λ_X is the corresponding slope parameter, α_X and ν_X are the two dispersion parameters, according to the Cohard and Pinty (2000) report,α_R=1 and ν_R=2, and α_C=3 and ν_C=1. Number concentration X is N_X, diameter of the drop category X is D_X (Lim and Hong, 2010).

For the WDM6 scheme, CCN number concentration n_a activation is a unique feature. Combined with Twomey's relationship between n_a and supersaturation S_W, the formula of the number of activated CCN is

$$n_a = (n + N_c)(\frac{S_w}{S_{max}})^k \tag{A.12}$$

where k is the parameter following the observation with a typical range from 0.3 to 1.0 (Khairoutdinov and Kogan, 2000), k=0.6 here. S_{max} is the supersaturation needed to activate the total particle count n+N_C. The preliminary results in current research indicated that the simulation is not sensitive when S_{max} is in a range of 0.22% to 0.8%.

A number of studies have reported that convective core includes a relatively large drop concentration value because of collision and coalescence. By contrast, a small value of drop concentration shown in the stratiform areas, because the double-moment scheme can reproduce ice particles under the melting process which increase precipitation (Waldvogel, 1974; Tokay and Short, 1996), while single-moment schemes always predict a stratiform-like behavior, it is an unclear area at the boundary between the convective and stratiform. Moreover, compared with the radar reflectivity of double-moment schemes, single-moment schemes' are weak with smaller rain number concentrations. Lim and Hong (2010) demonstrated that the WDM6 scheme enhanced radar reflectivity and weakened light rainfall while strengthening heavy rainfall activities compared with the WSM6 scheme.

B

Results at other four reported time - Case I

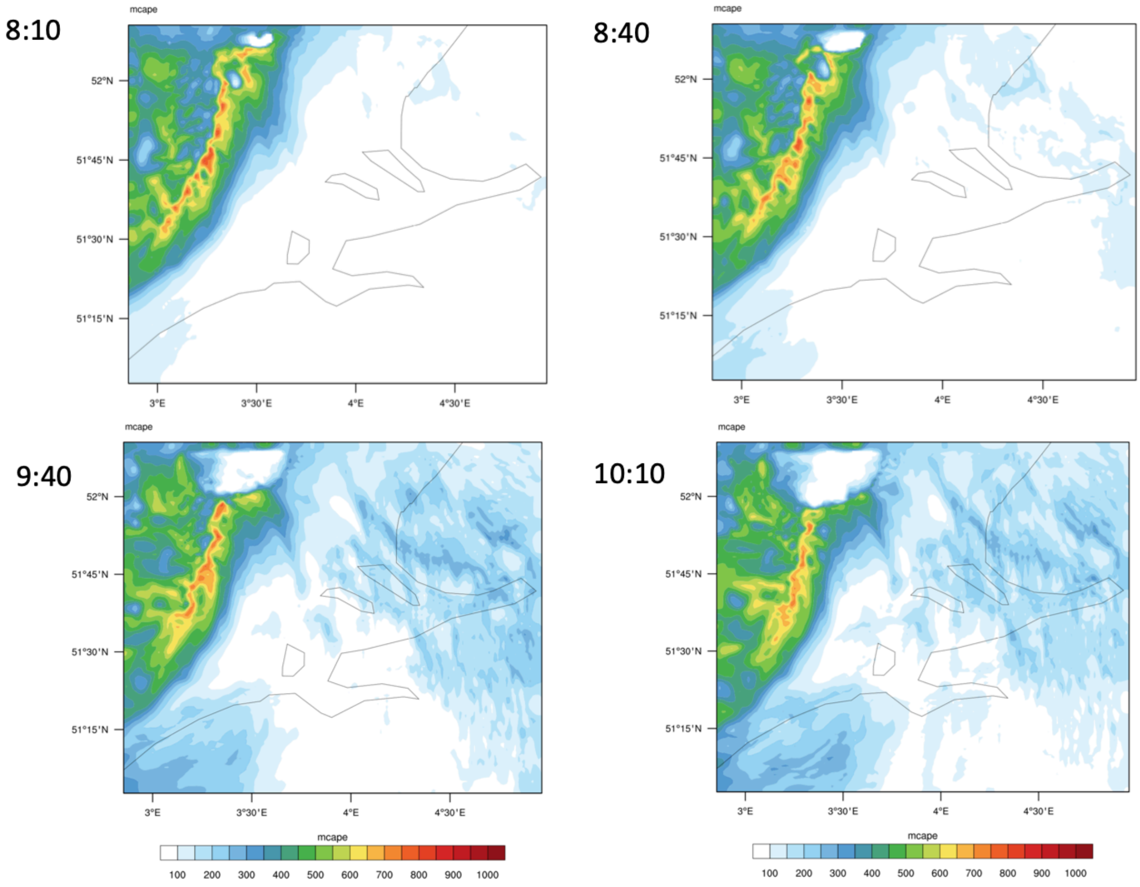

Figure B.1: Maximum convective available potential energy (MCAPE) by WSM6 scheme

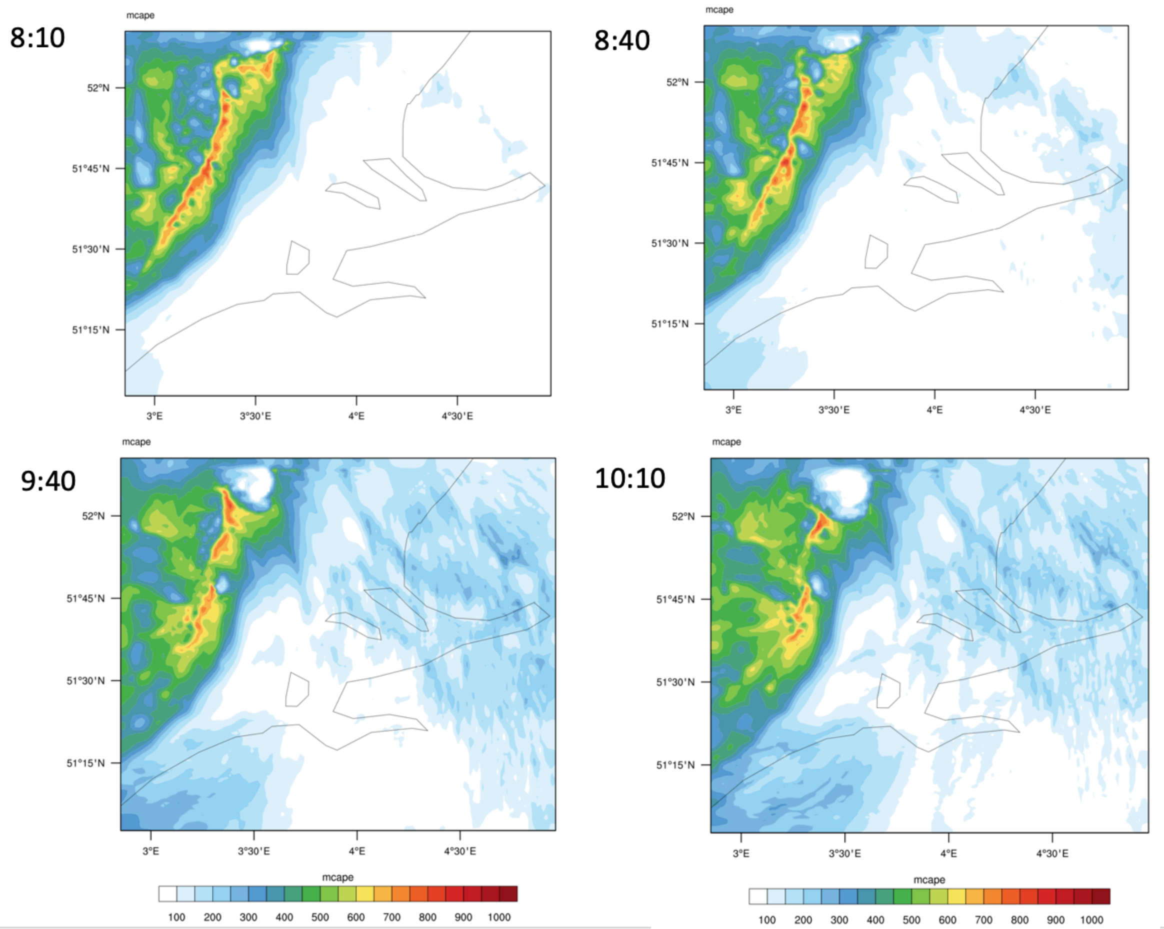

Figure B.2: Maximum convective available potential energy (MCAPE) by New Thompson scheme

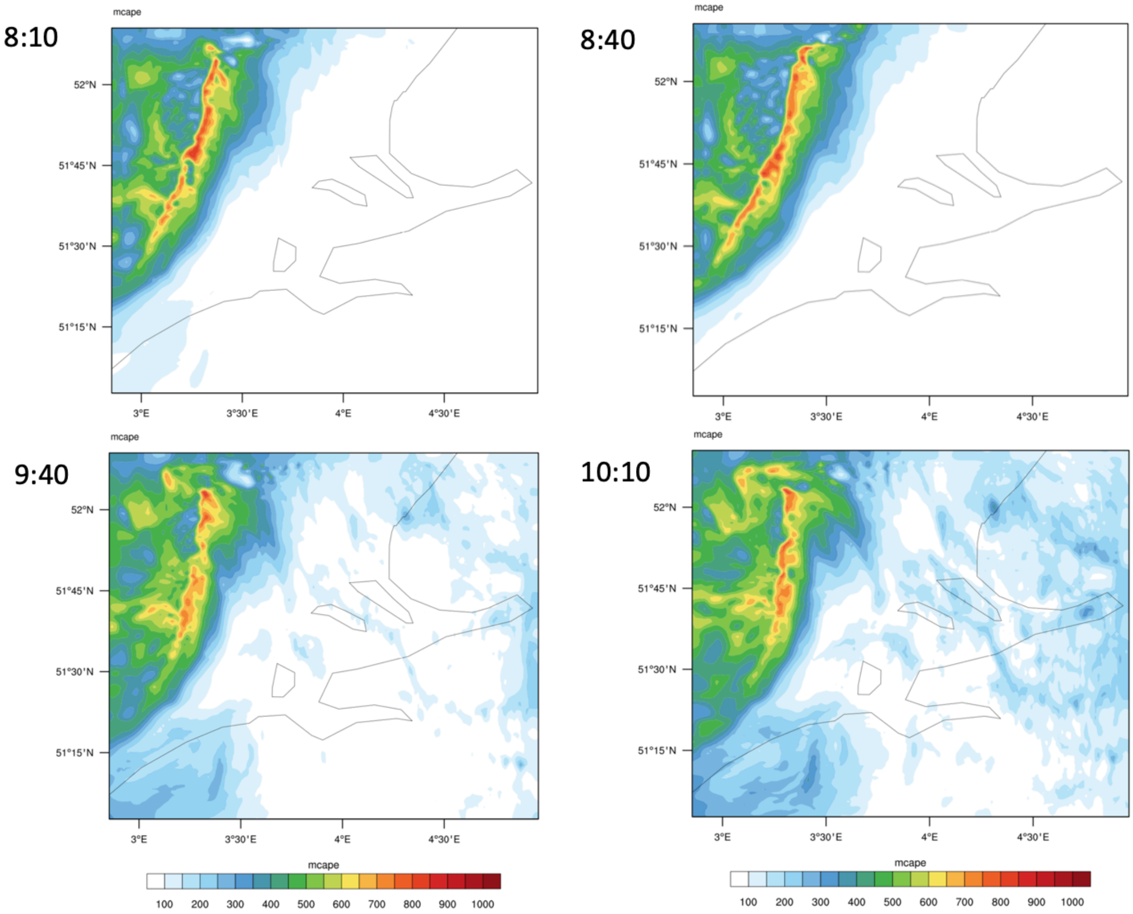

Figure B.3: Maximum convective available potential energy (MCAPE) by Milbrandt-Yau scheme

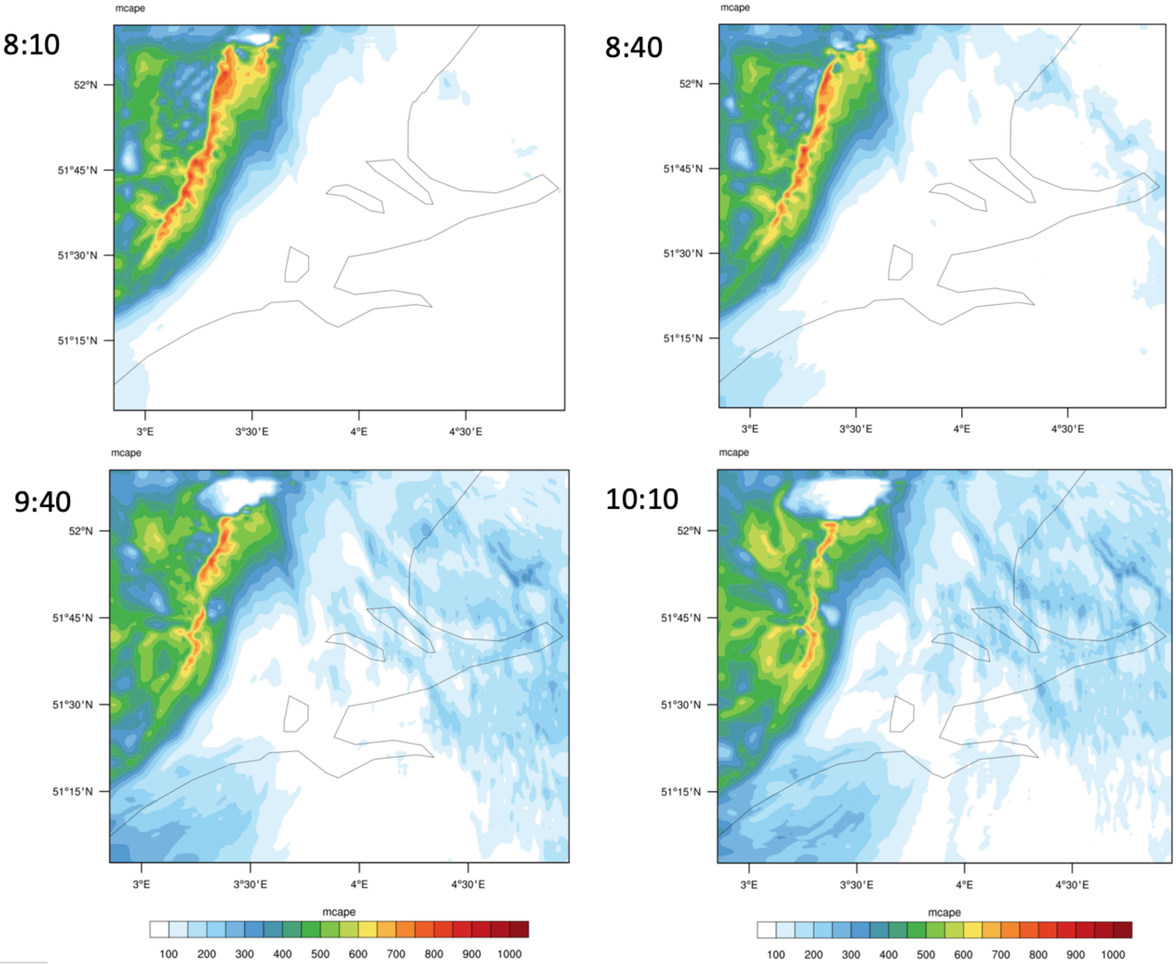

Figure B.4: Maximum convective available potential energy (MCAPE) by Morrison scheme

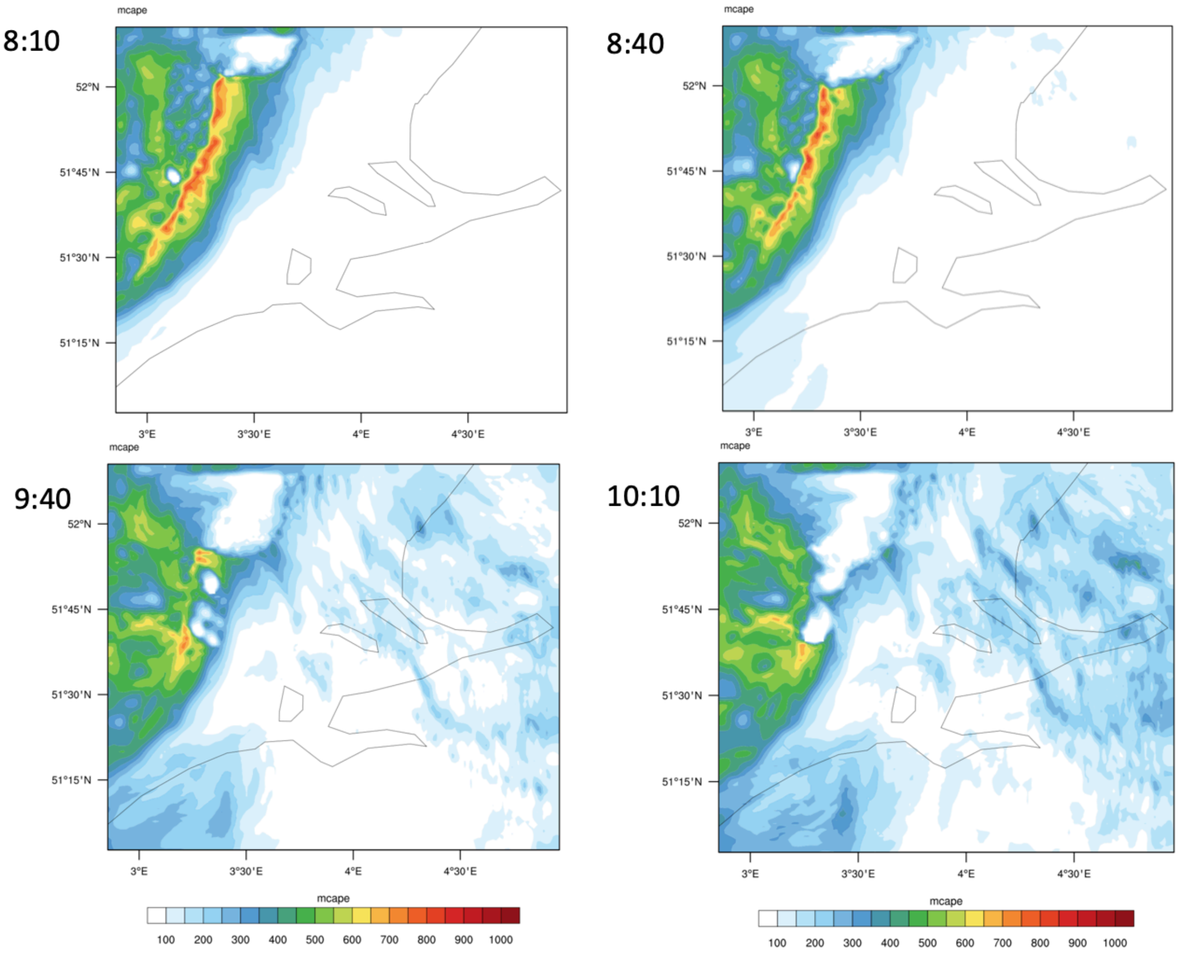

Figure B.5: Maximum convective available potential energy (MCAPE) by WDM6 scheme

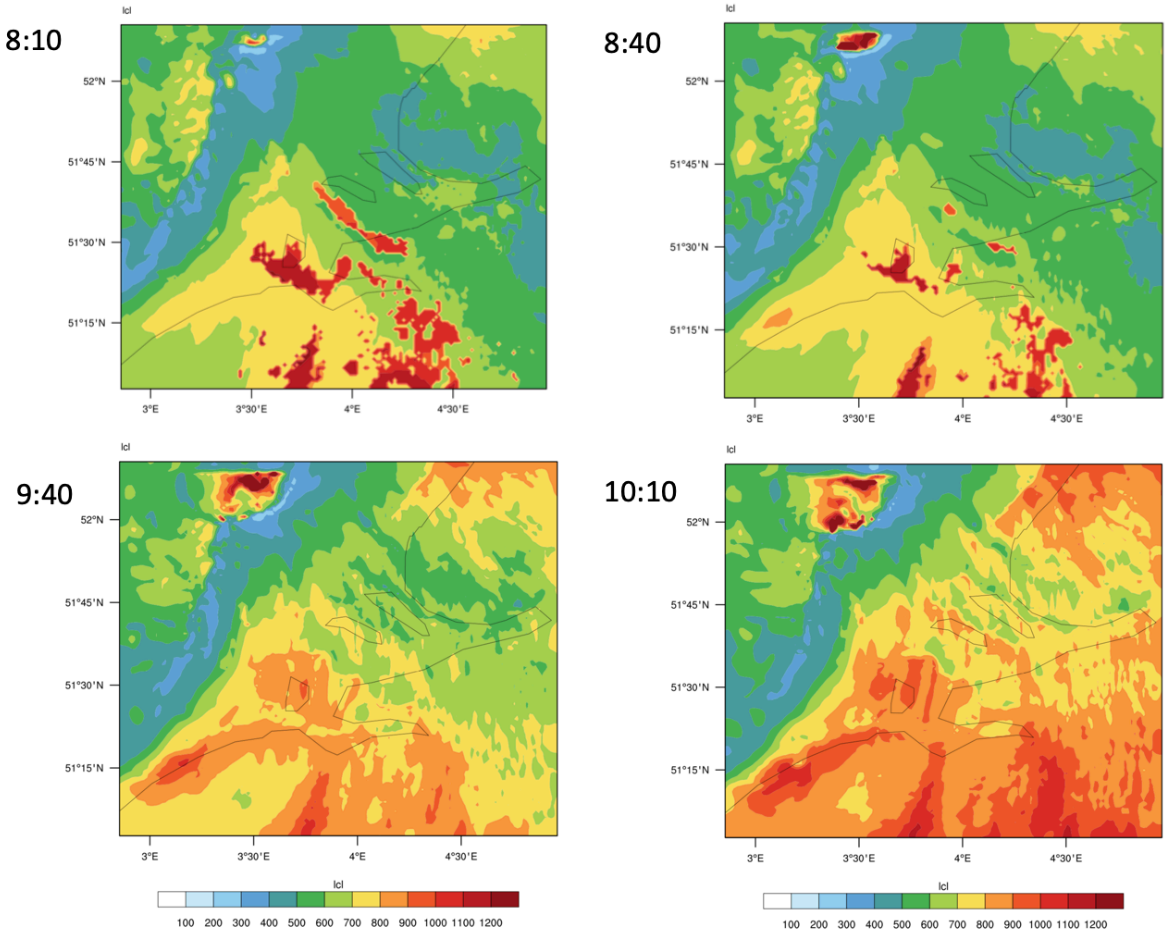

Figure B.6: Lifting Condensation Level (LCL) by WSM6 scheme

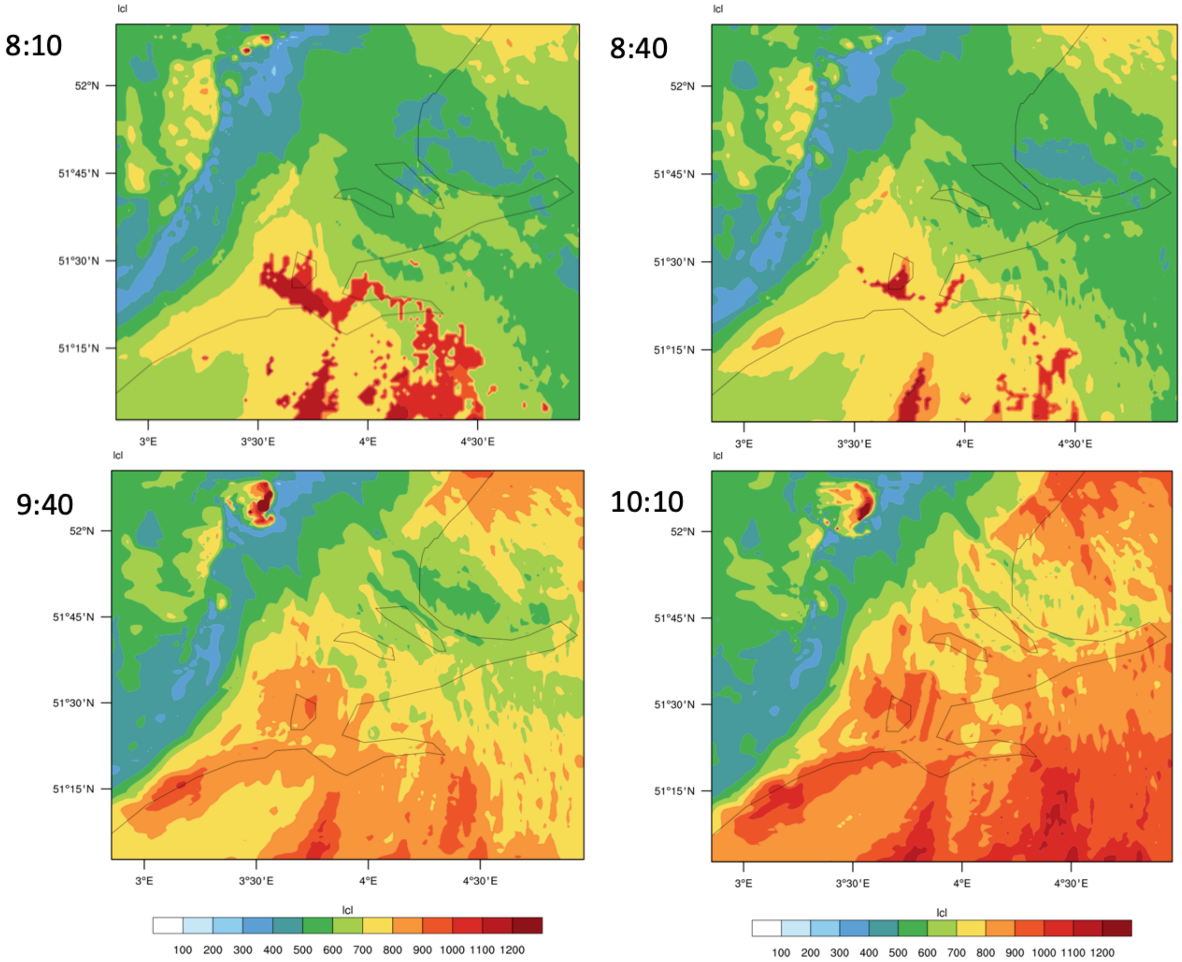

Figure B.7: Lifting Condensation Level (LCL) by New Thompson scheme

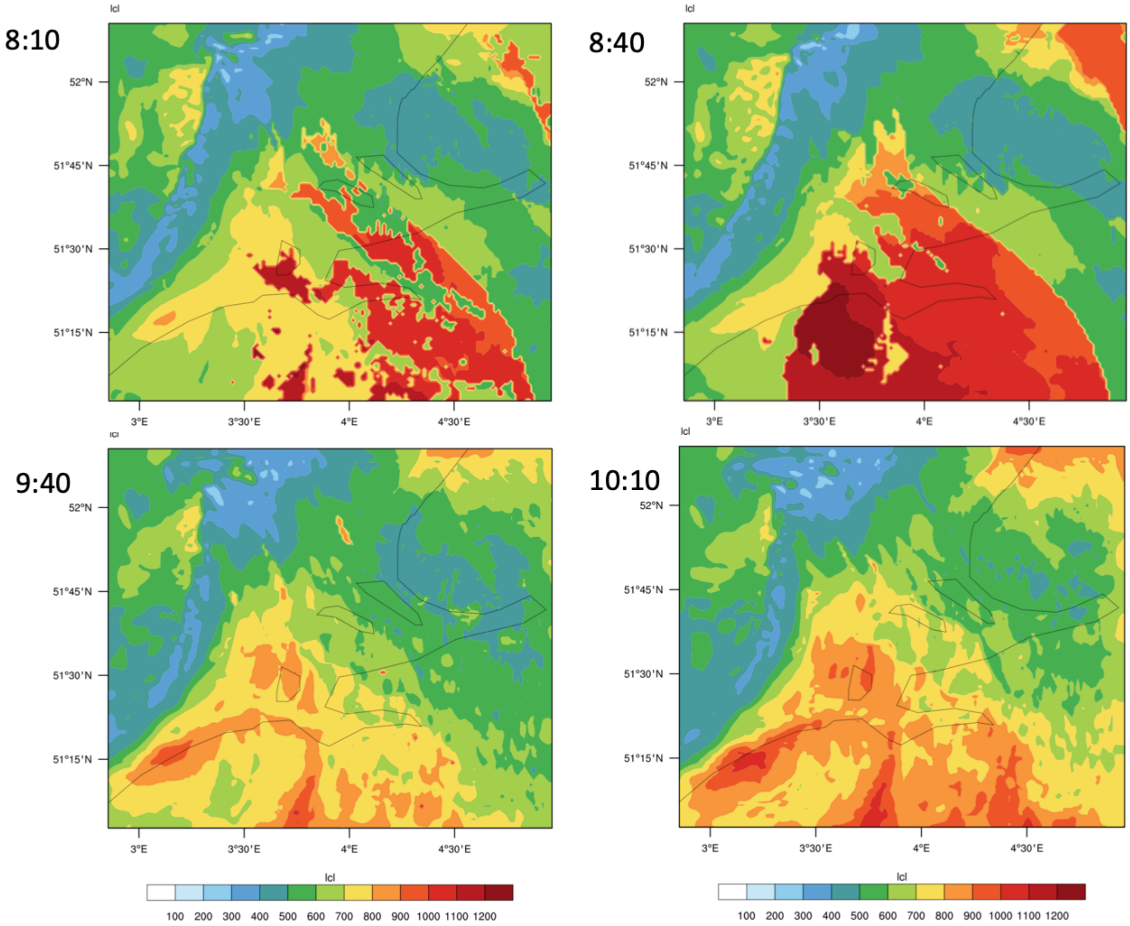

Figure B.8: Lifting Condensation Level (LCL) by Milbrandt-Yau scheme

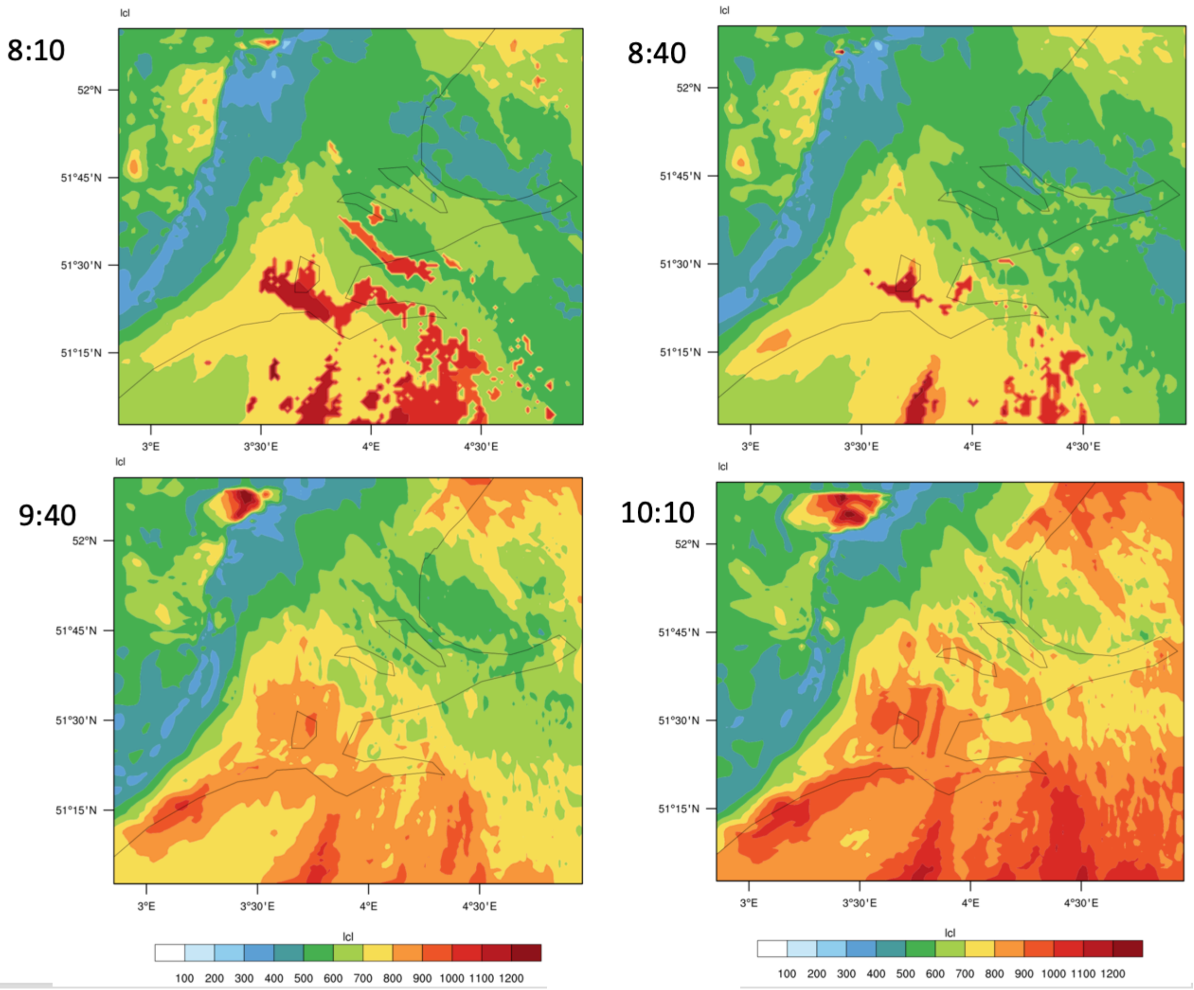

Figure B.9: Lifting Condensation Level (LCL) by Morrison scheme

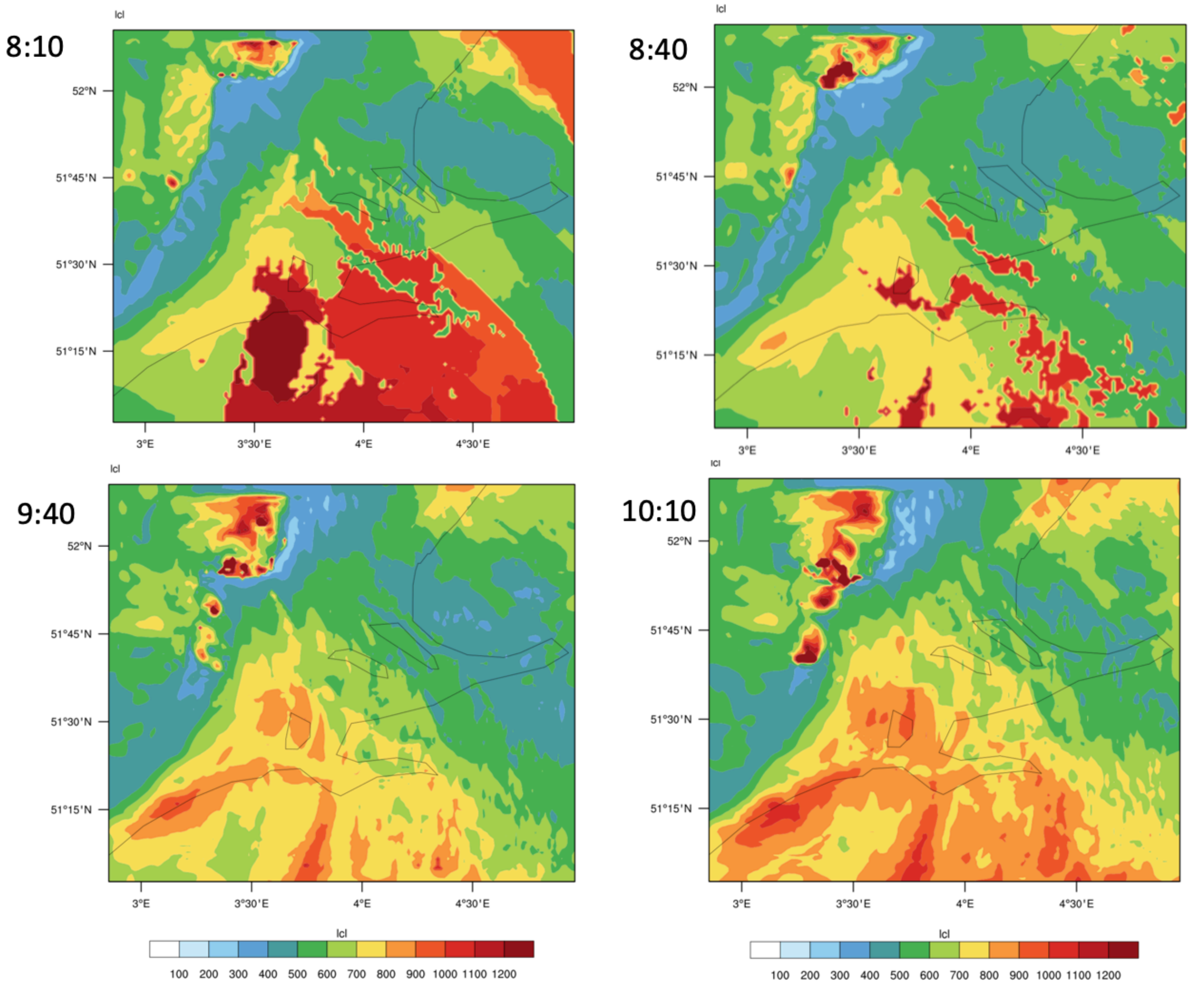

Figure B.10: Lifting Condensation Level (LCL) by WDM6 scheme

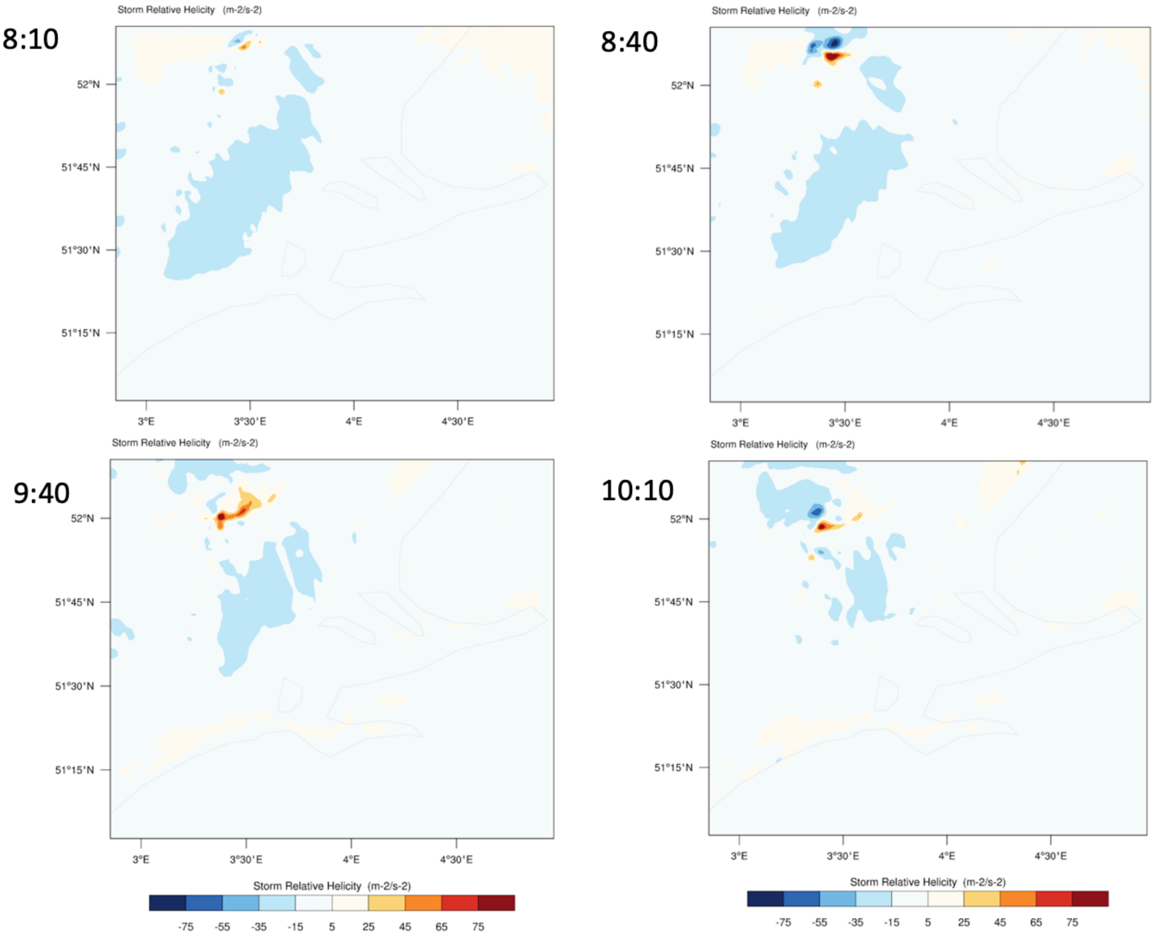

Figure B.11: 0–1 km Storm Relative Helicity (SRH) by WSM6 scheme

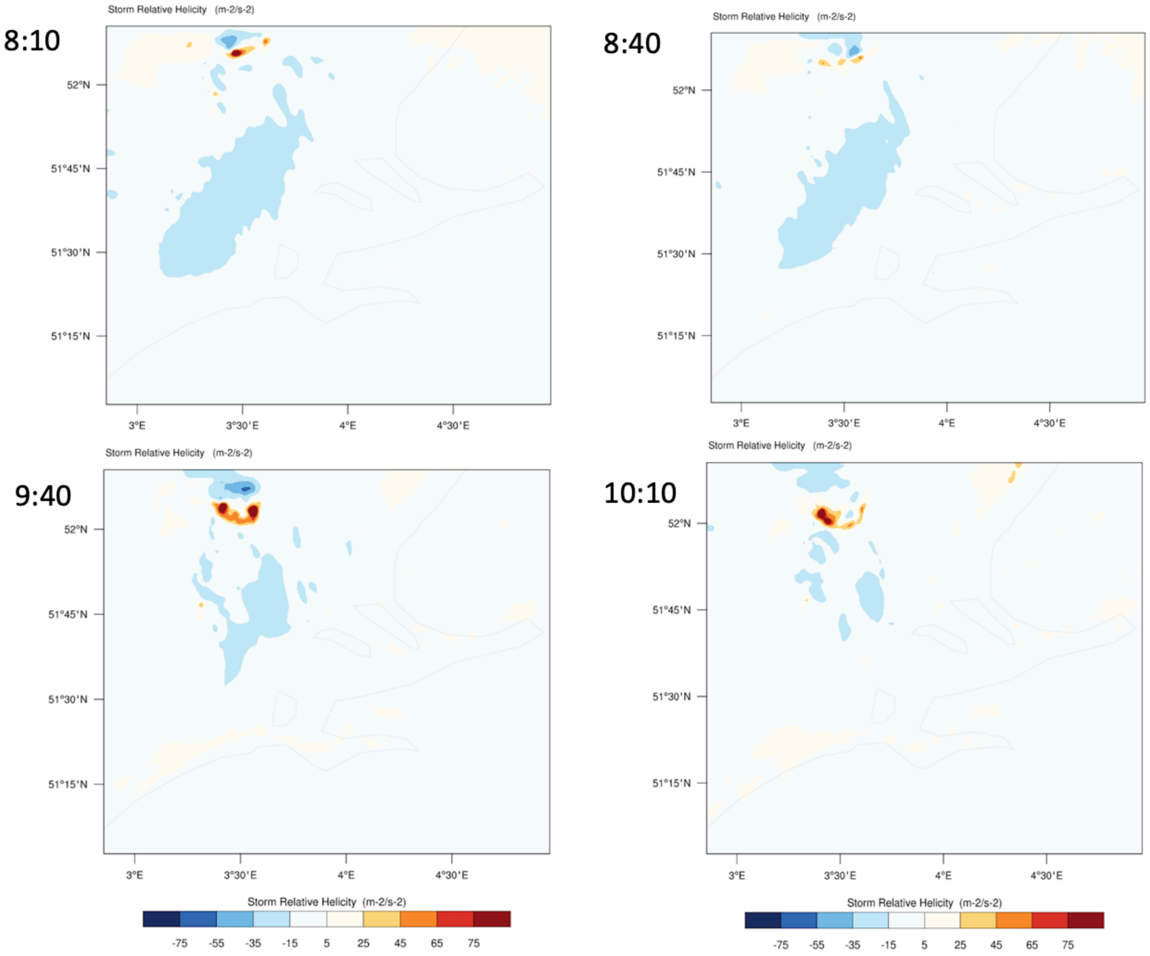

Figure B.12: 0–1 km Storm Relative Helicity (SRH) by New Thompson scheme

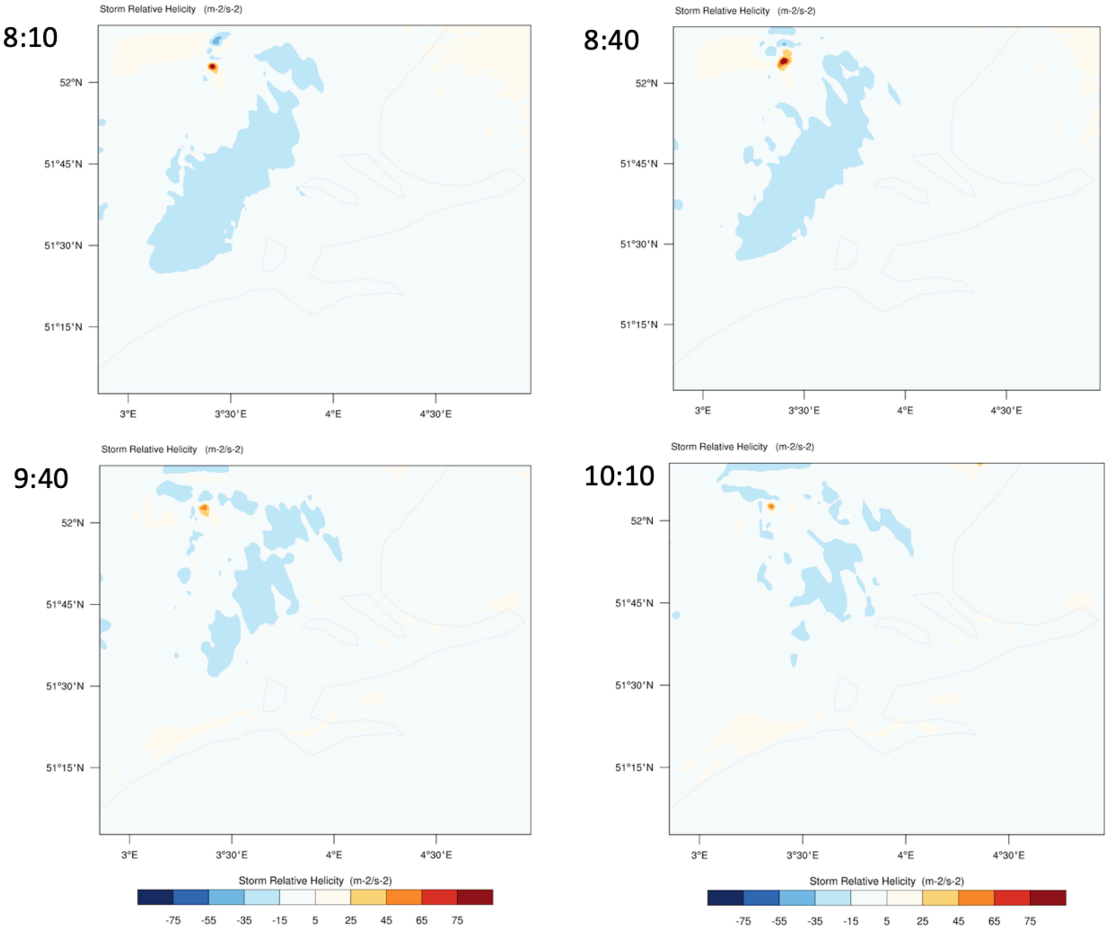

Figure B.13: L0–1 km Storm Relative Helicity (SRH) by Milbrandt-Yau scheme

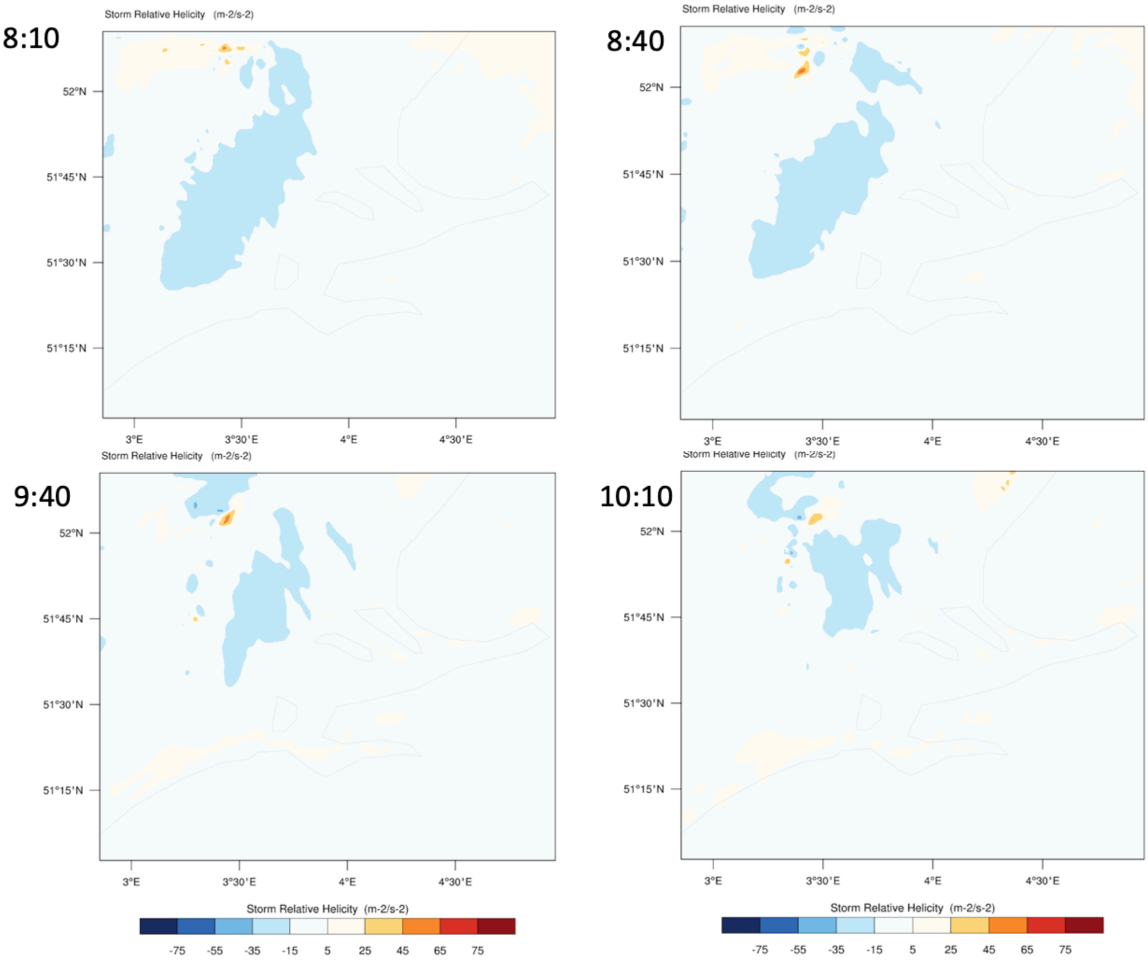

Figure B.14: 0–1 km Storm Relative Helicity (SRH) by Morrison scheme

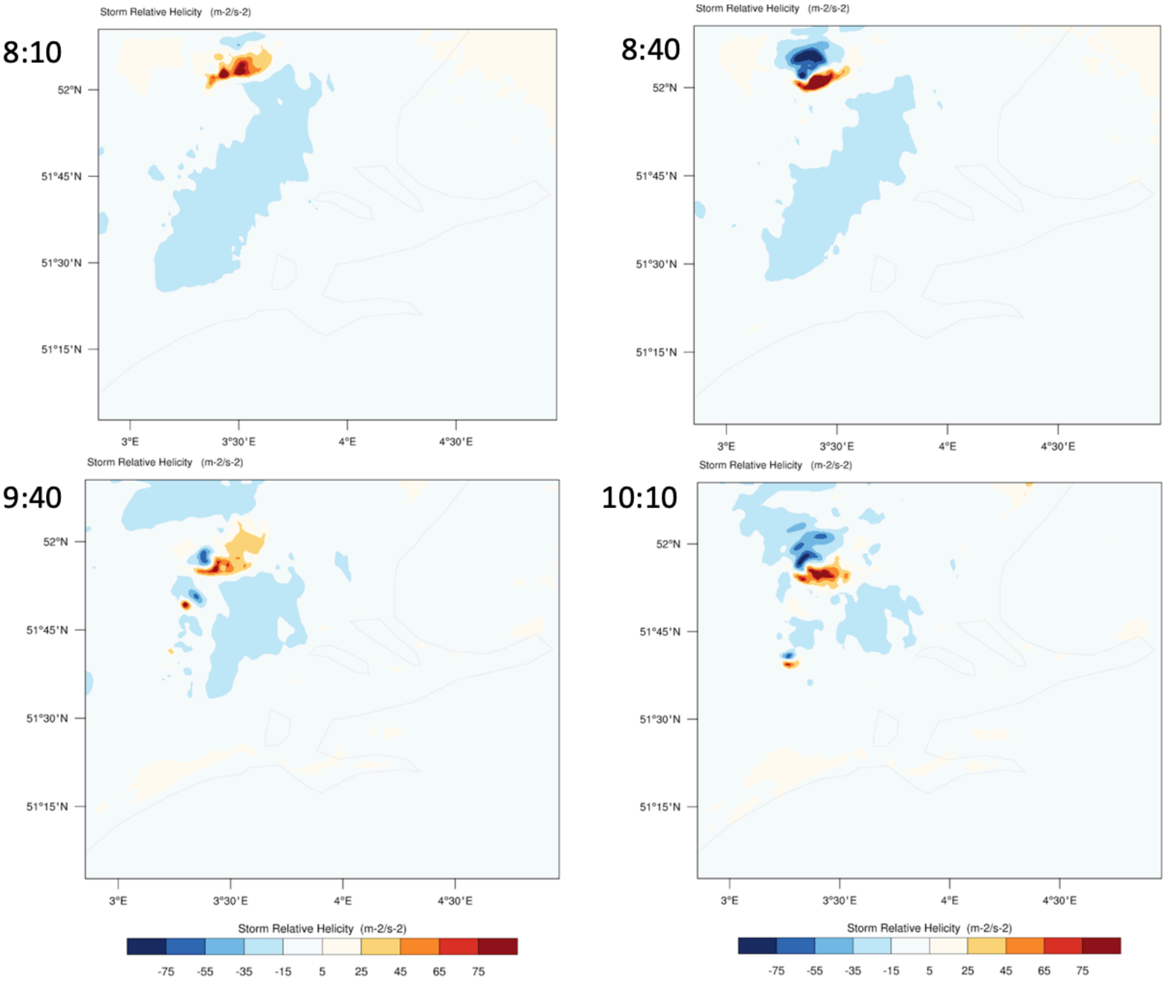

Figure B.15: 0–1 km Storm Relative Helicity (SRH) by WDM6 scheme

ACKNOWLEDGEMENTS

In this chapter, I would like to give my sincere appreciate to a number of individuals who helped me during my thesis project:

First of all, I would like to thank my chair supervisor Dr. Sukanta Basu, for offering me this opportunity to work on my field of interest, for the invaluable expertise, and for the patience and enthusiasm in discussing with me and guiding me through all stages of this project. He always shows his patience for my questions and gives me useful suggestions. Whenever I am stuck at technical or reporting obstacles, he was the one willing to help me out. Without his instructions and support, this thesis work could not be achieved in its present form. I would also like to thank my committee, Dr. Stephan de Roode for reviewing my work and providing insightful feedback; Prof.dr.S.J. Watson for the time to evaluate my work and give several valuable suggestions. We had several group meetings. They took the time to listen carefully to my research presentations and gave me thought-provoking comments within their fields of expertise.

Special thanks go to Sukanta's workstation and Vrlab for the powerful computational support. My laptop can not afford this type of expensive simulations, and it cost much to run them on a cloud virtual machine. I also want to thank Mr. Erwin de Beus for quick response to the question and technical instruction in terms of Vrlab.

Finally, thanks to my parents, mates from the same tutor and roommates, for their never-ending support and boundless affection.